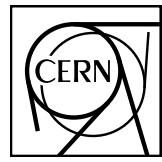


# EUROPEAN ORGANIZATION FOR NUCLEAR RESEARCH



ALICE-ANA-2016-xxx  
August 7, 2018

## Lambda-Kaon and Cascade-Kaon Femtoscopy in Pb-Pb Collisions at $\sqrt{s_{NN}} = 2.76$ TeV from the LHC ALICE Experiment

Jesse T. Buxton<sup>1</sup>

1. Department of Physics, The Ohio State University, Columbus, Ohio, USA

Email: jesse.thomas.buxton@cern.ch

### Abstract

We present results from a femtoscopic analysis of Lambda-Kaon correlations in Pb-Pb collisions at  $\sqrt{s_{NN}} = 2.76$  TeV by the ALICE experiment at the LHC. All pair combinations of  $\Lambda$  and  $\bar{\Lambda}$  with  $K^+$ ,  $K^-$  and  $K_S^0$  are analyzed. The femtoscopic correlations are the result of strong final-state interactions, and are fit with a parametrization based on a model by R. Lednicky and V. L. Lyuboshitz [1]. This allows us to both characterize the emission source and measure the scattering parameters for the particle pairs. We observe a large difference in the  $\Lambda K^+$  ( $\bar{\Lambda} K^-$ ) and  $\Lambda K^-$  ( $\bar{\Lambda} K^+$ ) correlations in pairs with low relative momenta ( $k^* \lesssim 100$  MeV). Additionally, the average of the  $\Lambda K^+$  ( $\bar{\Lambda} K^-$ ) and  $\Lambda K^-$  ( $\bar{\Lambda} K^+$ ) correlation functions is consistent with our  $\Lambda K_S^0$  ( $\bar{\Lambda} K_S^0$ ) measurement. The results suggest an effect arising from different quark-antiquark interactions in the pairs, i.e.  $s\bar{s}$  in  $\Lambda K^+$  ( $\bar{\Lambda} K^-$ ) and  $u\bar{u}$  in  $\Lambda K^-$  ( $\bar{\Lambda} K^+$ ). To gain further insight into this hypothesis, we currently are conducting a  $\Xi$ -K femtoscopic analysis.



## Contents

<b>1</b>	<b>Introduction</b>	<b>6</b>
<b>2</b>	<b>Data Sample and Software</b>	<b>6</b>
2.1	Data Sample . . . . .	6
2.2	Software . . . . .	6
<b>3</b>	<b>Data Selection</b>	<b>6</b>
3.1	Event Selection and Mixing . . . . .	6
3.2	$K^\pm$ Track Selection . . . . .	7
3.3	V0 Selection . . . . .	8
3.3.1	$\Lambda$ Reconstruction . . . . .	9
3.3.2	$K_S^0$ Reconstruction . . . . .	11
3.3.3	V0 Purity Background Estimation . . . . .	13
3.4	Cascade Reconstruction . . . . .	14
3.5	Pair Selection . . . . .	16
<b>4</b>	<b>Correlation Functions</b>	<b>20</b>
4.1	Typical Correlation Function Construction . . . . .	20
4.2	Stavinsky Correlation Function Construction . . . . .	22
<b>5</b>	<b>Fitting</b>	<b>25</b>
5.1	Model: $\Lambda K_S^0$ , $\Lambda K^\pm$ , $\Xi^{ch} K_S^0$ . . . . .	25
5.2	Model: $\Xi^{ch} K^{ch}$ . . . . .	25
5.3	Momentum Resolution Corrections . . . . .	26
5.4	Residual Correlations . . . . .	31
5.5	Non-Flat Background . . . . .	38
5.6	LednickyFitter . . . . .	41
5.7	Coulomb Fitter . . . . .	43
<b>6</b>	<b>Systematic Errors</b>	<b>44</b>
6.1	Systematic Errors: $\Lambda K_S^0$ . . . . .	44
6.1.1	Particle and Pair Cuts . . . . .	44
6.1.2	Non-Flat Background . . . . .	44
6.1.3	Fit Range . . . . .	45

6.2	Systematic Errors: $\Lambda K^\pm$	45
6.2.1	Particle and Pair Cuts	45
6.2.2	Non-Flat Background	45
6.2.3	Fit Range	45
6.3	Systematic Errors: $\Xi K^\pm$	46
6.3.1	Particle and Pair Cuts	46
<b>7</b>	<b>Results and Discussion</b>	<b>46</b>
7.1	Results: $\Lambda K_S^0$ and $\Lambda K^\pm$	46
7.1.1	Results: $\Lambda K_S^0$ and $\Lambda K^\pm$ : No Residual Correlations Included in Fit	48
7.1.2	Results: $\Lambda K_S^0$ and $\Lambda K^\pm$ : 3 Residual Correlations Included in Fit	54
7.1.3	Results: $\Lambda K_S^0$ and $\Lambda K^\pm$ : 10 Residual Correlations Included in Fit	62
7.1.4	Results: $\Lambda K_S^0$ and $\Lambda K^\pm$ : Fit Method Comparisons	70
7.2	Results: $\Xi K^\pm$	75
<b>8</b>	<b>To Do</b>	<b>76</b>
<b>9</b>	<b>Additional Figures</b>	<b>81</b>
9.1	Residuals	81
9.1.1	$\Lambda K^+$ Residuals	81
9.1.2	$\Lambda K^-$ Residuals	87
9.1.3	$\Lambda K_S^0$ Residuals	93

## List of Figures

1	V0 Reconstruction	9
2	$K_S^0$ contamination in $\Lambda(\bar{\Lambda})$ collection	10
3	$\Lambda$ and $\bar{\Lambda}$ Purity	11
4	$\Lambda(\bar{\Lambda})$ contamination in $K_S^0$ collection	12
5	$K_S^0$ Purity	13
6	V0 Purity Background Estimation	14
7	$\Xi$ Reconstruction	16
8	$\Xi^-(\bar{\Xi}^+)$ Purity	16
9	Average Separation of $\Lambda(\bar{\Lambda})$ and $K_S^0$ Daughters	18
10	Average Separation of $\Lambda(\bar{\Lambda})$ Daughter and $K^\pm$	18
11	Average Separation of $\Xi$ Daughters and $K^\pm$	19
12	$\Lambda K$ Correlation Functions	21
13	Correlation Functions: $\Lambda K^+$ vs $\Lambda K^-$ for 0-10% Centrality	21
14	$\Lambda K$ Stavinsky Correlation Functions (Correct)	23
15	$\Lambda K$ Stavinsky Correlation Functions (Correct and Incorrect)	24
16	Momentum Resolution: Sample $k_{True}^*$ vs. $k_{Rec}^*$	27
17	Particle Contaminations Visible in $k_{True}^*$ vs. $k_{Rec}^*$	28
18	Momentum Resolution Corrections: Methods Comparison	30
19	Residual Contributions Cartoon	31
20	Transform Matrices for $\Lambda K^+$ Analysis	32
21	Transform Matrices for $\bar{\Lambda} K^+$ Analysis	33
22	$\Sigma^0 K^+$ Transform	36
23	$\Sigma^0 K^+$ Transform	37
24	Compare Backgrounds	38
25	Backgrounds with THERMINATOR, $K_S^0$ Tweak	39
26	Backgrounds with THERMINATOR	40
27	Correlation with background decomposition (THERM)	41
28	Background reduction methods with THERMINATOR	42
29	Extracted Scattering Parameters: 3 Residuals in Fit	47
30	$\Lambda K_S^0(\bar{\Lambda} K_S^0)$ Fits with No Residuals	49
31	$\Lambda K^+(\bar{\Lambda} K^-)$ Fits, with NO residual correlations included, with No Residuals	50
32	$\Lambda K^-(\bar{\Lambda} K^+)$ Fits with No Residuals	51

33	Extracted Scattering Parameters: No Residuals in Fit . . . . .	53
34	$m_T$ Scaling of Radii: No Residuals in Fit . . . . .	53
35	$\Lambda(\bar{\Lambda})K_S^0$ Fits with 3 Residuals . . . . .	55
36	$\Lambda K^+(\bar{\Lambda} K^-)$ Fits with 3 Residuals . . . . .	56
37	$\Lambda K^-(\bar{\Lambda} K^+)$ Fits with 3 Residuals . . . . .	57
38	$\Lambda(\bar{\Lambda})K_S^0$ Fits showing 3 Residuals . . . . .	58
39	$\Lambda K^+(\bar{\Lambda} K^-)$ and $\Lambda K^-(\bar{\Lambda} K^+)$ Fits with 3 Residuals . . . . .	59
40	Extracted Scattering Parameters: 3 Residuals in Fit . . . . .	61
41	$m_T$ Scaling of Radii: 3 Residuals in Fit . . . . .	61
42	$\Lambda K_S^0(\bar{\Lambda} K_S^0)$ Fits with 10 Residuals . . . . .	63
43	$\Lambda K^+(\bar{\Lambda} K^-)$ Fits with 10 Residuals . . . . .	64
44	$\Lambda K^-(\bar{\Lambda} K^+)$ Fits with 10 Residuals . . . . .	65
45	$\Lambda(\bar{\Lambda})K_S^0$ Fits showing 10 Residuals . . . . .	66
46	$\Lambda K^+(\bar{\Lambda} K^-)$ and $\Lambda K^-(\bar{\Lambda} K^+)$ Fits with 10 Residuals . . . . .	67
47	Extracted Scattering Parameters: 3 Residuals in Fit . . . . .	69
48	$m_T$ Scaling of Radii: 10 Residuals in Fit . . . . .	69
49	Fit Results: Shared Radii and THERMINATOR 2 Background . . . . .	70
50	Compare Fit Parameters: Free vs fixed $\lambda$ . . . . .	71
51	Compare Fit Parameters: Shared vs unique $\lambda$ . . . . .	72
52	Compare Fit Parameters: Shared vs. Separate Radii . . . . .	73
53	Compare Fit Parameters: Compare number of residuals . . . . .	74
54	$\Xi K^\pm$ Results . . . . .	75
55	$\Xi K^\pm$ Data with Coulomb-Only Bands, 0-10% Centrality . . . . .	76
56	Effect of Strong Force Inclusion on Coulomb-Only Curve for $\Xi K^\pm$ systems . . . . .	77
57	$\Xi K^\pm$ Global Coulomb-Only Fit (Set 1) . . . . .	78
58	$\Xi K^\pm$ Global Coulomb-Only Fit (Set 2) . . . . .	79
59	$\Xi^- K^+$ Coulomb-Only Fit . . . . .	79
60	$\Xi^- K^-$ Coulomb-Only Fit . . . . .	80
61	Residuals: $\Sigma^0 K^+$ to $\Lambda K^+$ (0-10% Centrality) . . . . .	81
62	Residuals: $\Xi^0 K^+$ to $\Lambda K^+$ (0-10% Centrality) . . . . .	82
63	Residuals: $\Xi^- K^+$ to $\Lambda K^+$ (0-10% Centrality) . . . . .	82
64	Residuals: $\Sigma^{*+} K^+$ to $\Lambda K^+$ (0-10% Centrality) . . . . .	83
65	Residuals: $\Sigma^{*-} K^+$ to $\Lambda K^+$ (0-10% Centrality) . . . . .	83

66	Residuals: $\Sigma^{*0}K^+$ to $\Lambda K^+$ (0-10% Centrality) . . . . .	84
67	Residuals: $\Lambda K^{*0}$ to $\Lambda K^+$ (0-10% Centrality) . . . . .	84
68	Residuals: $\Sigma^0K^{*0}$ to $\Lambda K^+$ (0-10% Centrality) . . . . .	85
69	Residuals: $\Xi^0K^{*0}$ to $\Lambda K^+$ (0-10% Centrality) . . . . .	85
70	Residuals: $\Xi^-K^{*0}$ to $\Lambda K^+$ (0-10% Centrality) . . . . .	86
71	Residuals: $\Sigma^0K^-$ to $\Lambda K^-$ (0-10% Centrality) . . . . .	87
72	Residuals: $\Xi^0K^-$ to $\Lambda K^-$ (0-10% Centrality) . . . . .	88
73	Residuals: $\Xi^-K^-$ to $\Lambda K^-$ (0-10% Centrality) . . . . .	88
74	Residuals: $\Sigma^{*+}K^-$ to $\Lambda K^-$ (0-10% Centrality) . . . . .	89
75	Residuals: $\Sigma^{*-}K^-$ to $\Lambda K^-$ (0-10% Centrality) . . . . .	89
76	Residuals: $\Sigma^{*0}K^-$ to $\Lambda K^-$ (0-10% Centrality) . . . . .	90
77	Residuals: $\Lambda\bar{K}^{*0}$ to $\Lambda K^-$ (0-10% Centrality) . . . . .	90
78	Residuals: $\Sigma^0\bar{K}^{*0}$ to $\Lambda K^-$ (0-10% Centrality) . . . . .	91
79	Residuals: $\Xi^0\bar{K}^{*0}$ to $\Lambda K^-$ (0-10% Centrality) . . . . .	91
80	Residuals: $\Xi^-\bar{K}^{*0}$ to $\Lambda K^-$ (0-10% Centrality) . . . . .	92
81	Residuals: $\Sigma^0K_S^0$ to $\Lambda K_S^0$ (0-10% Centrality) . . . . .	93
82	Residuals: $\Xi^0K_S^0$ to $\Lambda K_S^0$ (0-10% Centrality) . . . . .	94
83	Residuals: $\Xi^-K_S^0$ to $\Lambda K_S^0$ (0-10% Centrality) . . . . .	94
84	Residuals: $\Sigma^{*+}K_S^0$ to $\Lambda K_S^0$ (0-10% Centrality) . . . . .	95
85	Residuals: $\Sigma^{*-}K_S^0$ to $\Lambda K_S^0$ (0-10% Centrality) . . . . .	95
86	Residuals: $\Sigma^{*0}K_S^0$ to $\Lambda K_S^0$ (0-10% Centrality) . . . . .	96
87	Residuals: $\Lambda K^{*0}$ to $\Lambda K_S^0$ (0-10% Centrality) . . . . .	96
88	Residuals: $\Sigma^0K^{*0}$ to $\Lambda K_S^0$ (0-10% Centrality) . . . . .	97
89	Residuals: $\Xi^0K^{*0}$ to $\Lambda K_S^0$ (0-10% Centrality) . . . . .	97
90	Residuals: $\Xi^-K^{*0}$ to $\Lambda K_S^0$ (0-10% Centrality) . . . . .	98

---

## 12 1 Introduction

13 We present results from a femtoscopic analysis of Lambda-Kaon correlations in Pb-Pb collisions at  $\sqrt{s_{NN}}$   
 14 = 2.76 TeV by the ALICE experiment at the LHC. All pair combinations of  $\Lambda$  and  $\bar{\Lambda}$  with  $K^+$ ,  $K^-$  and  
 15  $K_S^0$  are analyzed. The femtoscopic correlations are the result of strong final-state interactions, and are  
 16 fit with a parametrization based on a model by R. Lednicky and V. L. Lyuboshitz [1]. This allows us to  
 17 both characterize the emission source and measure the scattering parameters for the particle pairs. We  
 18 observe a large difference in the  $\Lambda$ - $K^+$  ( $\bar{\Lambda}$ - $K^-$ ) and  $\Lambda$ - $K^-$  ( $\bar{\Lambda}$ - $K^+$ ) correlations in pairs with low relative  
 19 momenta ( $k^* \lesssim 100$  MeV). Additionally, the average of the  $\Lambda$ - $K^+$  ( $\bar{\Lambda}$ - $K^-$ ) and  $\Lambda$ - $K^-$  ( $\bar{\Lambda}$ - $K^+$ ) correlation  
 20 functions is consistent with our  $\Lambda$ - $K_S^0$  ( $\bar{\Lambda}$ - $K_S^0$ ) measurement. The results suggest an effect arising from  
 21 different quark-antiquark interactions in the pairs, i.e.  $s\bar{s}$  in  $\Lambda$ - $K^+$  ( $\bar{\Lambda}$ - $K^-$ ) and  $u\bar{u}$  in  $\Lambda$ - $K^-$  ( $\bar{\Lambda}$ - $K^+$ ). To  
 22 gain further insight into this hypothesis, we currently are conducting a  $\Xi$ -K femtoscopic analysis.

## 23 2 Data Sample and Software

### 24 2.1 Data Sample

25 The analysis used “pass 2” reconstructed Pb-Pb data from LHC11h (AOD145). The runlist was selected  
 26 from runs with global quality tag “1” in the ALICE Run Condition Table. Approximately 40 million  
 27 combined central, semi-central, and minimum bias events were analyzed. Runs from both positive (++)  
 28 and negative (--) magnetic field polarity settings were used.

29 Run list: 170593, 170572, 170388, 170387, 170315, 170313, 170312, 170311, 170309, 170308, 170306,  
 30 170270, 170269, 170268, 170230, 170228, 170207, 170204, 170203, 170193, 170163, 170159, 170155,  
 31 170091, 170089, 170088, 170085, 170084, 170083, 170081, 170040, 170027, 169965, 169923, 169859,  
 32 169858, 169855, 169846, 169838, 169837, 169835, 169591, 169590, 169588, 169587, 169586, 169557,  
 33 169555, 169554, 169553, 169550, 169515, 169512, 169506, 169504, 169498, 169475, 169420, 169419,  
 34 169418, 169417, 169415, 169411, 169238, 169167, 169160, 169156, 169148, 169145, 169144, 169138,  
 35 169099, 169094, 169091, 169045, 169044, 169040, 169035, 168992, 168988, 168826, 168777, 168514,  
 36 168512, 168511, 168467, 168464, 168460, 168458, 168362, 168361, 168342, 168341, 168325, 168322,  
 37 168311, 168310, 168315, 168108, 168107, 168105, 168076, 168069, 167988, 167987, 167985, 167920,  
 38 167915

39 Analysis was also performed on the LHC12a17a\_fix (AOD149) Monte Carlo HIJING events for certain  
 40 checks. THERMINATOR2 was also used for certain aspects, such as transform matrices described feed-  
 41 down contributions.

### 42 2.2 Software

43 The analysis was performed on the PWGCF analysis train using AliRoot v5-08-18-1 and AliPhysics  
 44 vAN-20161027-1.

45 The main classes utilized include: AliFemtoVertexMultAnalysis, AliFemtoEventCutEstimators, AliFem-  
 46 toESDTrackCutNSigmaFilter, AliFemtoV0TrackCutNSigmaFilter, AliFemtoXiTrackCut, AliFemtoV0PairCut,  
 47 AliFemtoV0TrackPairCut, AliFemtoXiTrackPairCut, and AliFemtoAnalysisLambdaKaon. All of these  
 48 classes are contained in /AliPhysics/PWGCF/FEMTOSCOPY/AliFemto and .../AliFemtoUser.

## 49 3 Data Selection

### 50 3.1 Event Selection and Mixing

51 The events used in this study were selected with the class AliFemtoEventCutEstimators according to the  
 52 following criteria:

- 53        – Triggers
- 54            – minimum bias (kMB)
- 55            – central (kCentral)
- 56            – semi-central (kSemiCentral)
- 57        – z-position of reconstructed event vertex must be within 10 cm of the center of the ALICE detector
- 58        – the event must contain at least one particle of each type from the pair of interest
- 59     The event mixing was handled by the AliFemtoVertexMultAnalysis class, which only mixes events with
- 60     like vertex position and centrality. The following criteria were used for event mixing:
- 61            – Number of events to mix = 5
- 62            – Vertex position bin width = 2 cm
- 63            – Centrality bin width = 5
- 64     The AliFemtoEventReaderAODChain class is used to read the events. Event flattening is not currently
- 65     used. FilterBit(7). The centrality is determined by the “V0M” method of AliCentrality, set by calling Al-
- 66     iFemtoEventReaderAOD::SetUseMultiplicity(kCentrality). I utilize the SetPrimaryVertexCorrectionT-
- 67     PCPoints switch, which causes the reader to shift all TPC points to be relative to the event vertex.
- 68     **3.2 K<sup>±</sup> Track Selection**
- 69     Charged kaons are identified using the AliFemtoESDTrackCutNSigmaFilter class. The specific cuts used
- 70     in this analysis are as follows:
- 71     Track Selection:
- 72            – Kinematic range:
- 73                  –  $0.14 < p_T < 1.5 \text{ GeV}/c$
- 74                  –  $|\eta| < 0.8$
- 75            – FilterBit(7)
- 76                  – TPC tracks
- 77            – Track Quality
- 78                  – Minimum number of clusters in the TPC (fminTPCncls) = 80
- 79                  – Maximum allowed  $\chi^2/N_{DOF}$  for ITS clusters = 3.0
- 80                  – Maximum allowed  $\chi^2/N_{DOF}$  for TPC clusters = 4.0
- 81            – Primary Particle Selection:
- 82                  – Maximum XY impact parameter = 2.4 cm
- 83                  – Maximum Z impact parameter = 3.0 cm
- 84            – Remove particles with any kink labels (fRemoveKinks = true)
- 85            – Maximum allowed sigma to primary vertex (fMaxSigmaToVertex) = 3.0

86 K $^\pm$  Identification:

87 – PID Probabilities:

- 88 – K: > 0.2
- 89 –  $\pi$ : < 0.1
- 90 –  $\mu$ : < 0.8
- 91 – p: < 0.1

92 – Most probable particle type must be Kaon (fMostProbable=3)

93 – TPC and TOF N $_\sigma$  cuts:

- 94 –  $p < 0.4 \text{ GeV}/c$ : N $_{\sigma K, \text{TPC}} < 2$
- 95 –  $0.4 < p < 0.45 \text{ GeV}/c$ : N $_{\sigma K, \text{TPC}} < 1$
- 96 –  $0.45 < p < 0.8 \text{ GeV}/c$ : N $_{\sigma K, \text{TPC}} < 3 \& N_{\sigma K, \text{TOF}} < 2$
- 97 –  $0.8 < p < 1.0 \text{ GeV}/c$ : N $_{\sigma K, \text{TPC}} < 3 \& N_{\sigma K, \text{TOF}} < 1.5$
- 98 –  $p > 1.0 \text{ GeV}/c$ : N $_{\sigma K, \text{TPC}} < 3 \& N_{\sigma K, \text{TOF}} < 1$

99 – Electron Rejection: Reject if N $_{\sigma e^-, \text{TPC}} < 3$

100 – Pion Rejection: Reject if:

- 101 –  $p < 0.65 \text{ GeV}/c$ 
  - 102 \* if TOF and TPC available: N $_{\sigma \pi, \text{TPC}} < 3 \& N_{\sigma \pi, \text{TOF}} < 3$
  - 103 \* else
    - 104 ·  $p < 0.5 \text{ GeV}/c$ : N $_{\sigma \pi, \text{TPC}} < 3$
    - 105 ·  $0.5 < p < 0.65 \text{ GeV}/c$ : N $_{\sigma \pi, \text{TPC}} < 2$
- 106 –  $0.65 < p < 1.5 \text{ GeV}/c$ : N $_{\sigma \pi, \text{TPC}} < 5 \& N_{\sigma \pi, \text{TOF}} < 3$
- 107 –  $p > 1.5 \text{ GeV}/c$ : N $_{\sigma \pi, \text{TPC}} < 5 \& N_{\sigma \pi, \text{TOF}} < 2$

108 The purity of the K $^\pm$  collections was estimated using the MC data, for which the true identity of each  
109 reconstructed K $^\pm$  particle is known. Therefore, the purity may be estimated as:

$$\text{Purity}(K^\pm) = \frac{N_{\text{true}}}{N_{\text{reconstructed}}} \quad (1)$$

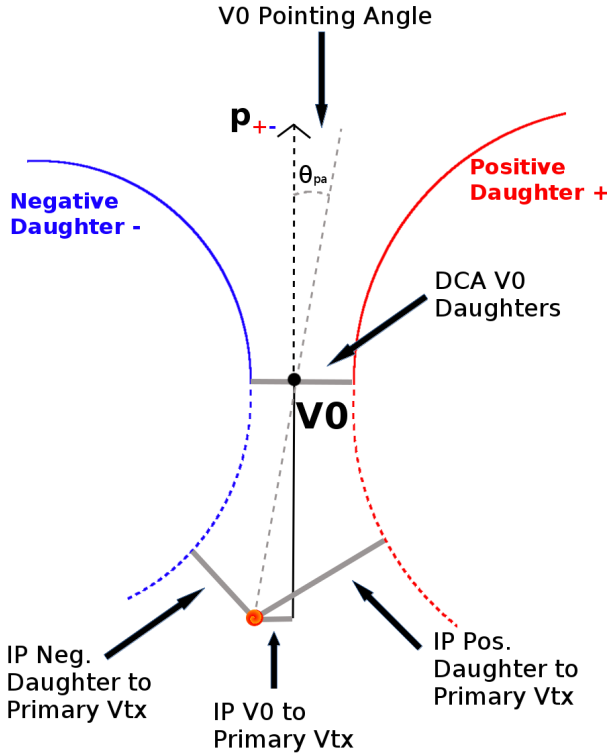
110 Purity(K $^+$ )  $\approx$  Purity(K $^-$ )  $\approx$  97%

### 111 3.3 V0 Selection

112  $\Lambda$  ( $\bar{\Lambda}$ ) and K $_S^0$  are neutral particles which cannot be directly detected, but must instead be reconstructed  
113 through detection of their decay products, or daughters. This process is illustrated in Figure 1. In  
114 general, particles which are topologically reconstructed in this fashion are called V0 particles. The  
115 class AliFemtoV0TrackCutNSigmaFilter (which is an extension of AliFemtoV0TrackCut) is used to  
116 reconstruct the V0s.

117 In order to obtain a true and reliable signal, one must ensure good purity of the V0 collection. The purity  
118 of the collection is calculated as:

$$\text{Purity} = \frac{\text{Signal}}{\text{Signal} + \text{Background}} \quad (2)$$



**Fig. 1:** V0 Reconstruction

119 To obtain both the signal and background, the invariant mass distribution ( $m_{\text{inv}}$ ) of all V0 candidates  
 120 must be constructed immediately before the final invariant mass cut. Examples of such distributions can  
 121 be found in Figures 3 and 5. It is vital that this distribution be constructed immediately before the final  
 122  $m_{\text{inv}}$  cut, otherwise it would be impossible to estimate the background. As shown in Figures 3 and 5, the  
 123 background is fit (with a polynomial) outside of the peak region of interest to obtain an estimate for the  
 124 background within the region. Within the  $m_{\text{inv}}$  cut limits, the background is the region below the fit while  
 125 the signal is the region above the fit.

### 126 3.3.1 **Λ Reconstruction**

127 The following cuts were used to select good  $\Lambda$  ( $\bar{\Lambda}$ ) candidates:

128 1. Daughter Particle Cuts

129 (a) Cuts Common to Both Daughters

- 130 i.  $|\eta| < 0.8$
- 131 ii. SetTPCnclsDaughters(80)
- 132 iii. SetStatusDaughters(AliESDtrack::kTPCrefit)
- 133 iv. DCA  $\pi p$  Daughters  $< 0.4$  cm

134 (b) Pion Specific Daughter Cuts

- 135 i.  $p_T > 0.16$  GeV/c
- 136 ii. DCA to prim vertex  $> 0.3$  cm
- 137 iii. TPC and TOF N $\sigma$  Cuts
  - 138 A.  $p < 0.5$  GeV/c : N $\sigma_{\text{TPC}} < 3$
  - 139 B.  $p > 0.5$  GeV/c :

- if TOF & TPC available:  $N\sigma_{\text{TPC}} < 3$  &  $N\sigma_{\text{TOF}} < 3$
- else  $N\sigma_{\text{TOF}} < 3$

142 (c) Proton Specific Daughter Cuts

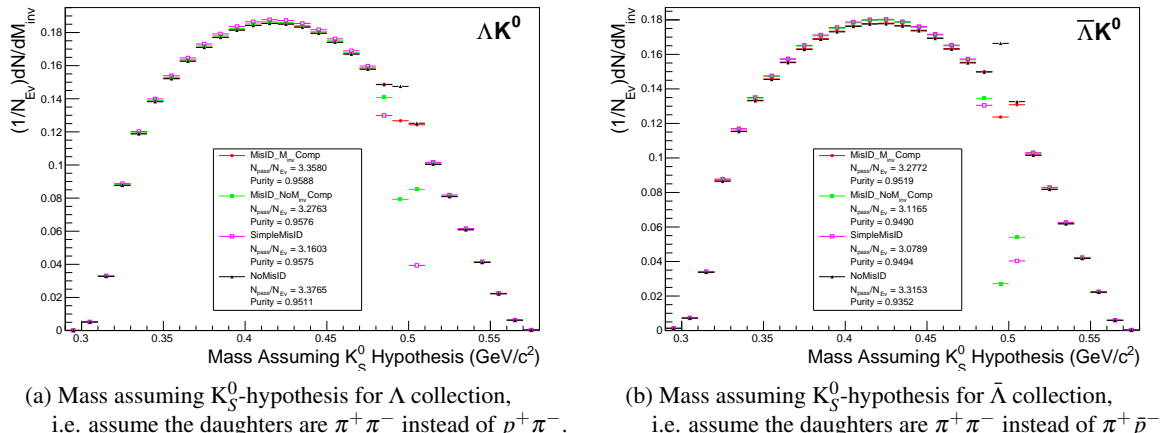
- i.  $p_T > 0.5(p)[0.3(\bar{p})] \text{ GeV}/c$
- ii. DCA to prim vertex  $> 0.1 \text{ cm}$
- iii. TPC and TOF  $N\sigma$  Cuts
  - A.  $p < 0.8 \text{ GeV}/c : N\sigma_{\text{TPC}} < 3$
  - B.  $p > 0.8 \text{ GeV}/c :$ 
    - if TOF & TPC available:  $N\sigma_{\text{TPC}} < 3$  &  $N\sigma_{\text{TOF}} < 3$
    - else  $N\sigma_{\text{TOF}} < 3$

150 2. V0 Cuts

- (a)  $|\eta| < 0.8$
- (b)  $p_T > 0.4 \text{ GeV}/c$
- (c)  $|m_{\text{inv}} - m_{\text{PDG}}| < 3.8 \text{ MeV}$
- (d) DCA to prim. vertex  $< 0.5 \text{ cm}$
- (e) Cosine of pointing angle  $> 0.9993$
- (f) OnFlyStatus = false
- (g) Decay Length  $< 60 \text{ cm}$

155 3. Shared Daughter Cut for V0 Collection

- Iterate through V0 collection to ensure that no daughter is used in more than one V0 candidate

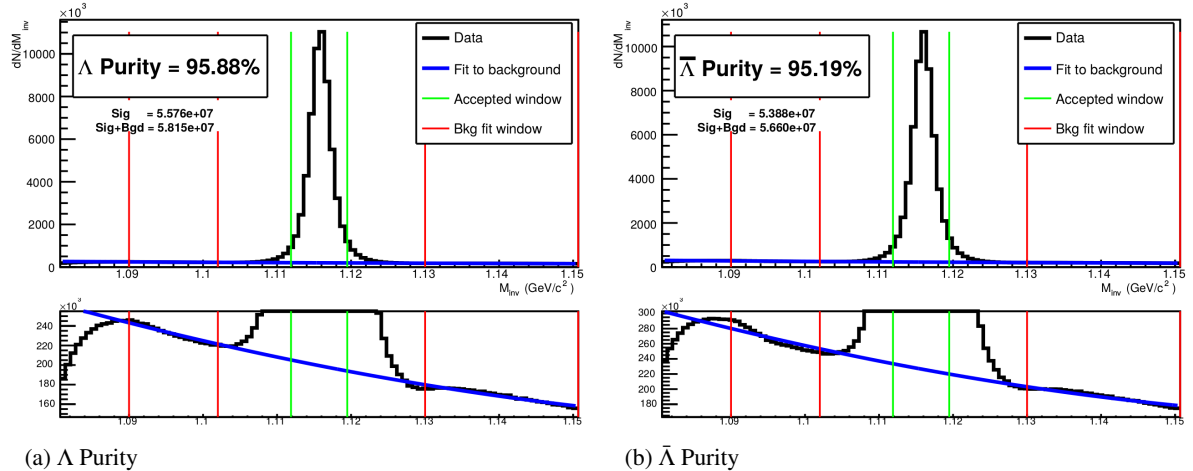


**Fig. 2:** Mass assuming  $K_S^0$ -hypothesis for V0 candidates passing all  $\Lambda$  (2a) and  $\bar{\Lambda}$  (2b) cuts. The “NoMisID” distribution (black triangles) uses the V0 finder without any attempt to remove misidentified  $K_S^0$ . The slight peak in the “NoMisID” distribution around  $m_{\text{inv}} = 0.5 \text{ GeV}/c^2$  contains misidentified  $K_S^0$  particles in our  $\Lambda(\bar{\Lambda})$  collection. “SimpleMisID” (pink squares) simply cuts out the entire peak, which throws away some good  $\Lambda$  and  $\bar{\Lambda}$  particles. “MisID\_NoM<sub>inv</sub>Comp” (green squares) uses the misidentification cut outlined in the text, but does not utilize the invariant mass comparison method. “MisID\_M<sub>inv</sub>Comp” (red circles) utilizes the full misidentification methods, and is currently used for this analysis. “ $N_{\text{pass}}/N_{\text{ev}}$ ” is the total number of  $\Lambda(\bar{\Lambda})$  particles found, normalized by the total number of events. The purity of the collection is also listed.

Figure 2a shows the mass assuming  $K_S^0$  hypothesis for the  $\Lambda$  collection, i.e. assume the daughters are  $\pi^+\pi^-$  instead of  $\pi^+\bar{p}$ . Figure 2b is a similar plot, but is for the  $\bar{\Lambda}$  collection, i.e. assume the daughters are  $\pi^+\pi^-$  instead of  $\pi^+\bar{p}$ . The  $K_S^0$  contamination is visible, although not profound, in both in the slight peaks around  $m_{\text{inv}} = 0.497 \text{ GeV}/c^2$ . If one simply cuts out the entire peak, good  $\Lambda$  particles will be lost. Ideally, the  $\Lambda$  selection and  $K_S^0$  misidentification cuts are selected such that the peak is removed from this plot while leaving the distribution continuous. To attempt to remove these  $K_S^0$  contaminations without throwing away good  $\Lambda$  and  $\bar{\Lambda}$  particles, the following misidentification cuts are imposed; a  $\Lambda(\bar{\Lambda})$  candidate is rejected if all of the following criteria are satisfied:

- $|m_{\text{inv}, K_S^0 \text{ Hypothesis}} - m_{\text{PDG}, K_S^0}| < 9.0 \text{ MeV}/c^2$
- Positive and negative daughters pass  $\pi$  daughter cut implemented for  $K_S^0$  reconstruction
- $|m_{\text{inv}, K_S^0 \text{ Hypothesis}} - m_{\text{PDG}, K_S^0}| < |m_{\text{inv}, \Lambda(\bar{\Lambda}) \text{ Hypothesis}} - m_{\text{PDG}, \Lambda(\bar{\Lambda})}|$

Figure 3 shows the invariant mass ( $m_{\text{inv}}$ ) distribution of all  $\Lambda(\bar{\Lambda})$  candidates immediately before the final invariant mass cut. These distributions are used to calculate the collection purities. The  $\Lambda$  and  $\bar{\Lambda}$  purities are found to be:  $\text{Purity}(\Lambda) \approx \text{Purity}(\bar{\Lambda}) \approx 95\%$ .



**Fig. 3:** Invariant mass ( $m_{\text{inv}}$ ) distribution of all  $\Lambda$  (a) and  $\bar{\Lambda}$  (b) candidates immediately before the final invariant mass cut. The bottom figures are zoomed to show the background with fit. The vertical green lines represent the  $m_{\text{inv}}$  cuts used in the analyses, the red vertical lines delineate the region over which the background was fit, and the blue line shows the background fit. These distributions are used to calculate the collection purities,  $\text{Purity}(\Lambda) \approx \text{Purity}(\bar{\Lambda}) \approx 95\%$ .

### 3.3.2 $K_S^0$ Reconstruction

The following cuts were used to select good  $K_S^0$  candidates:

#### 1. Pion Daughter Cuts

- (a)  $|\eta| < 0.8$
- (b) SetTPCnclsDaughters(80)
- (c) SetStatusDaughters(AliESDtrack::kTPCrefic)
- (d) DCA  $\pi^+\pi^-$  Daughters  $< 0.3 \text{ cm}$

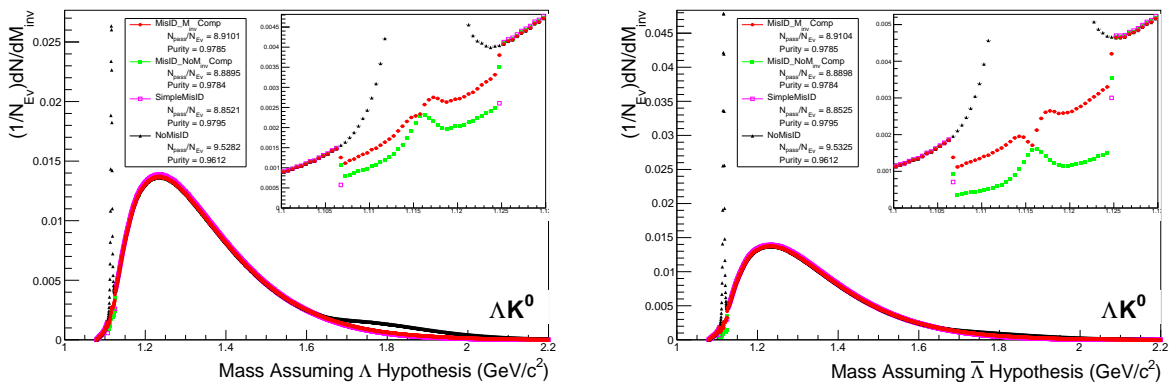
- (e)  $p_T > 0.15 \text{ GeV}/c$   
(f) DCA to prim vertex  $> 0.3 \text{ cm}$   
(g) TPC and TOF  $N\sigma$  Cuts  
i.  $p < 0.5 \text{ GeV}/c : N\sigma_{\text{TPC}} < 3$   
ii.  $p > 0.5 \text{ GeV}/c :$   
– if TOF & TPC available:  $N\sigma_{\text{TPC}} < 3 \& N\sigma_{\text{TOF}} < 3$   
– else  $N\sigma_{\text{TOF}} < 3$

## 2. $K_S^0$ Cuts

- (a)  $|\eta| < 0.8$   
(b)  $p_T > 0.2 \text{ GeV}/c$   
(c)  $m_{\text{PDG}} - 13.677 \text{ MeV} < m_{\text{inv}} < m_{\text{PDG}} + 2.0323 \text{ MeV}$   
(d) DCA to prim. vertex  $< 0.3 \text{ cm}$   
(e) Cosine of pointing angle  $> 0.9993$   
(f) OnFlyStatus = false  
(g) Decay Length  $< 30 \text{ cm}$

## 3. Shared Daughter Cut for V0 Collection

- Iterate through V0 collection to ensure that no daughter is used in more than one V0 candidate



(a) Mass assuming  $\Lambda$ -hypothesis for  $K_S^0$  collection, i.e. assume the daughters are  $p^+\pi^-$  instead of  $\pi^+\pi^-$ .

(b) Mass assuming  $\bar{\Lambda}$ -hypothesis for  $K_S^0$  collection, i.e. assume the daughters are  $\pi^+\bar{p}^-$  instead of  $\pi^+\pi^-$ .

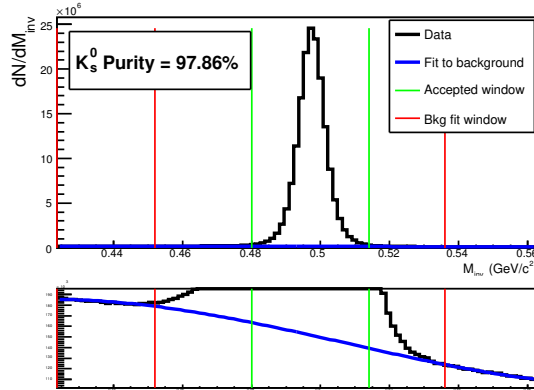
**Fig. 4:** Mass assuming  $\Lambda$ -hypothesis (4a) and  $\bar{\Lambda}$ -hypothesis (4b) for  $K_S^0$  collection. The “NoMisID” distribution (black triangles) uses the V0 finder without any attempt to remove misidentified  $\Lambda$  and  $\bar{\Lambda}$ . The peak in the “NoMisID” distribution around  $m_{\text{inv}} = 1.115 \text{ GeV}/c^2$  contains misidentified  $\Lambda$  (4a) and  $\bar{\Lambda}$  (4b) particles in our  $K_S^0$  collection. “SimpleMisID” (pink squares) simply cuts out the entire peak, which throws away some good  $K_S^0$  particles. “MisID\_NoM<sub>inv</sub>Comp” (green squares) uses the misidentification cut outlined in the text, but does not utilize the invariant mass comparison method. “MisID\_M<sub>inv</sub>Comp” (red circles) utilizes the full misidentification methods, and is currently used for this analysis. “ $N_{\text{pass}}/N_{\text{ev}}$ ” is the total number of  $K_S^0$  particles found, normalized by the total number of events. The purity of the collection is also listed. Also note, the relative excess of the “NoMisID” distribution around  $1.65 < m_{\text{inv}} < 2.1 \text{ GeV}/c^2$  shows misidentified  $\bar{\Lambda}$  (4a) and  $\Lambda$  (4b) particles in our  $K_S^0$  collection.

As can be seen in Figure 4, some misidentified  $\Lambda$  and  $\bar{\Lambda}$  particles contaminate our  $K_S^0$  sample. Figure 4a shows the mass assuming  $\Lambda$ -hypothesis for the  $K_S^0$  collection, i.e. assume the daughters are  $p^+\pi^-$

instead of  $\pi^+\pi^-$ . Figure 4b is similar, but shows the mass assuming  $\bar{\Lambda}$  hypothesis for the collection, i.e. assume the daughters are  $\pi^+\bar{p}^-$  instead of  $\pi^+\pi^-$ . The  $\Lambda$  contamination can be seen in 4a, and the  $\bar{\Lambda}$  contamination in 4b, in the peaks around  $m_{\text{inv}} = 1.115 \text{ GeV}/c^2$ . Additionally, the  $\bar{\Lambda}$  contamination is visible in Figure 4a, and the  $\Lambda$  contamination visible in Figure 4b, in the region of excess around  $1.65 < m_{\text{inv}} < 2.1 \text{ GeV}/c^2$ . This is confirmed as the number of misidentified  $\Lambda$  particles in the sharp peak of Figure 4a (misidentified  $\bar{\Lambda}$  particles in the sharp peak of Figure 4b) approximately equals the excess found in the  $1.65 < m_{\text{inv}} < 2.1 \text{ GeV}/c^2$  region of Figure 4a (Figure 4b).

The peaks around  $m_{\text{inv}} = 1.115 \text{ GeV}/c^2$  in Figure 4 contain both misidentified  $\Lambda$  ( $\bar{\Lambda}$ ) particles and good  $K_S^0$ . If one simply cuts out the entire peak, some good  $K_S^0$  particles will be lost. Ideally, the  $K_S^0$  selection and  $\Lambda(\bar{\Lambda})$  misidentification cuts can be selected such that the peak is removed from this plot while leaving the distribution continuous. To attempt to remove these  $\Lambda$  and  $\bar{\Lambda}$  contaminations without throwing away good  $K_S^0$  particles, the following misidentification cuts are imposed; a  $K_S^0$  candidate is rejected if all of the following criteria are satisfied (for either  $\Lambda$  or  $\bar{\Lambda}$  hypothesis):

- $|m_{\text{inv}, \Lambda(\bar{\Lambda}) \text{ Hypothesis}} - m_{\text{PDG}, \Lambda(\bar{\Lambda})}| < 9.0 \text{ MeV}/c^2$
- Positive daughter passes  $p^+(\pi^+)$  daughter cut implemented for  $\Lambda(\bar{\Lambda})$  reconstruction
- Negative daughter passes  $\pi^-(\bar{p}^-)$  daughter cut implemented by  $\Lambda(\bar{\Lambda})$  reconstruction
- $|m_{\text{inv}, \Lambda(\bar{\Lambda}) \text{ Hypothesis}} - m_{\text{PDG}, \Lambda(\bar{\Lambda})}| < |m_{\text{inv}, K_S^0 \text{ Hypothesis}} - m_{\text{PDG}, K_S^0}|$



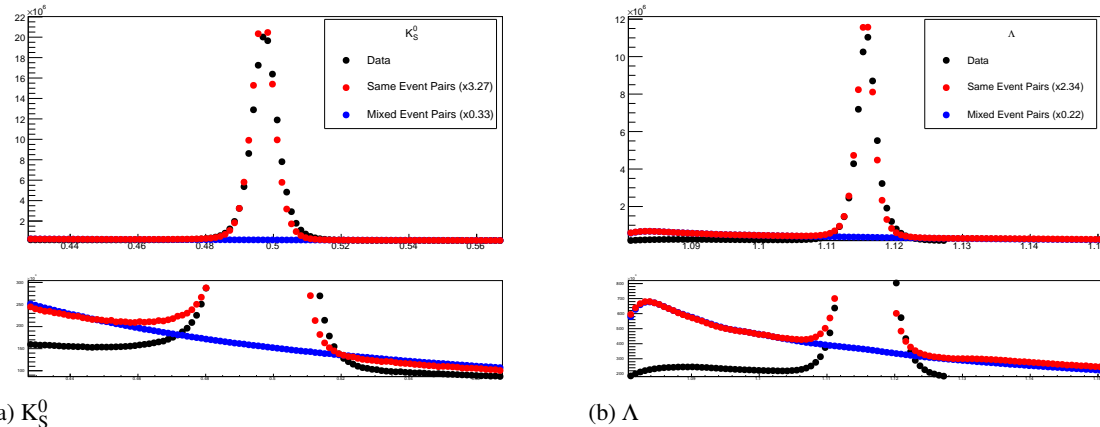
**Fig. 5:** Invariant mass ( $m_{\text{inv}}$ ) distribution of all  $K_S^0$  candidates immediately before the final invariant mass cut. The bottom figure is zoomed to show the background with fit. The vertical green lines represent the  $m_{\text{inv}}$  cut used in the analyses, the red vertical lines delineate the region over which the background was fit, and the blue line shows the background fit. This distribution is used to calculate the collection purity,  $\text{Purity}(K_S^0) \approx 98\%$ .

### 3.3.3 V0 Purity Background Estimation

As previously stated, the backgrounds in the  $m_{\text{inv}}$  distributions are fit with a polynomial outside of the final cut region in an attempt to estimate the background within the cut region. As this estimation of the background under the mass peak is vital in our estimation of our V0 purity, it is important for us to ensure that our estimation is accurate. More specifically, it is necessary that we ensure the background is well described by a polynomial fit within the cut region.

To better understand our background, we studied V0 candidates reconstructed with daughters from different events. These mixed-event V0s certainly do not represent real, physical V0s (a single V0 cannot have daughters living in two different events!), but rather represents a large portion of the background creeping into our analysis.

The standard AliFemto framework is not equipped to handle this situation, as most are not interested in these fake-V0s. Therefore, we built the AliFemtoV0PurityBgdEstimator class. In addition to finding fake-V0s using mixed-event daughters, we also used our AliFemtoV0PurityBgdEstimator class to find real-V0s using same-event daughters. The purpose here was to compare our simple V0 finder (in AliFemtoV0PurityBgdEstimator) to the established V0 finder used in standard AliFemto analyses.



**Fig. 6:** V0 Purity Background Estimation. The black points, marked "Data", correspond to real V0s found using the standard V0-finder (i.e. the V0s used in my analyses). The red points, marked "Same Event Pairs", show real V0s reconstructed with our personal V0-finder in AliFemtoV0PurityBgdEstimator. These data are scaled by a factor (listed in the legend) to match their *Signal + Background* value in the cut region with that of the data. The blue points, marked "Mixed Event Pairs", show fake-V0s reconstructed with our personal V0-finder using mixed-event daughters. The blue points are scaled by a factor (listed in the legend) to closely match the red points in the side-band region.

Figure 6 shows the results of our study. In the figures, the black points, marked "Data", correspond to V0s found using the standard V0-finder, and to the V0s used in my analyses. The red points show real V0s reconstructed with our personal V0-finder (in AliFemtoV0PurityBgdEstimator) using same-event daughters, and the blue points show fake-V0s reconstructed with our personal V0-finder using mixed-event daughters. Both the red and blue points have been scaled by different factors (listed in the figure's legends) to nicely align all three data on a single plot.

Figure 6 shows that our personal V0-finder does a good, but not perfect, job of matching the shape of the  $m_{inv}$  plots obtained from the data. The scale factor listed in the legend reveals that we are only finding 1/3 - 1/2 of the V0s found by the standard V0-finder. These two points are not of concern, as our purpose here was to gain a sense of the broad shape of the background. It is revealed in Fig. 6, when studying the red and blue points, that the background distribution within the mass peak region is simply a smooth connection of the backgrounds outside of the cut region. Therefore, our method of fitting the background outside of the cut region, fitting with a smooth polynomial, and extrapolating to the cut region is justified.

### 3.4 Cascade Reconstruction

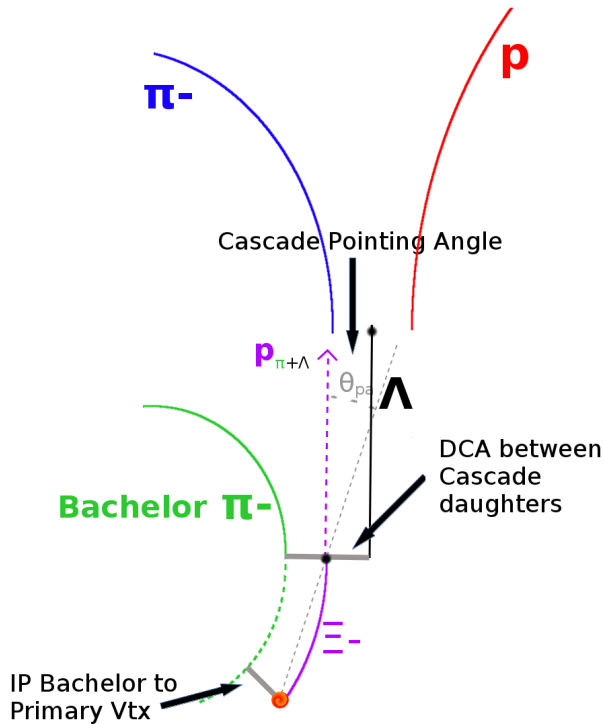
Our motivation for studying  $\Xi K^\pm$  systems is to hopefully better understand the striking difference in the  $\Lambda K^+$  and  $\Lambda K^-$  data at low  $k^*$  (Figure 13).

The reconstruction of  $\Xi$  particles is one step above V0 reconstruction. V0 particles are topologically reconstructed by searching for the charged daughters' tracks into which they decay. With  $\Xi$  particles, we search for the V0 particle and charged daughter into which the  $\Xi$  decays. In the case of  $\Xi^-$ , we search for the  $\Lambda$  (V0) and  $\pi^-$  (track) daughters. We will refer to this  $\pi$  as the "bachelor  $\pi$ ".

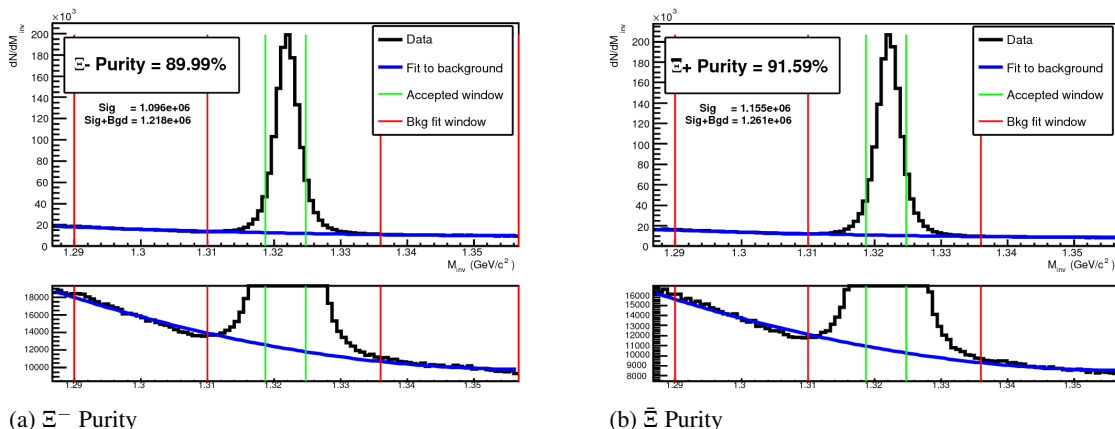
The following cuts were used to select good  $\Xi^-$  ( $\bar{\Xi}^+$ ) candidates:

- 253        1. V0 Daughter Reconstruction
- 254            (a) V0 Daughter Particle Cuts
- 255              i. Cuts Common to Both Daughters
- 256               A.  $|\eta| < 0.8$
- 257               B. SetTPCnclsDaughters(80)
- 258               C. SetStatusDaughters(AliESDtrack::kTPCrefic)
- 259               D. SetMaxDcaV0Daughters(0.4)
- 260              ii. Pion Specific Daughter Cuts
- 261               A.  $p_T > 0.16$
- 262               B. DCA to prim vertex  $> 0.3$
- 263              iii. Proton Specific Daughter Cuts
- 264               A.  $p_T > 0.5(p) [0.3(\bar{p})] \text{ GeV}/c$
- 265               B. DCA to prim vertex  $> 0.1$
- 266            (b) V0 Cuts
- 267              i.  $|\eta| < 0.8$
- 268              ii.  $p_T > 0.4 \text{ GeV}/c$
- 269              iii.  $|m_{inv} - m_{PDG}| < 3.8 \text{ MeV}$
- 270              iv. DCA to prim. vertex  $> 0.2 \text{ cm}$
- 271              v. Cosine of pointing angle to  $\Xi$  decay vertex  $> 0.9993$
- 272              vi. OnFlyStatus = false
- 273              vii. Decay Length  $< 60 \text{ cm}$
- 274              viii. The misidentification cuts described in Section 3.3.1 are utilized
- 275        2. Bachelor  $\pi$  Cuts
- 276            (a)  $|\eta| < 0.8$
- 277            (b)  $p_T < 100 \text{ GeV}/c$
- 278            (c) DCA to prim vertex  $> 0.1 \text{ cm}$
- 279            (d) SetTPCnclsDaughters(70)
- 280            (e) SetStatusDaughters(AliESDtrack::kTPCrefic)
- 281        3.  $\Xi$  Cuts
- 282            (a)  $|\eta| < 0.8$
- 283            (b)  $0.8 < p_T < 100 \text{ GeV}/c$
- 284            (c)  $|m_{inv} - m_{PDG}| < 3.0 \text{ MeV}$
- 285            (d) DCA to prim. vertex  $< 0.3 \text{ cm}$
- 286            (e) Cosine of pointing angle  $> 0.9992$
- 287        4. Shared Daughter Cut for  $\Xi$  Collection
- 288            – Iterate through  $\Xi$  collection to ensure that no daughter is used in more than one  $\Xi$  candidate

289        The purity of our  $\Xi$  and  $\bar{\Xi}$  collections are calculated just as those of our V0 collections 3.3. Figure 8,  
290        which is used to calculate the purity, shows the  $m_{inv}$  distribution of our  $\Xi(\bar{\Xi})$  candidates just before the  
291        final  $m_{inv}$  cut. Currently, we have  $\text{Purity}(\Xi^-) \approx 90\%$  and  $\text{Purity}(\bar{\Xi}^+) \approx 92\%$ .



**Fig. 7:**  $\Xi$  Reconstruction



**Fig. 8:**  $\Xi^- (\bar{\Xi}^+)$  Purity 0-10%: Purity( $\Xi^-$ )  $\approx$  90% and Purity( $\bar{\Xi}^+$ )  $\approx$  92%.

### 292    3.5 Pair Selection

293    It is important to obtain true particle pairs in the analysis. In particular, contamination from pairs constructed with split or merged tracks, and pairs sharing daughters, can introduce an artificial signal into  
294    the correlation function, obscuring the actual physics.  
295

296    1. Shared Daughter Cut for Pairs

297        (a) V0-V0 Pairs (i.e.  $\Lambda(\bar{\Lambda})K_S^0$  analyses)

- 298            – Remove all pairs which share a daughter
  - 299              – Ex.  $\Lambda$  and  $K_S^0$  particles which share a  $\pi^-$  daughter are not included

300        (b) V0-Track Pairs (i.e.  $\Lambda(\bar{\Lambda})K^\pm$  analyses)

- 301           – Remove pairs if Track is also used as a daughter of the V0  
 302            – In these analyses, this could only occur if, for instance, a  $K$  is misidentified as a  $\pi$   
 303            or  $p$  in the V0 reconstruction

304       (c)  $\Xi$ -Track Pairs

- 305           – Remove pairs if Track is also used as a daughter of the  $\Xi$   
 306            – In these analyses, this could only occur if, for instance, a  $K$  is misidentified as a  $\pi$   
 307            or  $p$  in the V0 reconstruction, or misidentified as bachelor  $\pi$ .  
 308           – Remove pair if bachelor  $\pi$  is also a daughter of the  $\Lambda$   
 309            – This is not a pair cut, but is included here because this cut occurs in the  
 310              AliFemtoXiTrackPairCut class

311       2. Average Separation Cuts

- 312           – Used to cut out splitting and merging effects  
 313           – The motivation for these cuts can be seen in Figures 9, 10, and 11, in which average separa-  
 314           tion correlation functions are presented

315       (a)  $\Lambda(\bar{\Lambda})K_S^0$  Analyses

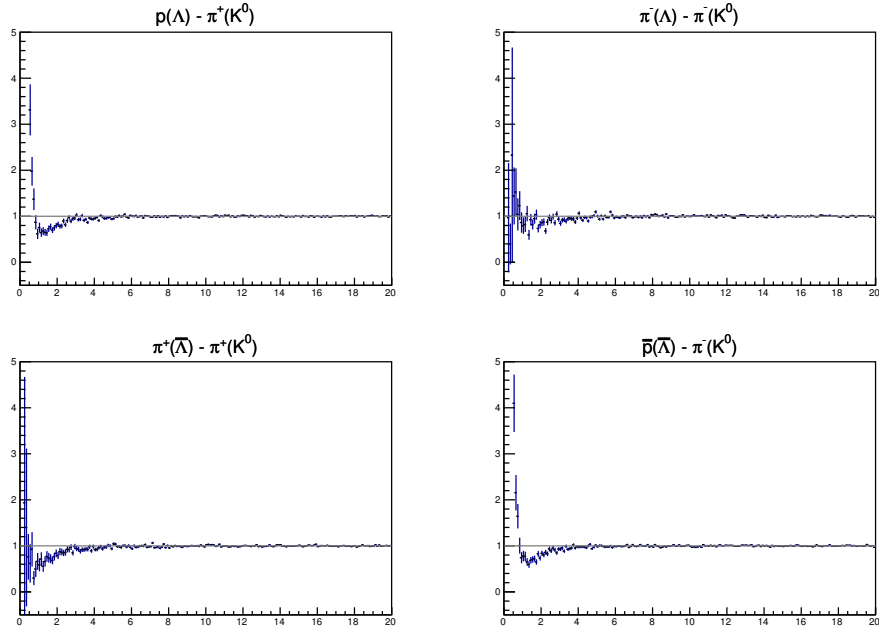
- 316           – Average separation  $> 6.0$  cm for like charge sign daughters  
 317            – ex.  $p$  daughter of  $\Lambda$  and  $\pi^+$  daughter of  $K_S^0$   
 318            – No cut for unlike-sign daughters

319       (b)  $\Lambda(\bar{\Lambda})K^\pm$  Analyses

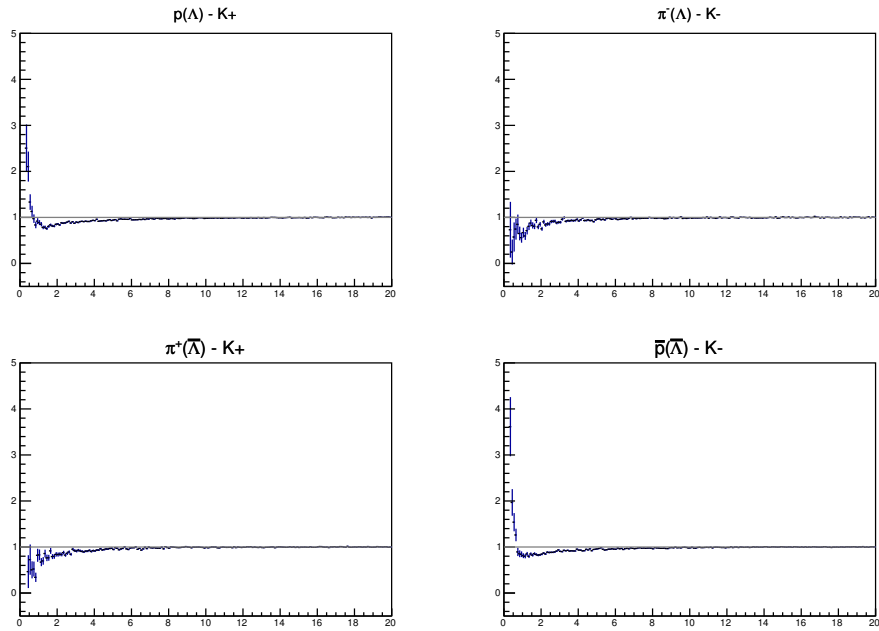
- 320           – Average Separation  $> 8.0$  cm for daughter of  $\Lambda(\bar{\Lambda})$  sharing charge sign of  $K^\pm$   
 321            – ex. in  $\Lambda K^+$  analysis,  $p$  daughter of  $\Lambda$  with  $K^+$   
 322            – No cut for unlike signs

323       (c)  $\Xi(\bar{\Xi})K^\pm$  Analyses

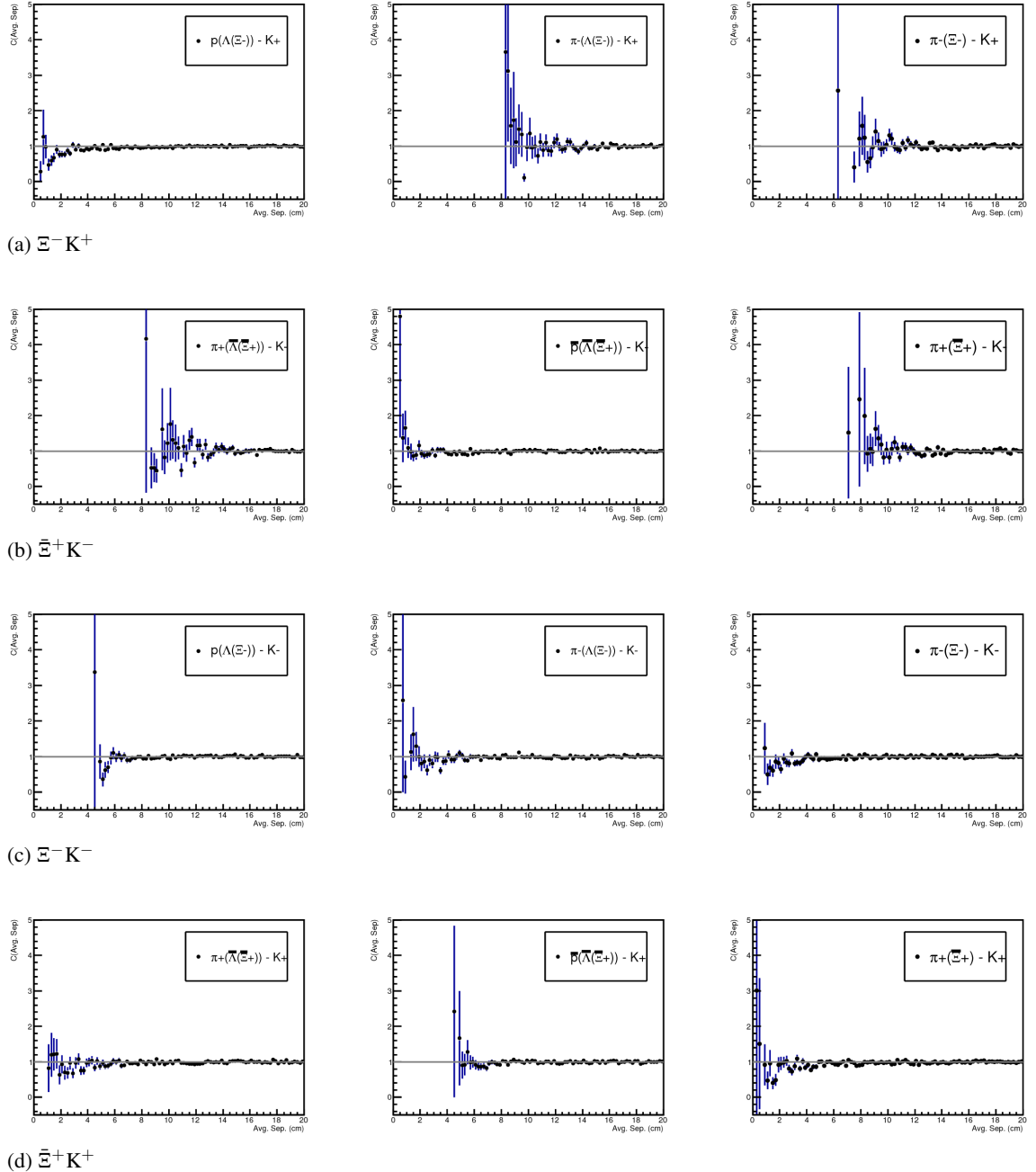
- 324           – Average Separation  $> 8.0$  cm for any daughter of  $\Xi$  sharing charge sign of  $K^\pm$   
 325            – ex. in  $\Xi^- K^-$  analysis,  $\pi^-$  daughter of  $\Lambda$  daughter with  $K^-$ , and bachelor  $\pi^-$  daugh-  
 326            ter with  $K^-$   
 327            – No cut for unlike signs



**Fig. 9:** Average separation (cm) correlation functions of  $\Lambda(\bar{\Lambda})$  and  $K_S^0$  Daughters. Only like-sign daughter pairs are shown (the distributions for unlike-signs were found to be flat). The title of each subfigure shows the daughter pair, as well as the mother of each daughter (in “()”), ex. top left is  $p$  from  $\Lambda$  with  $\pi^+$  from  $K_S^0$ .



**Fig. 10:** Average separation (cm) correlation functions of  $\Lambda(\bar{\Lambda})$  Daughter and  $K^\pm$ . Only like-sign pairs are shown (unlike-signs were flat). In the subfigure titles, the particles in “()” represent the mothers, ex. top left is  $p$  from  $\Lambda$  with  $K^+$ .



**Fig. 11:** Average separation (cm) correlation functions of  $\Xi$  Daughter and  $K^\pm$ . In the subfigure titles, the particles in “()” represent the mothers, ex. top left is  $p$  from  $\Lambda$  from  $\Xi^-$  with  $K^+$ .

---

328 **4 Correlation Functions**

329 This analysis studies the momentum correlations of both  $\Lambda$ -K and  $\Xi$ -K pairs using the two-particle correlation  
 330 function, defined as  $C(k^*) = A(k^*)/B(k^*)$ , where  $A(k^*)$  is the signal distribution,  $B(k^*)$  is the  
 331 reference (or background) distribution, and  $k^*$  is the momentum of one of the particles in the pair rest  
 332 frame. In practice,  $A(k^*)$  is constructed by binning in  $k^*$  pairs from the same event. Ideally,  $B(k^*)$  is sim-  
 333 ilar to  $A(k^*)$  in all respects excluding the presence of femtoscopic correlations [2]; as such,  $B(k^*)$  is used  
 334 to divide out the phase-space effects, leaving only the femtoscopic effects in the correlation function.

335 This analysis presents correlation functions for three centrality bins (0-10%, 10-30%, and 30-50%),  
 336 and is currently pair transverse momentum ( $k_T = 0.5|\mathbf{p}_{T,1} + \mathbf{p}_{T,2}|$ ) integrated (i.e. not binned in  $k_T$ ).  
 337 The correlation functions are constructed separately for the two magnetic field configurations, and are  
 338 combined using a weighted average:

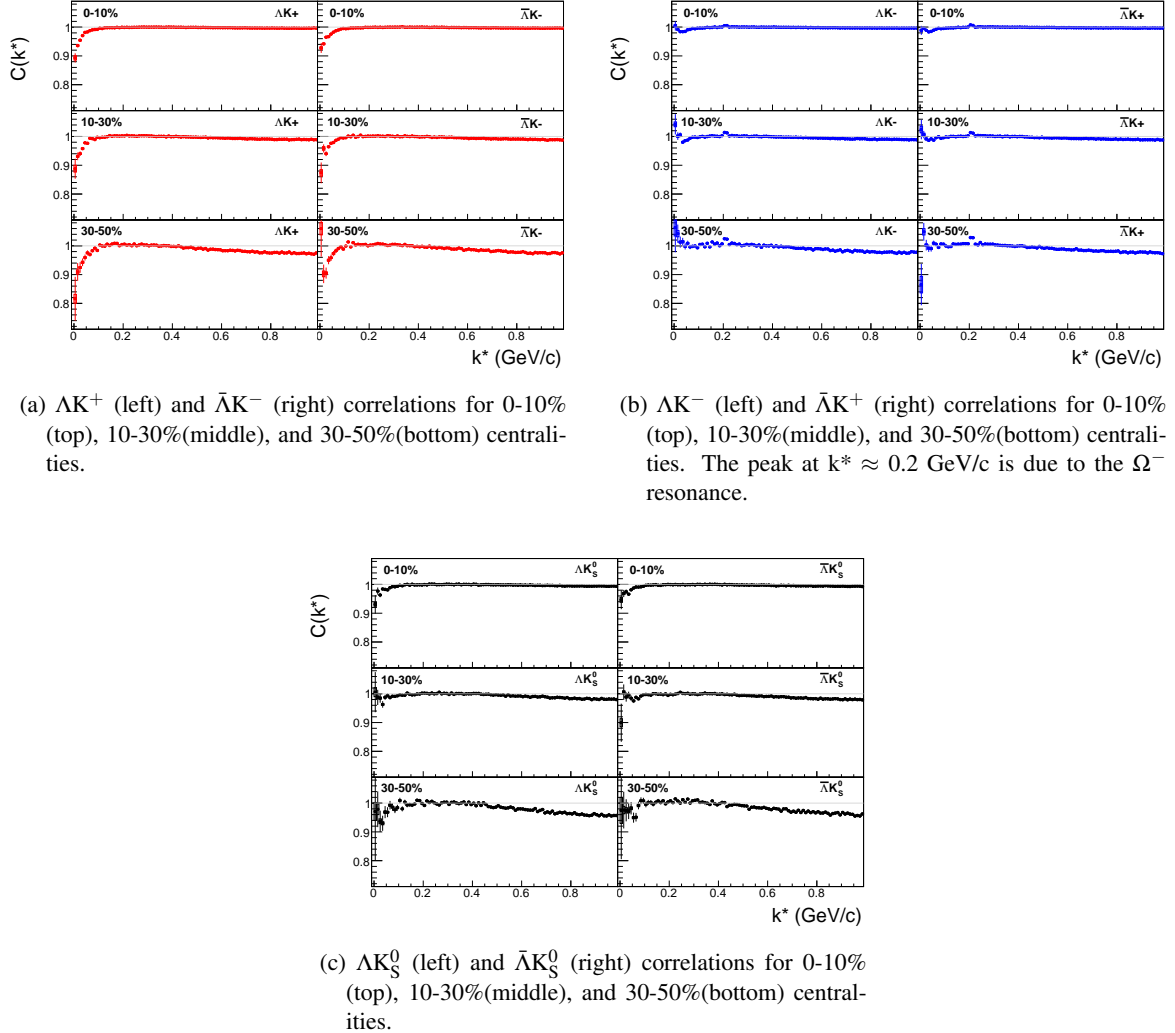
$$C_{combined}(k^*) = \frac{\sum_i w_i C_i(k^*)}{\sum_i w_i} \quad (3)$$

339 where the sum runs over the correlation functions to be combined, and the weight,  $w_i$ , is the number of  
 340 numerator pairs in  $C_i(k^*)$ . Here, the sum is over the two field configurations.

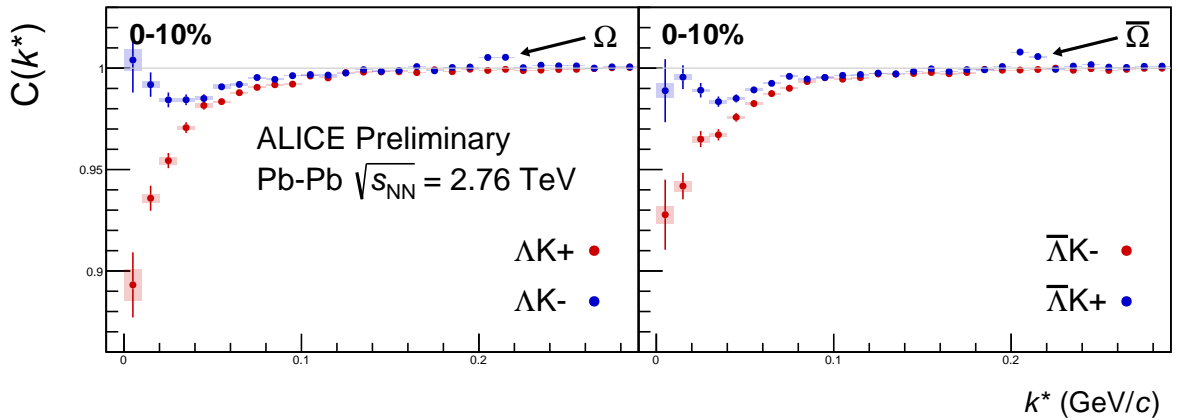
341 **4.1 Typical Correlation Function Construction**

342 Typically, in practice,  $B(k^*)$  is obtained by forming mixed-event pairs, i.e. particles from a given event  
 343 are paired with particles from  $N_{mix}(= 5)$  other events, and these pairs are then binned in  $k^*$ . In forming the  
 344 background distribution, it is important to mix only similar events; mixing events with different phase-  
 345 spaces can lead to artificial signals in the correlation function. Therefore, in this analysis, we mix events  
 346 with primary vertices within 2 cm and centralities within 5% of each other. Also note, a vertex correction  
 347 is also applied to each event, which essentially re-centers the primary vertices to  $z = 0$ .

348 Figures 12a, 12b, 12c show the correlation functions for all centralities studied for  $\Lambda K^+(\bar{\Lambda} K^-)$ ,  $\Lambda K^-(\bar{\Lambda} K^+)$ ,  
 349 and  $\Lambda(\bar{\Lambda}) K_S^0$ , respectively. All were normalized in the range  $0.32 < k^* < 0.4$  GeV/c.



**Fig. 12:**  $\Lambda K$  and  $\bar{\Lambda} K$  correlation functions for 0-10%, 10-30%, and 30-50% centralities. The lines represent the statistical errors, while the boxes represent the systematic errors.



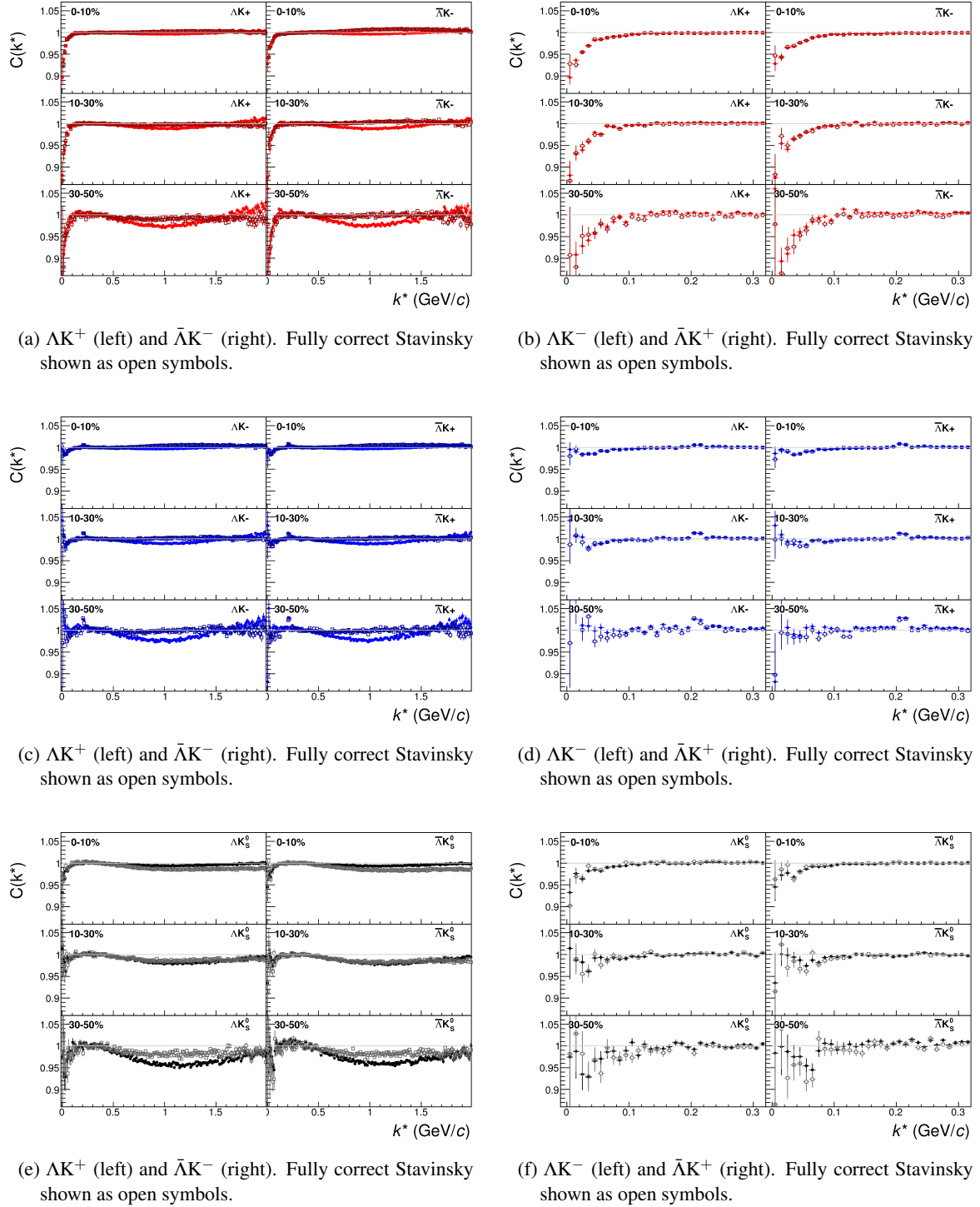
**Fig. 13:** Correlation Functions:  $\Lambda K^+$  vs  $\Lambda K^-$  ( $\bar{\Lambda} K^+$  vs  $\bar{\Lambda} K^-$ ) for 0-10% centrality. The peak in  $\Lambda K^-$  ( $\bar{\Lambda} K^+$ ) at  $k^* \approx 0.2$  GeV/c is due to the  $\Omega^-$  resonance. The lines represent the statistical errors. (NOTE: This figure is slightly dated, and a new one will be generated which includes both statistical and systematic uncertainties)

**350 4.2 Stavinsky Correlation Function Construction**

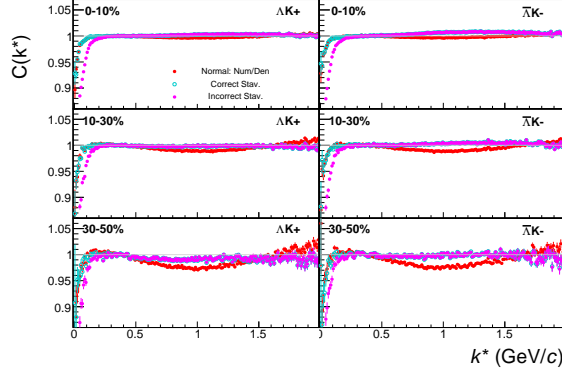
351 The purpose of the Stavinsky method is to rid the correlation functions of the non-femtoscopic back-  
352 ground. More specifically, this method is intended to handle background contributions from elliptic  
353 flow, and other sources having reflection symmetry in the transverse plane. With the Stavinsky method,  
354 mixed-event pairs are not used for the background; instead, same-event suds-pairs, formed by rotating  
355 one particle in a real pair by  $180^\circ$  in the transverse plane, as used as a background. This rotation rids  
356 the pairs of any femtoscopic correlation, while maintaining correlations due to elliptic flow (and other  
357 properly symmetric contributors).

358 The results of correctly implementing such a procedure are shown in Figure 14. The figure shows the  
359 Stavinsky method does a very good job of ridding the  $\Lambda K^\pm$  correlations of their non-femtoscopic back-  
360 grounds. We also see the procedure does not work as well on the  $\Lambda K_S^0$  system.

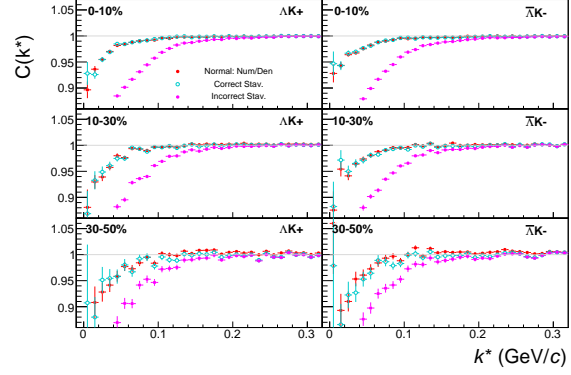
361 Now, one must be somewhat careful when applying this Stavinsky method. We found that, in order to  
362 obtain correct results, we had to run our pseudo-pairs through the same pair cuts used in our analyses. In  
363 an ideal world, our pair cut would only remove truly bad pairs results from splitting, merging, etc. In the  
364 real world, the pair cut always throws out some of the good with the bad. For the pseudo-pairs to form a  
365 reliable background, they too must experience the pair cut, and the loss of "good" pairs. We found this  
366 issue affected mainly our  $\Lambda K^+$  &  $\bar{\Lambda} K^-$  analysis, as can be seen in Figure 15, which shows both a correct  
367 implementation of the Stavinsky method, and an incorrect implementation lacking the additional pair cut  
368 on the pseudo-pairs.



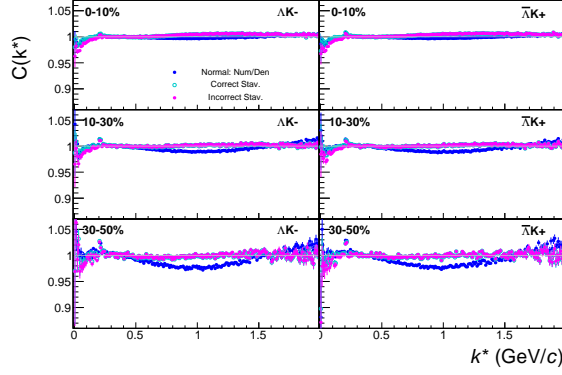
**Fig. 14:**  $\Lambda K$  and  $\bar{\Lambda} K$  correlation functions built using the fully correct Stavinsky method for 0-10%, 10-30%, and 30-50% centralities. In the full correct method, the pseudo-pairs (same-event pairs with one particle rotated by  $180^\circ$  in the transverse plane) are also run through the pair cuts used in the analysis. Closed symbols represent correlations built using the normal mixed-event background, while open symbols represent correlations formed using the Stavinsky same-event pseudo-pairs as a background. Figures in the right column are zoomed-in versions of figures in the left column.



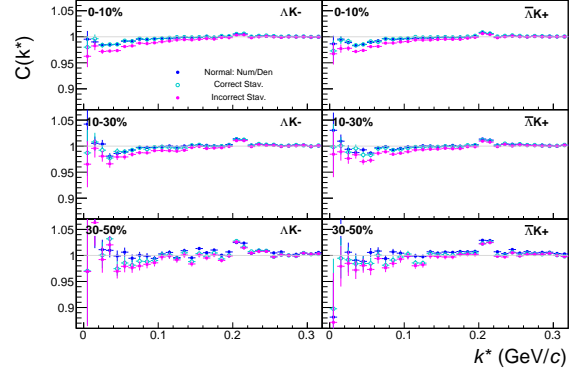
(a)  $\Lambda K^+$  (left) and  $\bar{\Lambda} K^-$  (right). Incorrect Stavinsky shown as open symbols.



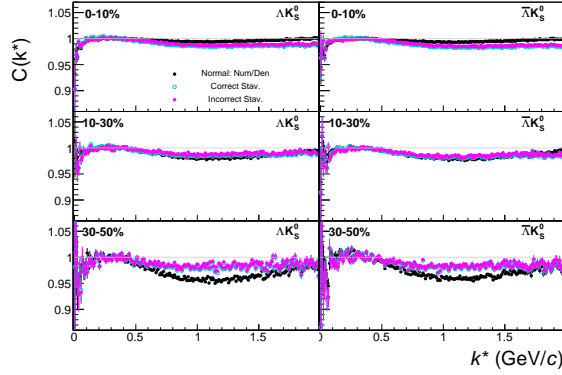
(b)  $\Lambda K^-$  (left) and  $\bar{\Lambda} K^+$  (right). Incorrect Stavinsky shown as open symbols.



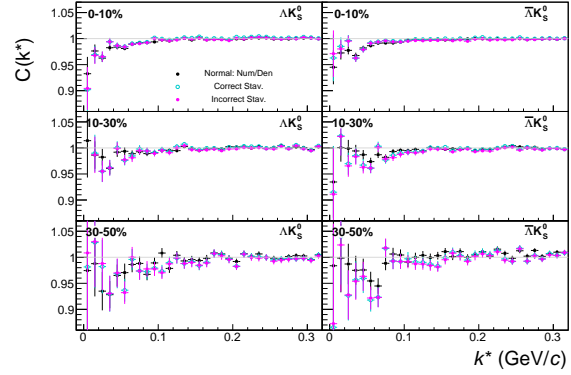
(c)  $\Lambda K^+$  (left) and  $\bar{\Lambda} K^-$  (right). Incorrect Stavinsky shown as open symbols.



(d)  $\Lambda K^-$  (left) and  $\bar{\Lambda} K^+$  (right). Incorrect Stavinsky shown as open symbols.



(e)  $\Lambda K^+$  (left) and  $\bar{\Lambda} K^-$  (right). Incorrect Stavinsky shown as open symbols.



(f)  $\Lambda K^-$  (left) and  $\bar{\Lambda} K^+$  (right). Incorrect Stavinsky shown as open symbols.

**Fig. 15:**  $\Lambda K$  and  $\bar{\Lambda} \bar{K}$  correlation functions built using the Stavinsky method for 0-10%, 10-30%, and 30-50% centralities. The closed, (red, blue, black) symbols represent correlation functions formed using the normal method with mixed-event background pairs. The open, cyan symbols represent correlation functions formed using the correct Stavinsky method. The closed, magenta symbols represent correlation functions formed using the incorrect Stavinsky method. In the incorrect method, the pseudo-pairs (same-event pairs with one particle rotated by  $180^\circ$  in the transverse plane) are not run through the pair cuts used in the analysis. Figures in the right column are zoomed-in versions of figures in the left column.

369 **5 Fitting**

370 **5.1 Model:**  $\Lambda K_S^0$ ,  $\Lambda K^\pm$ ,  $\Xi^{ch} K_S^0$

371 The two-particle relative momentum correlation function may be written theoretically by the Koonin-  
 372 Pratt equation [3, 4]:

$$C(\mathbf{k}^*) = \int S(\mathbf{r}^*) |\Psi_{\mathbf{k}^*}(\mathbf{r}^*)|^2 d^3 \mathbf{r}^* \quad (4)$$

373 In the absence of Coulomb effects, and assuming a spherically gaussian source of width  $R$ , the 1D  
 374 femtoscopic correlation function can be calculated analytically using:

$$C(k^*) = 1 + C_{QI}(k^*) + C_{FSI}(k^*) \quad (5)$$

375  $C_{QI}$  describes plane-wave quantum interference:

$$C_{QI}(k^*) = \alpha \exp(-4k^{*2}R^2) \quad (6)$$

376 where  $\alpha = (-1)^{2j}/(2j+1)$  for identical particles with spin  $j$ , and  $\alpha = 0$  for non-identical particles.  
 377 Obviously,  $\alpha = 0$  for all analyses presented in this note.  $C_{FSI}$  describes the s-wave strong final state  
 378 interaction between the particles:

$$\begin{aligned} C_{FSI}(k^*) &= (1 + \alpha) \left[ \frac{1}{2} \left| \frac{f(k^*)}{R} \right|^2 \left( 1 - \frac{d_0}{2\sqrt{\pi}R} \right) + \frac{2\Re f(k^*)}{\sqrt{\pi}R} F_1(2k^*R) - \frac{\Im f(k^*)}{R} F_2(2k^*R) \right] \\ f(k^*) &= \left( \frac{1}{f_0} + \frac{1}{2} d_0 k^{*2} - ik^* \right)^{-1}; \quad F_1(z) = \int_0^z \frac{e^{x^2-z^2}}{x} dx; \quad F_2(z) = \frac{1-e^{-z^2}}{z} \end{aligned} \quad (7)$$

379 where  $R$  is the source size,  $f(k^*)$  is the s-wave scattering amplitude,  $f_0$  is the complex scattering length,  
 380 and  $d_0$  is the effective range of the interaction.

381 An additional parameter  $\lambda$  is typically included in the femtoscopic fit function to account for the purity  
 382 of the pair sample. In the case of no residual correlations (to be discussed in Section 5.4), the fit function  
 383 becomes:

$$C(k^*) = 1 + \lambda [C_{QI}(k^*) + C_{FSI}(k^*)] \quad (8)$$

384 **5.2 Model:**  $\Xi^{ch} K^{ch}$

385 The two-particle correlation function may be written as:

$$C(\mathbf{k}^*) = \sum_S \rho_S \int S(\mathbf{r}^*) |\Psi_{\mathbf{k}^*}^S(\mathbf{r}^*)|^2 d^3 \mathbf{r}^* \quad (9)$$

386 where  $\rho_S$  is the normalized emission probability of particles in a state with spin  $S$ ,  $S(\mathbf{r}^*)$  is the pair  
 387 emission source distribution (assumed to be Gaussian), and  $\Psi_{\mathbf{k}^*}^S(\mathbf{r}^*)$  is the two-particle wave-function  
 388 including both strong and Coulomb interactions [5]:

$$\Psi_{\mathbf{k}^*}(\mathbf{r}^*) = e^{i\delta_c} \sqrt{A_c(\eta)} [e^{i\mathbf{k}^* \cdot \mathbf{r}^*} F(-i\eta, 1, i\xi) + f_c(k^*) \frac{\tilde{G}(\rho, \eta)}{r^*}] \quad (10)$$

where  $\rho = k^*r^*$ ,  $\eta = (k^*a_c)^{-1}$ ,  $\xi = \mathbf{k}^* \cdot \mathbf{r}^* + k^*r^* \equiv \rho(1 + \cos\theta^*)$ , and  $a_c = (\mu z_1 z_2 e^2)^{-1}$  is the two-particle Bohr radius (including the sign of the interaction).  $\delta_c$  is the Coulomb s-wave phase shift,  $A_c(\eta)$  is the Coulomb penetration factor,  $\tilde{G} = \sqrt{A_c}(G_0 + iF_0)$  is a combination of the regular ( $F_0$ ) and singular ( $G_0$ ) s-wave Coulomb functions.  $f_c(k^*)$  is the s-wave scattering amplitude:

$$f_c(k^*) = \left[ \frac{1}{f_0} + \frac{1}{2}d_0k^{*2} - \frac{2}{a_c}h(\eta) - ik^*A_c(\eta) \right]^{-1} \quad (11)$$

where, the “h-function”,  $h(\eta)$ , is expressed through the digamma function,  $\psi(z) = \Gamma'(z)/\Gamma(z)$  as:

$$h(\eta) = 0.5[\psi(i\eta) + \psi(-i\eta) - \ln(\eta^2)] \quad (12)$$

In this case, the  $\lambda$  parameter may be included as:

$$C(\mathbf{k}^*) = (1 - \lambda) + \lambda \sum_S \rho_S \int S(\mathbf{r}^*) |\Psi_{\mathbf{k}^*}^S(\mathbf{r}^*)|^2 d^3\mathbf{r}^* \quad (13)$$

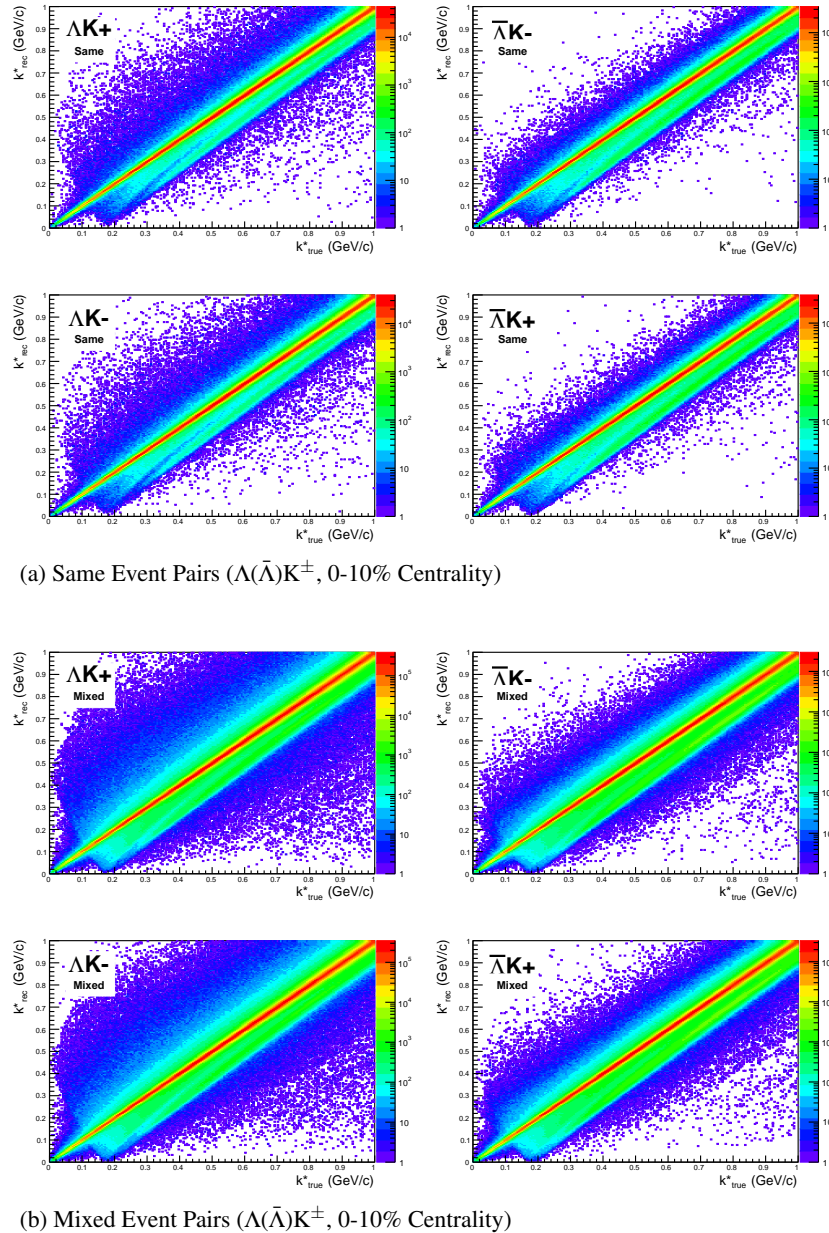
### 5.3 Momentum Resolution Corrections

Finite track momentum resolution causes the reconstructed momentum of a particle to smear around the true value. This, of course, also holds true for V0 particles. The effect is propagated up to the pairs of interest, which causes the reconstructed relative momentum ( $k_{Rec}^*$ ) to differ from the true momentum ( $k_{True}^*$ ). Smearing of the momentum typically will result in a suppression of the signal.

The effect of finite momentum resolution can be investigated using the MC data, for which both the true and reconstructed momenta are available. Figure 16 shows sample  $k_{True}^*$  vs.  $k_{Rec}^*$  plots for  $\Lambda(\bar{\Lambda})K^\pm$  0-10% analyses; Figure 16a was generated using same-event pairs, while Figure 16b was generated using mixed-event pairs (with  $N_{mix} = 5$ ).

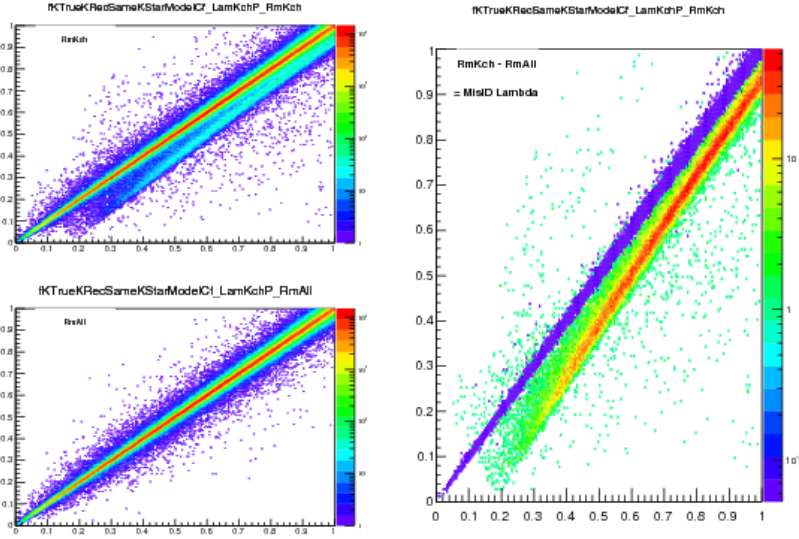
If there are no contaminations in our particle collection, the plots in Figure 16 should be smeared around  $k_{True}^* = k_{Rec}^*$ ; this is mostly true in our analyses. However, there are some interesting features of our results which demonstrate a small (notice the log-scale on the z-axis) contamination in our particle collection. The structure around  $k_{Rec}^* = k_{True}^* - 0.15$  is mainly caused by  $K_S^0$  contamination in our  $\Lambda(\bar{\Lambda})$  sample. The remaining structure not distributed about  $k_{Rec}^* = k_{True}^*$  is due to  $\pi$  and  $e$  contamination in our  $K^\pm$  sample. These contaminations are more visible in Figure 17, which show  $k_{Rec}^*$  vs.  $k_{True}^*$  plots (for a small sample of the  $\Lambda K^\pm$  0-10% central analysis), for which the MC truth (i.e. true, known identity of the particle) was used to eliminate misidentified particles in the  $K^+(a)$  and  $\Lambda(b)$  collections. (NOTE: This is an old figure and is for a small sample of the data. A new version will be generated shortly. It, nonetheless, demonstrates the point well).

Information gained from looking at  $k_{Rec}^*$  vs  $k_{True}^*$  can be used to apply corrections to account for the effects of finite momentum resolution on the correlation functions. A typical method (“Ratio” method) involves using the MC HIJING data to build two correlation functions,  $C_{Rec}(k^*)$  and  $C_{True}(k^*)$ , using the generator-level momentum ( $k_{True}^*$ ) and the measured detector-level momentum ( $k_{Rec}^*$ ). The data is then corrected by multiplying by the ratio,  $C_{True}/C_{Rec}$ , before fitting. This essentially unsmears the data, which that can be compared directly to theoretical predictions and fits. Although this is conceptually simple, there are a couple of big disadvantages to this method. First, HIJING does not incorporate final-state interactions, so weights must be used when building same-event (numerator) distributions. These weights account for the interactions, and, in the absence of Coulomb interactions, can be calculated using Eq. 5. Of course, these weights are valid only for a particular set of fit parameters. Therefore, in the fitting process, during which the fitter explores a large parameter set, the corrections will not remain valid. As such, applying the momentum resolution correction and fitting becomes a long and drawn out iterative

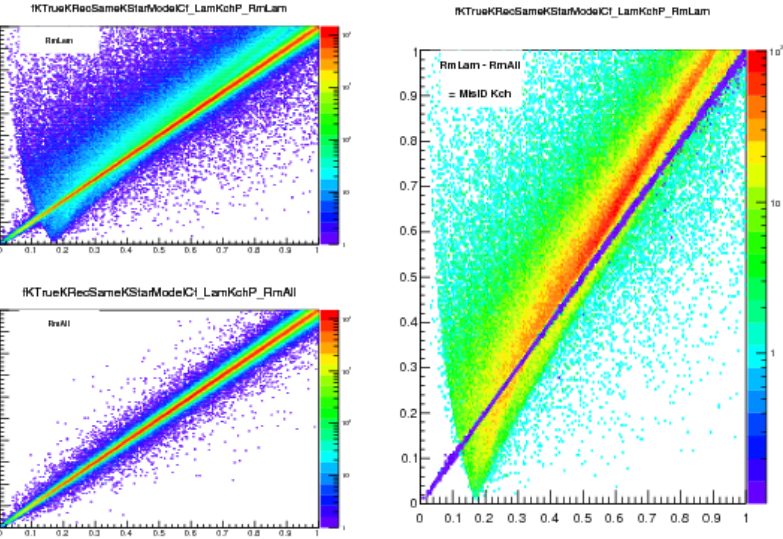


**Fig. 16:** Sample  $k_{True}^*$  vs.  $k_{Rec}^*$  plot for  $\Lambda(\bar{\Lambda})K^\pm$  0-10% analyses. The structure which appears around  $k_{Rec}^* = k_{True}^* - 0.15$  is mainly caused by  $K_S^0$  contamination in our  $\Lambda(\bar{\Lambda})$  sample. The remaining structure not distributed about  $k_{Rec}^* = k_{True}^*$  is due to  $\pi$  and  $e$  contamination in our  $K^\pm$  sample. These contaminations are more clearly visible in Figure 17

process. An initial parameter set is obtained (through fitting without momentum resolution corrections, theoretical models, or a good guess), then the MC data is run over to obtain the correction factor, the data is fit using the correction factor, a refined parameter set is extracted, the MC data is run over again to obtain the new correction factor, etc. This process continues until the parameter set stabilizes. The second issue concerns statistics. With the MC data available on the grid, we were not able to generate the statistics necessary to use the raw  $C_{True}/C_{Rec}$  ratio. The ratio was not stable, and when applied to the data, obscured the signal. Attempting to fit the ratio to generate the corrections also proved problematic. However, as HIJING does not include final-state interactions, the same-event and mixed-event pairs are very similar (with the exception of things like energy and momentum conservation, etc). Therefore, one may build the numerator distribution using mixed-event pairs. This corresponds, more or



(a) (Top Left) All misidentified  $K^+$  excluded. (Bottom Left) All misidentified  $\Lambda$  and  $K^+$  excluded. (Right) The difference of (Top Left) - (Bottom Left), which reveals the contamination in our  $\Lambda$  collection. The structure which appears around  $k_{Rec}^* = k_{True}^* - 0.15$  is mainly caused by  $K_S^0$  contamination in our  $\Lambda(\bar{\Lambda})$  sample.



(b) (Top Left) All misidentified  $\Lambda$  excluded. (Bottom Left) All misidentified  $\Lambda$  and  $K^-$  excluded. (Right) The difference of (Top Left) - (Bottom Left), which reveals the contamination in our  $K^-$  collection. The structure not distributed about  $k_{Rec}^* = k_{True}^*$  is due to  $\pi$  and  $e^-$  contamination in our  $K^\pm$  sample.

**Fig. 17:** Note: This is an old figure and is for a small sample of the data. A new version will be generated shortly.  
y-axis =  $k_{Rec}^*$ , x-axis =  $k_{True}^*$ .

(Left)  $k_{Rec}^*$  vs.  $k_{True}^*$  plots for a small sample of the  $\Lambda K^+$  0-10% central analysis, MC truth was used to eliminate misidentified particles in the  $K^+$ (a) and  $\Lambda$ (b) collections. (Right) The difference of the top left and bottom left plots. Contaminations in our particle collections are clearly visible. Figure (a) demonstrates a  $K_S^0$  contamination in our  $\Lambda$  collection; Figure (b) demonstrates a  $\pi$  and  $e^-$  contamination in our  $K^\pm$  collection.

436 less, to simply running a the weight generator through the detector framework.

437 A second approach ("Matrix" method) is to use information gained from plots like those in Figure 16,  
438 which can be considered response matrices. The reponse matrix describes quantitatively how each  $k_{Rec}^*$

439 bin receives contributions from multiple  $k_{True}^*$  bins, and can be used to account for the effects of finite mo-  
 440 mentum resolution. With this approach, the resolution correction is applied on-the-fly during the fitting  
 441 process by propagating the theoretical (fit) correlation function through the response matrix, according  
 442 to:

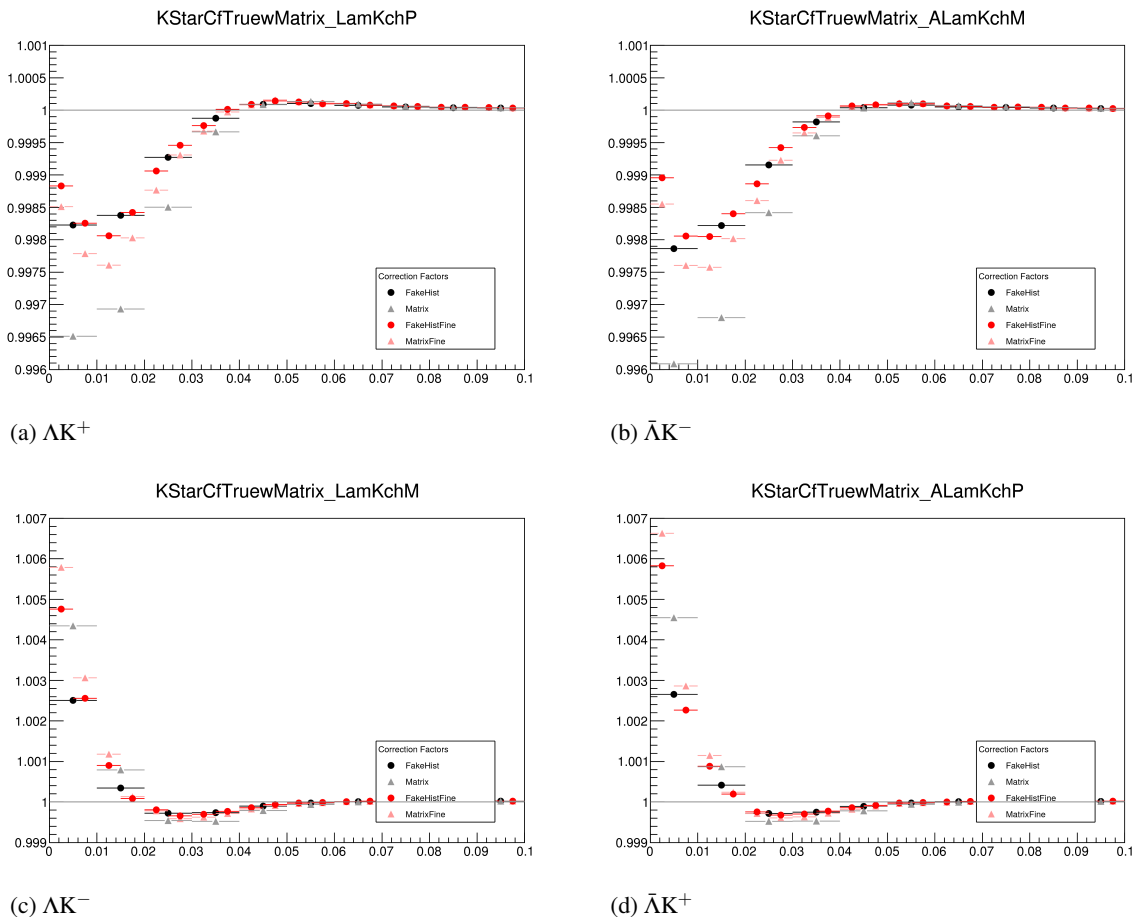
$$C_{fit}(k_{Rec}^*) = \frac{\sum_{k_{True}^*} M_{k_{Rec}^*, k_{True}^*} C_{fit}(k_{True}^*)}{\sum_{k_{True}^*} M_{k_{Rec}^*, k_{True}^*}} \quad (14)$$

443 where  $M_{k_{Rec}^*, k_{True}^*}$  is the response matrix (Figure 16),  $C_{fit}(k_{True}^*)$  is the fit binned in  $k_{True}^*$ , and the denomi-  
 444 nator normalizes the result.

445 Equation 14 describes that, for a given  $k_{Rec}^*$  bin, the observed value of  $C(k_{Rec}^*)$  is a weighted average of  
 446 all  $C(k_{True}^*)$  values, where the weights are the normalized number of counts in the  $[k_{Rec}^*, k_{True}^*]$  bin. As  
 447 seen in Figure 16, overwhelmingly the main contributions comes from the  $k_{Rec}^* = k_{True}^*$  bins. Although  
 448 the correction is small, it is non-negligible for the low- $k^*$  region of the correlation function.

449 Here, the momentum resolution correction is applied to the fit, not the data. In other words, during  
 450 fitting, the theoretical correlation function is smeared just as real data would be, instead of unsmearing  
 451 the data. This may not be ideal for the theorist attempting to compare a model to experimental data, but  
 452 it leaves the experimental data unadulterated. The current analyses use this second approach to applying  
 453 momentum resolution corrections because of two major advantages. First, the MC data must be analyzed  
 454 only once, and no assumptions about the fit are needed. Secondly, the momentum resolution correction  
 455 is applied on-the-fly by the fitter, delegating the iterative process to a computer instead of the user.

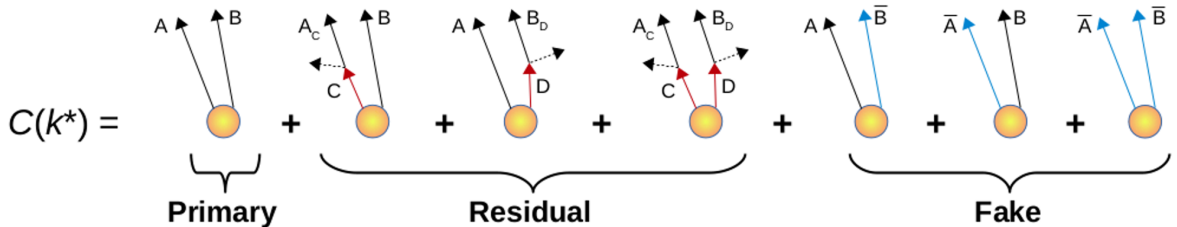
456 The two methods described above, Ratio and Matrix, should reproduce the same results at the parameter  
 457 set used to generate the  $C_{True}/C_{Rec}$  needed for the Ratio method. Figure 18 shows that the two methods  
 458 converge as the binning size is decreased.



**Fig. 18:** Comparison of the two methods, Ratio and Matrix, for accounting for momentum resolution effects with HIJING. The Ratio method corresponds to the "FakeHist" histograms (circles), while the Matrix method corresponds to the "Matrix" histograms (triangles). Black shows a course binning, while red shows a finer binning.

459 **5.4 Residual Correlations**

460 The purpose of this analysis is study the interaction and scale of the emitting source of the pairs. In  
 461 order to obtain correct results, it is important for our particle collections to consist of primary particles.  
 462 In practice, this is difficult to achieve for our  $\Lambda$  and  $\bar{\Lambda}$  collections. Many of our  $\Lambda$  particles are not  
 463 primary, but originate as decay products from other hyperons, including  $\Sigma^0$ ,  $\Xi^0$ ,  $\Xi^-$  and  $\Sigma^{*(+,-,0)}(1385)$ .  
 464 Additionally, many of our K particles are not primary, but decay from  $K^{*(+,-,0)}(892)$  parents. In these  
 465 decays, the  $\Lambda$  carries away a momentum very similar to that of its parent. As a result, the correlation  
 466 function between a secondary  $\Lambda$  and, for instance, a  $K^+$  will be sensitive to, and dependent upon, the  
 467 interaction between the parent of the  $\Lambda$  and the  $K^+$ . In effect, the correlation between the parent of  
 468 the  $\Lambda$  and the  $K^+$  (ex.  $\Sigma^0 K^+$ ) will be visible, although smeared out, in the  $\Lambda K^+$  data; we call this a  
 469 residual correlation resulting from feed-down. The contributions from the primary correlation, residual  
 470 correlations, and fake pairs on the finally measure data is shown schematically in Figure 19. Residual  
 471 correlations are important in an analysis when three criteria are met [6]: i) the parent correlation signal  
 472 is large, ii) a large fraction of pairs in the sample originate from the particular parent system, and iii) the  
 473 decay momenta are comparable to the expected correlation width in  $k^*$ .



**Fig. 19:** A schematic representation of the contributions to the finally measured data from the primary correlation, residual correlations, and fake pairs.

474 As it is difficult for us to eliminate these residual correlations in our analyses, we must attempt to account  
 475 for them in our fitter. To achieve this, we will simultaneously fit the data for both the primary correlation  
 476 function and the residual correlations. For example, in the simple case of a  $\Lambda K^+$  analysis with residuals  
 477 arising solely from  $\Sigma^0 K^+$  feed-down:

$$C_{measured}(k_{\Lambda K^+}^*) = 1 + \lambda_{\Lambda K^+}[C_{\Lambda K^+}(k_{\Lambda K^+}^*) - 1] + \lambda_{\Sigma^0 K^+}[C_{\Sigma^0 K^+}(k_{\Lambda K^+}^*) - 1]$$

$$C_{\Sigma^0 K^+}(k_{\Lambda K^+}^*) \equiv \frac{\sum_{k_{\Sigma^0 K^+}^*} C_{\Sigma^0 K^+}(k_{\Sigma^0 K^+}^*) T(k_{\Sigma^0 K^+}^*, k_{\Lambda K^+}^*)}{\sum_{k_{\Sigma^0 K^+}^*} T(k_{\Sigma^0 K^+}^*, k_{\Lambda K^+}^*)} \quad (15)$$

478  $C_{\Sigma^0 K^+}(k_{\Sigma^0 K^+}^*)$  is the  $\Sigma^0 K^+$  correlation function from, for instance, Equation 5, and  $T$  is the transform  
 479 matrix generated with THERMINATOR. The transform matrix is formed for a given parent pair, AB,  
 480 by taking all  $\Lambda K$  pairs originating from AB, calculating the relative momentum of the parents ( $k_{AB}^*$ )  
 481 and daughters ( $k_{\Lambda K}^*$ ), and filling a two-dimensional histogram with the values. The transform matrix  
 482 is essentially an unnormalized probability distribution mapping the  $k^*$  of the parent pair to that of the  
 483 daughter pair when one or both parents decay. An example of such transform matrices can be found in  
 484 Figures 20 and 21.

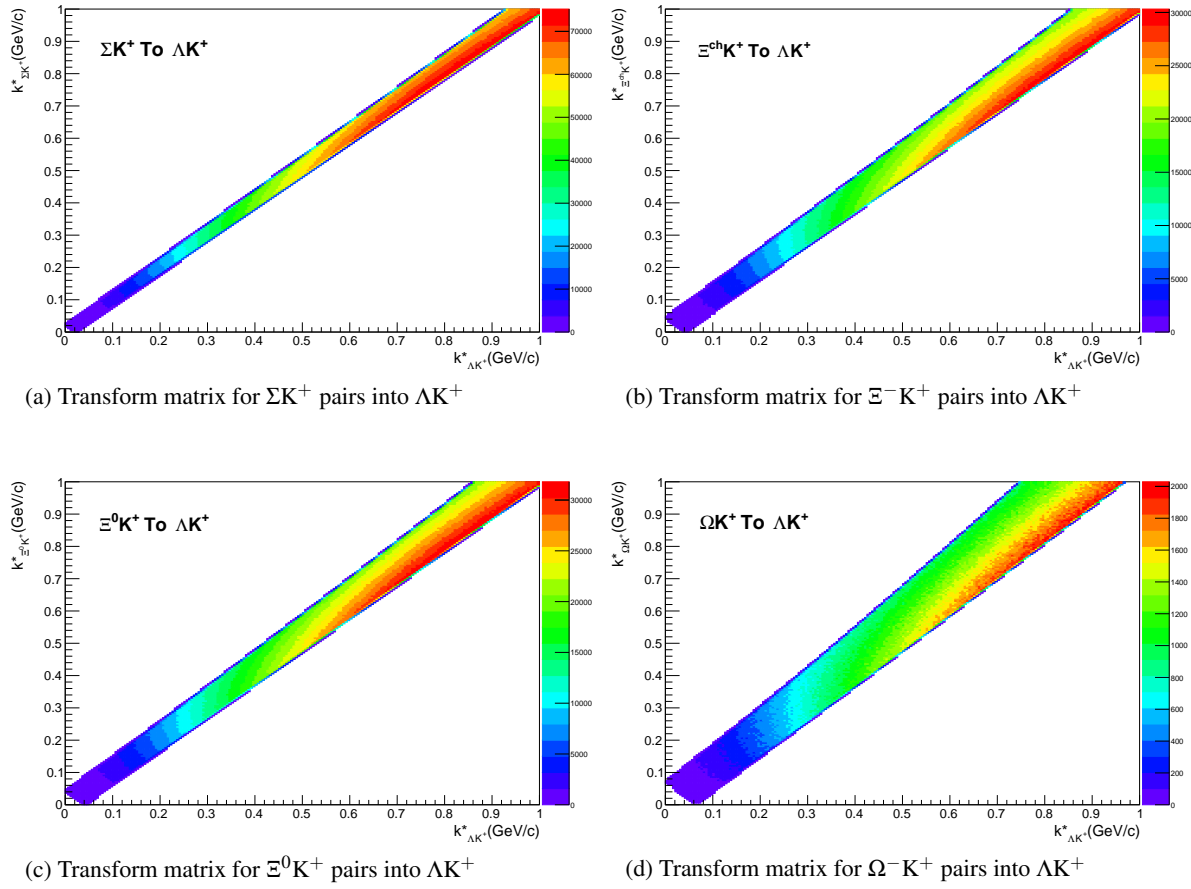
485 The above equation can be easily extended to include feed-down from more sources:

$$\begin{aligned}
C_{measured}(k_{\Lambda K}^*) &= 1 + \lambda_{\Lambda K}[C_{\Lambda K}(k_{\Lambda K}^*) - 1] + \lambda_{\Sigma^0 K}[C_{\Sigma^0 K}(k_{\Lambda K}^*) - 1] + \dots \\
&\quad + \lambda_{P_1 P_2}[C_{P_1 P_2}(k_{\Lambda K}^*) - 1] + \lambda_{other}[C_{other}(k_{\Lambda K}^*) - 1]
\end{aligned}
\tag{16}$$

$$C_{P_1 P_2}(k_{\Lambda K}^*) \equiv \frac{\sum_{k_{P_1 P_2}^*} C_{P_1 P_2}(k_{P_1 P_2}^*) T(k_{P_1 P_2}^*, k_{\Lambda K}^*)}{\sum_{k_{P_1 P_2}^*} T(k_{P_1 P_2}^*, k_{\Lambda K}^*)}$$

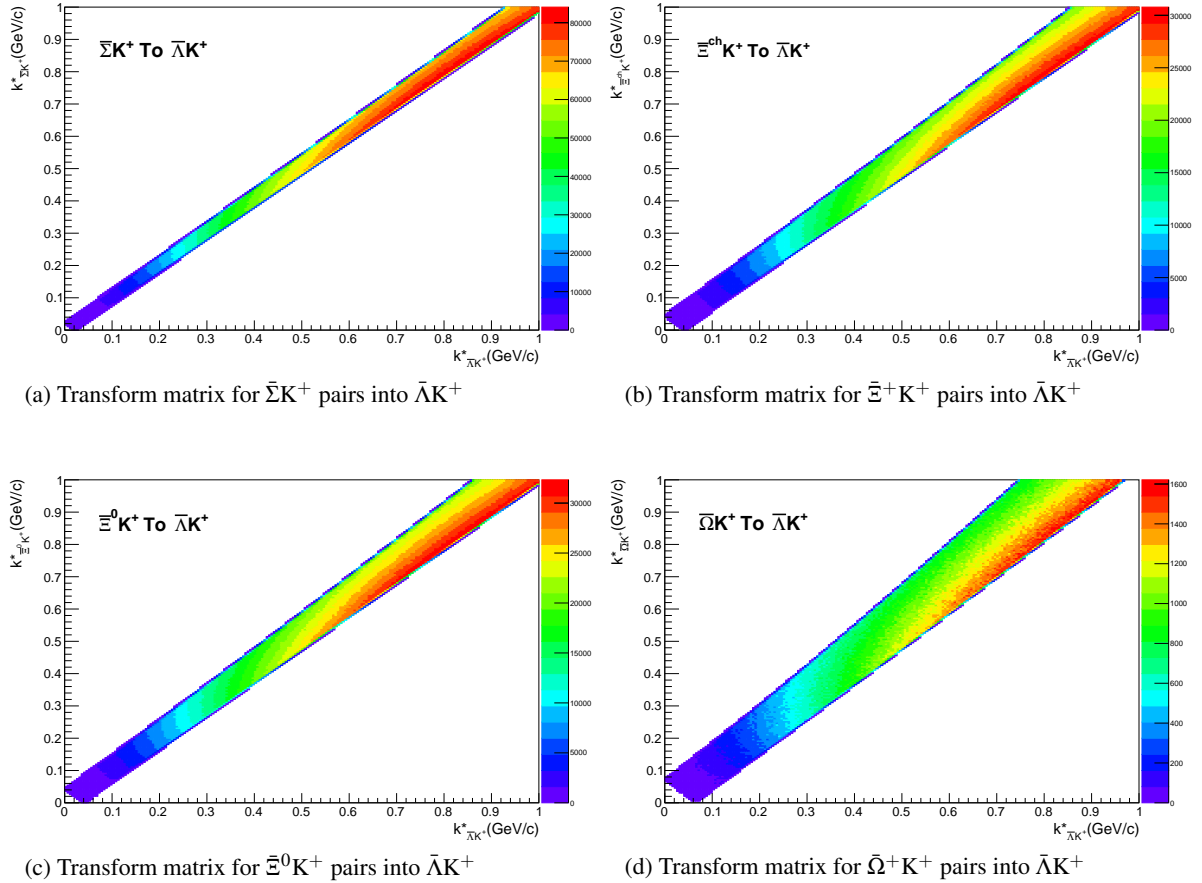
486 Or, more compactly:

$$C_{measured}(k_{\Lambda K}^*) = 1 + \sum_i \lambda_i [C_i(k_{\Lambda K}^*) - 1] \tag{17}$$



**Fig. 20:** Transform Matrices generated with THERMINATOR for  $\Lambda K^+$  Analysis

487 So, in practice, we model the correlation function of the parents, and run the correlation function through  
488 the appropriate transform matrix to determine the contribution to the daughter correlation function. A  
489 few questions still remain. First, what  $\lambda$  values should be used in the above equation? One option  
490 would be to leave all of these  $\lambda$ -parameters free during the fit process. However, this would introduce  
491 a huge number of new parameters into the fitter, and would make the fit results less trustworthy. The  $\lambda$   
492 parameters roughly dictate the strength of the parent contribution to the daughter pair. Additionally, as  
493 found in [7], the reconstruction efficiency for primary  $\Lambda$  particles is nearly equal to that of  $\Lambda$  particles  
494 originating from  $\Sigma$ ,  $\Sigma^*$ ,  $\Xi^0$ ,  $\Xi^-$ , and  $\Omega$  hyperons. Therefore, the  $\lambda$  parameter for parent system AB can



**Fig. 21:** Transform Matrices generated with THERMINATOR for  $\bar{\Lambda}K^+$  Analysis

495 be estimated using THERMINATOR as the total number of  $\Lambda K$  pairs originating from AB ( $N_{AB}$ ) divided  
 496 by the total number of  $\Lambda K$  pairs ( $N_{Total}$ ):

$$\lambda_{AB} = \frac{N_{AB}}{N_{Total}} \quad (18)$$

497 The  $\lambda$  values used can be found in Table 1, for the case of both three and ten residual contributors. In the  
 498 table, we also list the  $\lambda$  values used for “Other” and “Fakes”. The “Other” category contains pairs which  
 499 are not primary, and which do not originate from the (3 or 10) residual pairs included in the fit. The  
 500 “Fakes” category represents pairs that are mistakenly identified as  $\Lambda K$ . To estimate this  $\lambda_{Fakes}$  value, we  
 501 assumed that the number of fake pairs was equal to the total number of pairs multiplied by the  $\Lambda$  purity  
 502 (i.e. assuming perfect purity for the kaons); or, more simply,  $\lambda_{Fakes} = 1.0 - \text{Purity}(\Lambda)$ . For both of these  
 503 contributors (“Other” and “Fakes”), we assume that these correlations average to unity, and therefore do  
 504 not contribute to the final correlation function.

$\Lambda K^+$ residuals		$\bar{\Lambda}K^-$ residuals		$\Lambda K^-$ residuals		$\bar{\Lambda}K^+$ residuals		$\Lambda K_S^0$ residuals		$\bar{\Lambda}K_S^0$ residuals	
Pair System	$\lambda$ value	Pair System	$\lambda$ value	Pair System	$\lambda$ value	Pair System	$\lambda$ value	Pair System	$\lambda$ value	Pair System	$\lambda$ value
3 Residuals											
$\Lambda K^+$	0.154	$\bar{\Lambda}K^-$	0.158	$\Lambda K^-$	0.154	$\bar{\Lambda}K^+$	0.158	$\Lambda K_S^0$	0.165	$\bar{\Lambda}K_S^0$	0.169
$\Sigma^0 K^+$	0.099	$\bar{\Sigma}^0 K^-$	0.102	$\Sigma^0 K^-$	0.099	$\bar{\Sigma}^0 K^+$	0.103	$\Sigma^0 K_S^0$	0.107	$\bar{\Sigma}^0 K_S^0$	0.111
$\Xi^0 K^+$	0.072	$\bar{\Xi}^0 K^-$	0.067	$\Xi^0 K^-$	0.071	$\bar{\Xi}^0 K^+$	0.068	$\Xi^0 K_S^0$	0.077	$\bar{\Xi}^0 K_S^0$	0.073
$\Xi^- K^+$	0.069	$\bar{\Xi}^+ K^-$	0.065	$\Xi^- K^-$	0.068	$\bar{\Xi}^+ K^+$	0.066	$\Xi^- K_S^0$	0.075	$\bar{\Xi}^+ K_S^0$	0.071
Other	0.558	Other	0.560	Other	0.561	Other	0.557	Other	0.528	Other	0.528
Fakes	0.048	Fakes	0.048	Fakes	0.048	Fakes	0.048	Fakes	0.048	Fakes	0.048
10 Residuals											
$\Lambda K^+$	0.154	$\bar{\Lambda}K^-$	0.158	$\Lambda K^-$	0.154	$\bar{\Lambda}K^+$	0.158	$\Lambda K_S^0$	0.165	$\bar{\Lambda}K_S^0$	0.169
$\Sigma^0 K^+$	0.099	$\bar{\Sigma}^0 K^-$	0.102	$\Sigma^0 K^-$	0.099	$\bar{\Sigma}^0 K^+$	0.103	$\Sigma^0 K_S^0$	0.107	$\bar{\Sigma}^0 K_S^0$	0.111
$\Xi^0 K^+$	0.072	$\bar{\Xi}^0 K^-$	0.067	$\Xi^0 K^-$	0.071	$\bar{\Xi}^0 K^+$	0.068	$\Xi^0 K_S^0$	0.077	$\bar{\Xi}^0 K_S^0$	0.073
$\Xi^- K^+$	0.069	$\bar{\Xi}^+ K^-$	0.065	$\Xi^- K^-$	0.068	$\bar{\Xi}^+ K^+$	0.066	$\Xi^- K_S^0$	0.075	$\bar{\Xi}^+ K_S^0$	0.071
$\Sigma^{*+} K^+$	0.046	$\bar{\Sigma}^{*-} K^-$	0.046	$\Sigma^{*+} K^-$	0.046	$\bar{\Sigma}^{*-} K^+$	0.046	$\Sigma^{*+} K_S^0$	0.050	$\bar{\Sigma}^{*-} K_S^0$	0.050
$\Sigma^{*-} K^+$	0.042	$\bar{\Sigma}^{*+} K^-$	0.045	$\Sigma^{*-} K^-$	0.041	$\bar{\Sigma}^{*+} K^+$	0.045	$\Sigma^{*-} K_S^0$	0.045	$\bar{\Sigma}^{*+} K_S^0$	0.049
$\Sigma^{*0} K^+$	0.042	$\bar{\Sigma}^{*0} K^-$	0.040	$\Sigma^{*0} K^-$	0.041	$\bar{\Sigma}^{*0} K^+$	0.041	$\Sigma^{*0} K_S^0$	0.045	$\bar{\Sigma}^{*0} K_S^0$	0.044
$\Lambda K^{*0}$	0.039	$\bar{\Lambda}K^{*0}$	0.041	$\Lambda \bar{K}^{*0}$	0.039	$\bar{\Lambda}K^{*0}$	0.041	$\Lambda K^{*0}$	0.019	$\bar{\Lambda}K^{*0}$	0.020
$\Sigma^0 K^{*0}$	0.035	$\bar{\Sigma}^0 \bar{K}^{*0}$	0.036	$\Sigma^0 \bar{K}^{*0}$	0.035	$\bar{\Sigma}^0 K^{*0}$	0.036	$\Sigma^0 K^{*0}$	0.017	$\bar{\Sigma}^0 K^{*0}$	0.017
$\Xi^0 K^{*0}$	0.025	$\bar{\Xi}^0 \bar{K}^{*0}$	0.024	$\Xi^0 \bar{K}^{*0}$	0.025	$\bar{\Xi}^0 K^{*0}$	0.024	$\Xi^0 K^{*0}$	0.012	$\bar{\Xi}^0 K^{*0}$	0.011
$\Xi^- K^{*0}$	0.024	$\bar{\Xi}^+ \bar{K}^{*0}$	0.023	$\Xi^- \bar{K}^{*0}$	0.024	$\bar{\Xi}^+ K^{*0}$	0.023	$\Xi^- K^{*0}$	0.012	$\bar{\Xi}^+ K^{*0}$	0.011
Other	0.305	Other	0.305	Other	0.308	Other	0.301	Other	0.329	Other	0.326
Fakes	0.048	Fakes	0.048	Fakes	0.048	Fakes	0.048	Fakes	0.048	Fakes	0.048

**Table 1:**  $\lambda$  values for the individual components of the  $\Lambda K$  correlation functions for the case of 3 and 10 residual contributions.

Now, the remaining question is how do we model the parent correlation functions? In an ideal world, we would simply look up the parent interaction in some table, and input this into our Lednicky equation (for the case of one or more charge neutral particle in the pair), or run it through the CoulombFitter machinery described in Sec. 5.2. Unfortunately, the world in which we live is not perfect, such a table does not exist, and little is known about the interaction between the residual pairs in this study. One solution would be to introduce a set of scattering parameters and radii for each residual system. However, as will be the case of the  $\lambda$ -parameters above, this would introduce a large number of additional fit parameters, and would make our fitter too unconstrained and would yield untrustworthy results. The second option, which is adopted in this analysis, is to assume all residual pairs have the same source size as the daughter pair, and all Coulomb-neutral residual pairs also share the same scattering parameters as the daughter pair (the case of charged pairs will be described below).

Concerning the radii of the residual parent pairs, it was suggested that these should be set to smaller values. In the interest of minimizing the number of parameters in the fitter, we tested this by introducing an  $m_T$ -scaling of the parent radii. The motivation for this scaling comes from the approximate  $m_T$ -scaling of the radii observed in ???. To achieve this scaling, we assume the radii follow an inverse-square-root distribution:  $R_{AB} = \alpha m_T^{-1/2}$ . Then, it follows that we should scale the parent radii as:

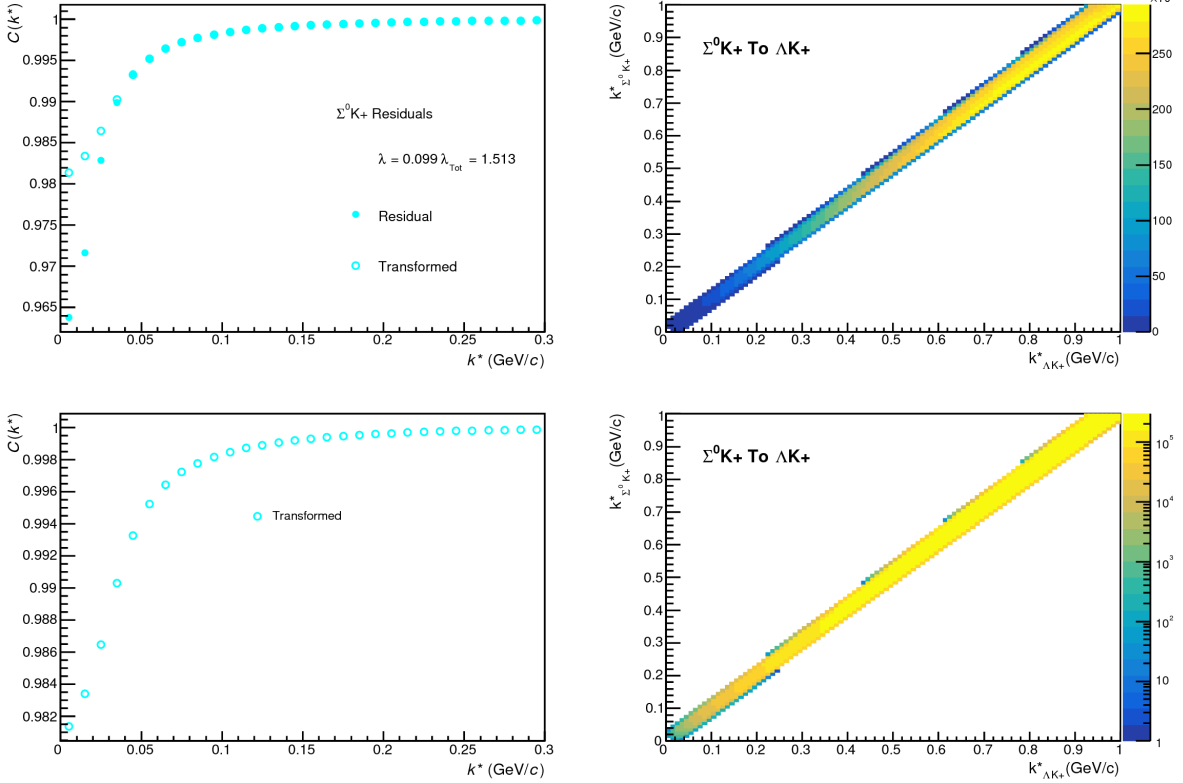
$$R_{AB} = R_{\Lambda K} \left( \frac{m_{T,AB}}{m_{T,\Lambda K}} \right)^{-1/2} \quad (19)$$

The values for  $m_T$  for each pair system was taken from THERMINATOR. As the fitter dances around parameter space and selects new radii for the  $\Lambda K$  pairs, the radii of the residuals is scaled by the above factor. In the end, this scaling factor made no significant difference in our fit results, so this complication is excluded from our final results. Note that this is not surprising, as the most extreme scaling factor was, in the case of using 10 residual systems, between  $\Lambda K^+$  with  $m_{T,\Lambda K^+} \approx 1.4 \text{ GeV}/c^2$  and  $\Xi^- K^{*0}$  with  $m_{T,\Xi^- K^{*0}} \approx 1.8 \text{ GeV}/c^2$ , resulting in a scale factor of  $\approx 0.9$ .

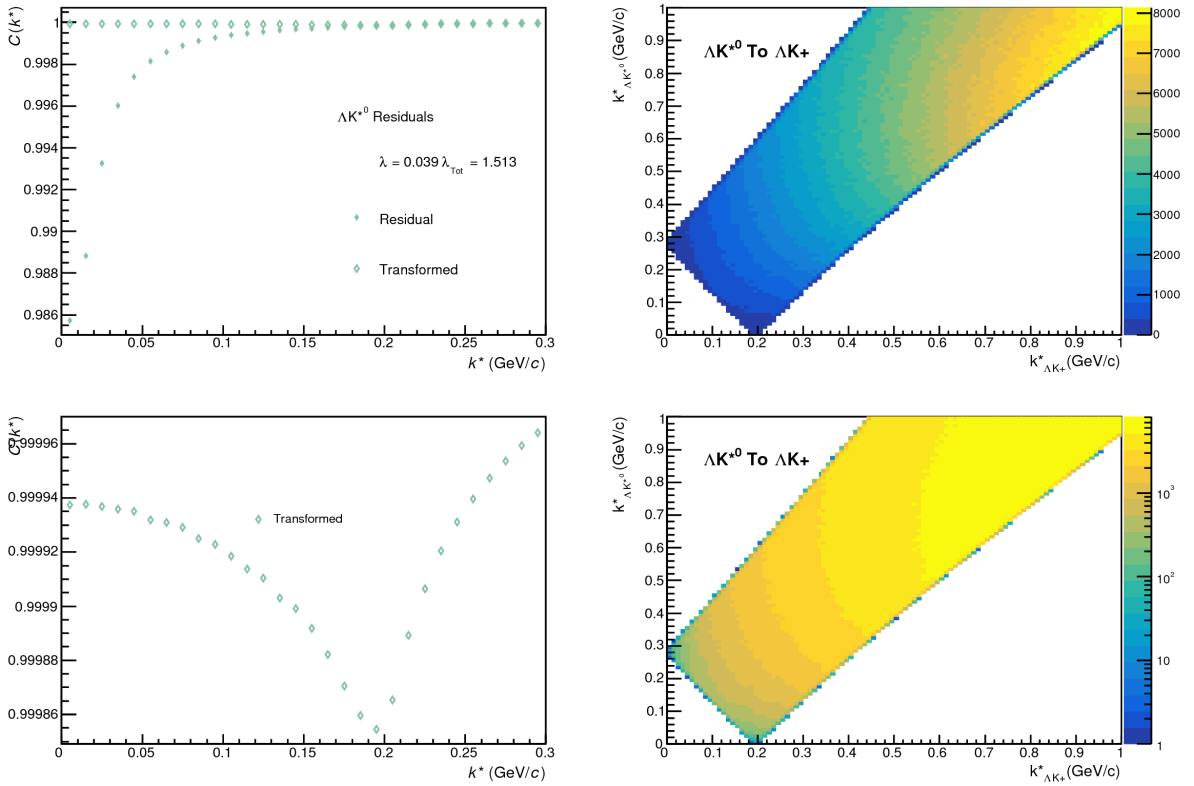
Now, as hinted above, accounting for charged residuals adds a complication in that they necessitate the inclusion of the CoulombFitter into the process. The complication of combining the two fitters is not troubling, but it increases the fitting time drastically (the parallelization of the CoulombFitter across a large number of GPU cores, to drastically decrease run-time, is currently underway). We have two solutions to bypass such a large increase in run time. First, we can use our experimental  $\Xi^{\text{ch}} K^{\text{ch}}$  data to represent all charged parent pair system. In this case, there is no need to make any assumption about scattering parameters or source sizes, as we already have the experimental data. The downside is that, especially in the 30-50% centrality bin, the error bars on the data are large. Alternatively, we can assume the strong interaction is negligible in the charged residual, and generate the parent correlation function given radius and  $\lambda$  parameters. We find in our  $\Xi^{\text{ch}} K^{\text{ch}}$  study that a Coulomb-only description of the system describes, reasonably well, the broad features of the correlation. The strong interaction is necessary for the fine details. However, as these correlations are run through a transform matrix, which largely flattens out and fine details, a Coulomb-only description should be sufficient. In practice, this Coulomb-only scenario is achieved by first building a large number of Coulomb-only correlations for various radii and  $\lambda$  parameter values, and interpolating from this grid during the fitting process. We find consistent results between using the  $\Xi K$  data and the Coulomb-only interpolation method. When the number of residual pairs used is increased to 10, so that pairs such as  $\Sigma^{*+} K^-$  enter the picture, the Coulomb-only interpolation method is used. In other words, the  $\Xi K$  experimental data is only used to model the  $\Xi K$  residual contribution, all other charged pairs are treated with the Coulomb-only interpolation method.

Two examples of how very different transform matrices can alter a correlation function are shown in Figures 22 and 23 below. These figures were taken using parameter values obtained from fits to the data. In the top left corner of the figures, the input correlation function (closed symbols) is shown together

549 with the output, transformed, correlation function (open symbols). In the bottom left, the transformed  
 550 correlation is shown by itself. This is especially helpful when the  $\lambda$  parameter is very small, in which  
 551 case the contribution in the top left can look flat, but the zoomed in view in the bottom left shows the  
 552 structure. The right two plots in each figure show the transform matrix without (top right) and with  
 553 (bottom right) a log-scale on the z-axis. Note, more examples of these transforms can be found in Sec.  
 554 9.



**Fig. 22:**  $\Sigma^0 K^+$  Transform. These figures were taken using parameter values obtained from fits to the data. In the top left corner of the figures, the input correlation function (closed symbols) is shown together with the output, transformed, correlation function (open symbols). In the bottom left, the transformed correlation is shown by itself. The right two plots in each figure show the transform matrix without (top right) and with (bottom right) a log-scale on the z-axis.



**Fig. 23:**  $\Sigma^0 K^+$  Transform. These figures were taken using parameter values obtained from fits to the data. In the top left corner of the figures, the input correlation function (closed symbols) is shown together with the output, transformed, correlation function (open symbols). In the bottom left, the transformed correlation is shown by itself. The right two plots in each figure show the transform matrix without (top right) and with (bottom right) a log-scale on the z-axis.

## 555 5.5 Non-Flat Background

556 We observe a significant non-femtoscopic, non-flat, background in all of our correlations at large  $k^*$ .  
 557 This background increases with decreasing centrality, is the same amongst all  $\Lambda K^\pm$  pairs, and is more  
 558 pronounced in the  $\Lambda K_S^0$  system, as can be seen in Fig. 24.

559 It is important to note that the difference in  $\Lambda K^\pm$  and  $\Lambda K_S^0$  backgrounds is due mainly to the difference in  
 560 kinematic cuts, not due to any interesting physics. Figure 25a shows that THERMINATOR 2 simulation  
 561 does a good job of describing the difference of backgrounds in  $\Lambda K^\pm$  and  $\Lambda K_S^0$ . Figure 25b show that  
 562 when restrictions are imposed on the  $p_T$  of the  $K_S^0$  to more closely match the  $K^\pm$  cuts, the backgrounds  
 563 align much better. Therefore, we conclude that the difference in background between  $\Lambda K^\pm$  and  $\Lambda K_S^0$   
 564 observed in our experimental data is simply due to a difference in kinematic cuts between  $K^\pm$  and  $K_S^0$   
 565 particles.

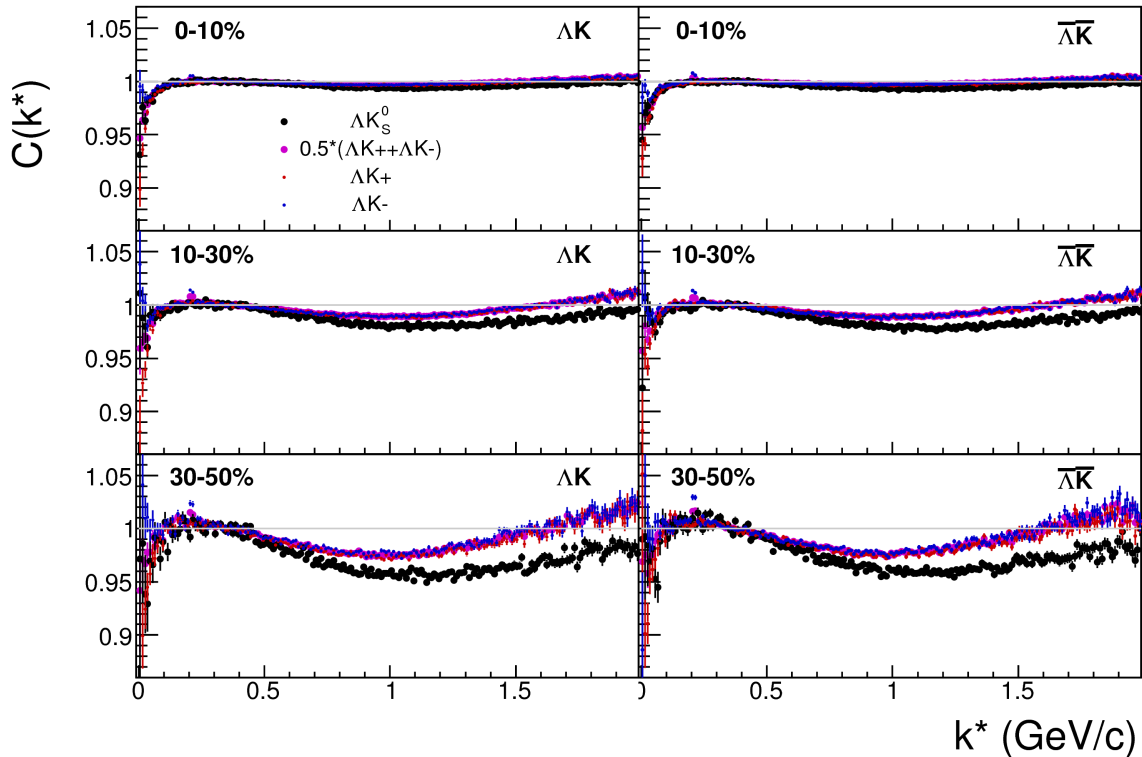
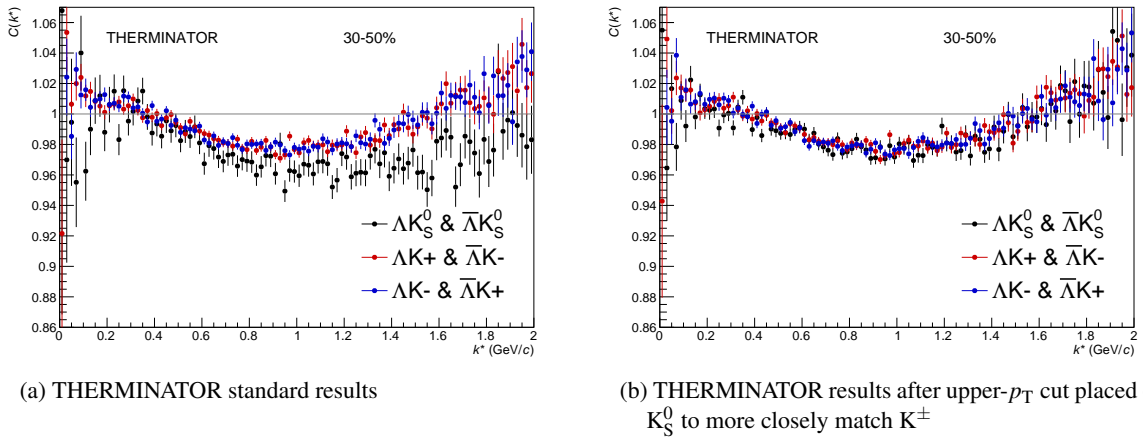


Fig. 24: Compare backgrounds

566 It is suggested that this background effect is due primarily to particle collimation associated with elliptic  
 567 flow [8]. More specifically, these backgrounds result from mixing events with unlike event-plane angles  
 568 ( $\Psi_{EP}$ ). As explained in [8], when elliptic flow is present, all particles are more likely to be emitted  
 569 in a specific direction (in-plane), as opposed to a perpendicular direction. Therefore, the difference in  
 570 momenta for pairs of particles tends to be smaller, compared to the case of no flow. In the case of mixed-  
 571 event pairs, the two events used do not share an event-plane, and therefore this is no collimation effect  
 572 in the pairs from flow. As a result, pairs with larger momentum are more likely when mixed-events are  
 573 used, and the correlation function will be observed below unity. In general, a dip below unity, at a given  
 574  $k^*$ , means it is more probable to find a pair at that  $k^*$  when the daughters are taken from mixed-events, as  
 575 compared to when they are taken from the same event.

576 This same reasoning suggests that the background should lead to an enhancement at low- $k^*$ . The en-  
 577 hancement at high- $k^*$  ( $k^* \gtrsim 1.5$  GeV/c) does not result from the collective flow of the system. We are not



**Fig. 25:** THERMINATOR 2 simulation for  $\Lambda K^+$  (red),  $\Lambda K^-$  (blue), and  $\Lambda K_S^0$  (black). In 25a, we should the standard THERMINATOR 2 results. THERMINATOR 2 does a good job describing qualitatively the different between the  $\Lambda K^\pm$  and  $\Lambda K_S^0$  backgrounds. In 25b, an upper- $p_T$  cut was placed on the  $K_S^0$  particles to more closely match the  $K^\pm$  kinematic cuts. After this tweak, the  $\Lambda K^\pm$  and  $\Lambda K_S^0$  results agree much better.

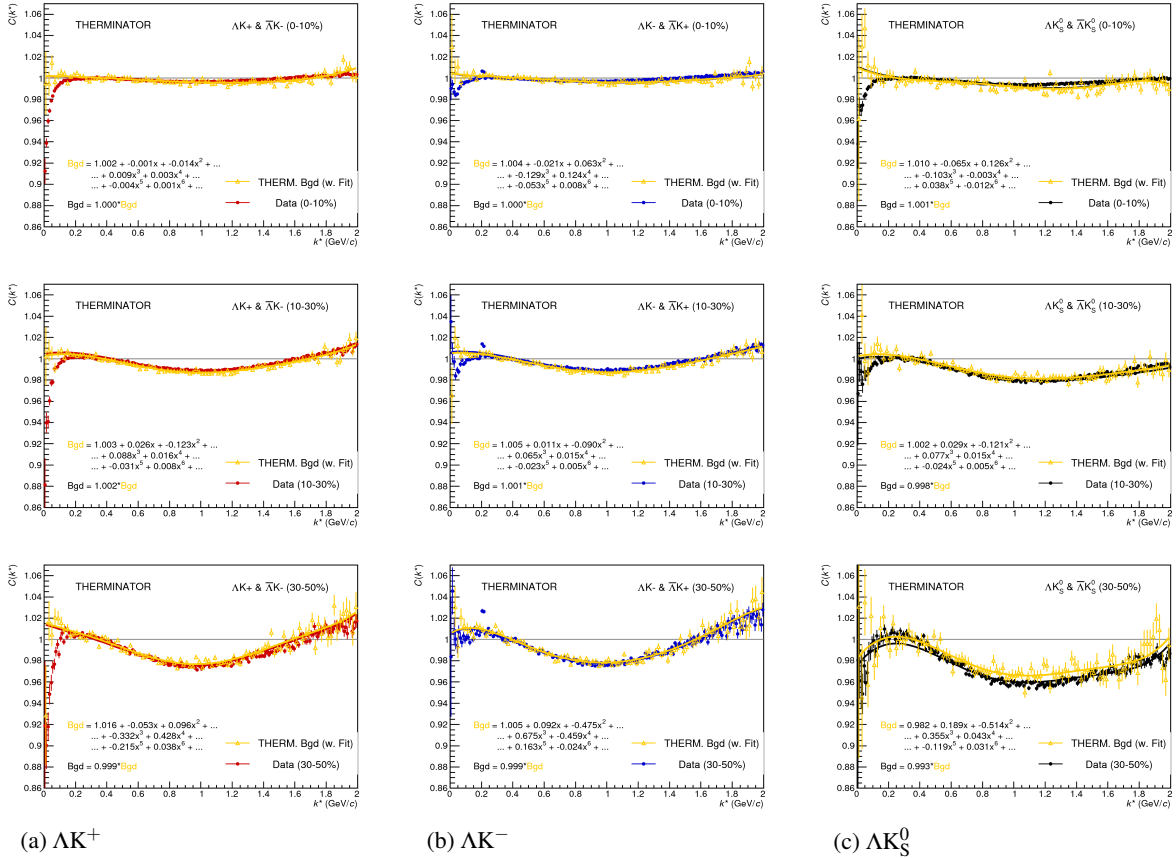
578 certain was causes this enhancement, but typical suspects are jet-like correlations and resonance decays.

We can split our correlation functions into three main regions. First, the low- $k^*$  region ( $k^* \lesssim 0.3$  GeV/c) contains the femtoscopic correlations, as well as a likely enhancement from the background. The intermediate- $k^*$  region ( $0.3 \lesssim k^* \gtrsim 1.5$  GeV/c) contains a suppression from the background. Finally, the high- $k^*$  region ( $k^* \gtrsim 1.5$  GeV/c) contains an enhancement with unknown origin.

583 THERMINATOR 2 simulation has been shown to reproduce the background features in a  $\pi K$  analysis  
 584 [8]. As the background effect can be attributed mainly to elliptic flow, which is a global feature of the  
 585 system, we suspected THERMINATOR 2 could also, at least qualitatively, describe our backgrounds.  
 586 After ensuring each simulated event received a random event-plane angle ( $\Psi_{EP}$ )<sup>1</sup>, we found THERMI-  
 587 NATOR 2 did a good job of describing our data qualitatively, and, in some cases, quantitatively. Figure  
 588 26 shows the THERMINATOR 2 simulation (gold) together with experimental data (red, blue, or black)  
 589 The figure also shows a 6<sup>th</sup>-order polynomial fit to the simulation (gold), as well as the fit polynomial  
 590 scaled to match the data (red, blue, black).

Figure 27 shows three different correlation function generated using THERMINATOR 2 simulation ("Cf w/o Bgd (A)", "Cf w. Bgd (B)", "Bgd(C)"), as well as two histograms describing the relation between the three ("Ratio (B/C)", "1+Diff(B-C)"). Cf w/o Bgd (A)" shows a correlation function with a femtoscopic correlation, but without background. When THERMINATOR 2 is run without randomizing event planes, and therefore having all events share a common event plane, no non-flat background is observed, as expected. The femtoscopic correlation effect was introduced by assuming scattering parameters for the system, and weighting the numerators appropriately. The second correlation, "Cf w. Bgd (B)", shows a correlation function with both a femtoscopic correlation and a background (most closely matches our situation in experiment). To generate the background, each event was given a random event-plane angle, as is given to us in experiment. To generate the femtoscopic correlation, the same numerator weighting procedure was used. Finally, "Bgd (C)", shows a correlation function with a non-femtoscopic background, but no femtoscopic correlation, i.e. background only. This is generated just as "Cf w. Bgd (B)", with randomized event planes, but unit weights are used when filling the numerators, so no femtoscopic effects are included.

<sup>1</sup>default was for all events to share a common event plane



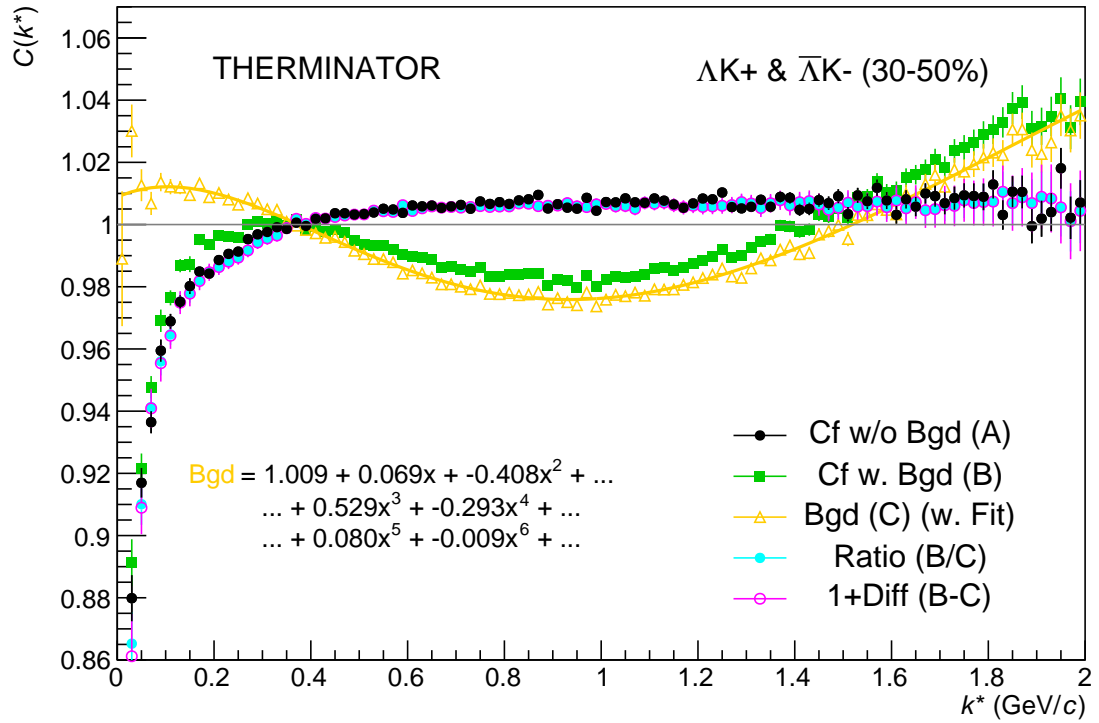
**Fig. 26:** THERMINATOR 2 simulation (gold) together with experimental data (red, blue, or black). The left column shows results for  $\Lambda K^+$  (26a), middle for  $\Lambda K^-$  (26b), and right for  $\Lambda K_S^0$  (26c). A 6<sup>th</sup>-order polynomial fit to the simulation is shown as a solid gold line, and whose fit parameters are printed on the lower left of each plot. This polynomial is scaled to match the experimental data; the value of this scale is printed in the lower left corner of each plot. The polynomial fit with scale factor applied is drawn in a color matching the experimental data (red, blue, black).

605 The main point of Fig. 27 is that the black points match the blue (and purple) points; or, equivalently:

$$C_{fw/oBgd} = \frac{C_{fw.Bgd}}{Bgd} \rightarrow C_{theory} = \frac{C_{exp}}{F_{Bgd}} \rightarrow C_{exp} = C_{theory} \cdot F_{Bgd} \quad (20)$$

606 As shown and described in Fig 27 and Eq. 20, THERMINATOR 2 simulation shows the non-femtoscopic  
607 background affects the correlation function as a separable scale factor. We expect this behavior to be  
608 roughly the same in the experimental data.

609 Figure 28 demonstrates the use of the Stavinsky method with THERMINATOR 2. In the figure, unit  
610 weights were used for all numerators, so no femtoscopic signal is included, only background effects.  
611 The black points show an ideal, experimentally unreachable, situation of aligning all of the event-plane  
612 angles. With THERMINATOR 2, when the event-planes are aligned, the background signal is killed. The  
613 green points show the experimental situation of random event-plane angles. The purple points shown the  
614 affect of applying the Stavinsky method to the case of random event-planes. The figure shows that this  
615 method effectively kills the non-flat background (i.e. the procedure takes the green points to the purple).  
616 Finally, the blue points show the effect of applying the Stavinsky method when all of the event-planes  
617 are aligned. This shows that the Stavinsky method does not introduce any signal to an already flat



**Fig. 27:** Correlation with background decomposition with THERMINATOR. "Cf w/o Bgd (A)" shows a correlation function with a femtoscopic correlation, but without background. "Cf w. Bgd (B)", shows a correlation function with both a femtoscopic correlation and a background (most closely matches our situation in experiment). "Bgd (C)", shows a correlation function with a non-femtoscopic background, but no femtoscopic correlation, i.e. background only.

background.

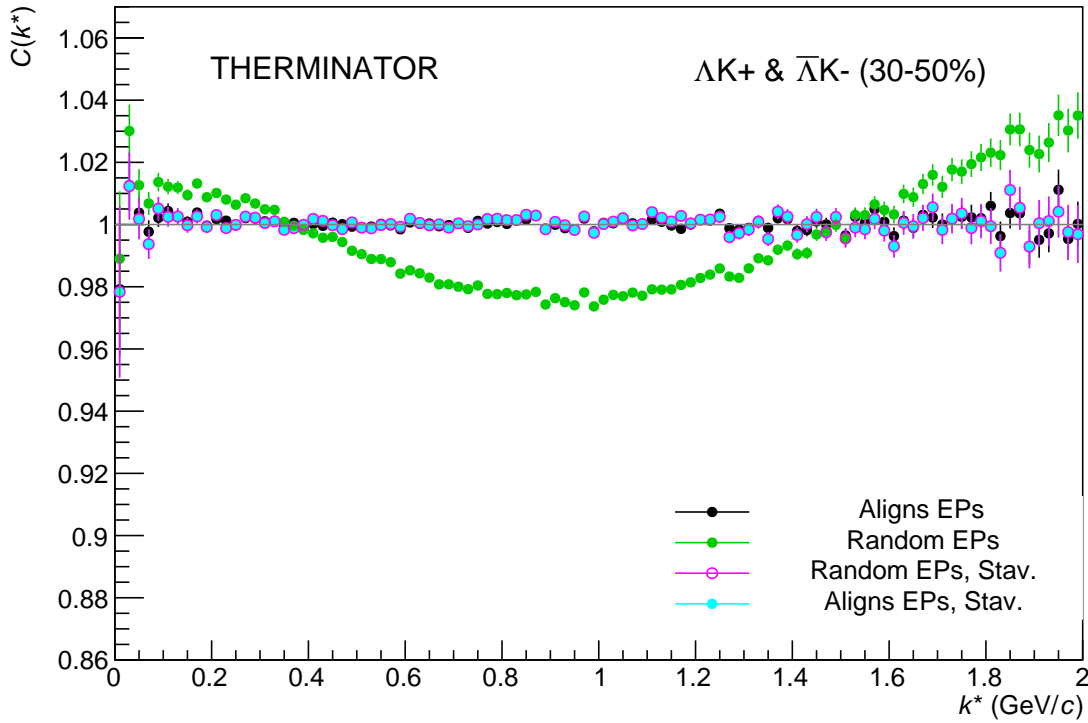
## 5.6 LednickyFitter

The code developed to fit the data is called "LednickyFitter", and utilizes the ROOT TMinuit implementation of the MINUIT fitting package. In short, given a function with a number of parameters, the fitter explores the parameter space searching for the minimum of the equation. In this implementation, the function to be minimized should represent the difference between the measure and theoretical correlation functions. However, a simple  $\chi^2$  test is inappropriate for fitting correlation functions, as the ratio two Poisson distributions does not result in a Poisson distribution. Instead, a log-likelihood fit function of the following form is used [2]:

$$\chi_{PML}^2 = -2 \left[ A \ln \left( \frac{C(A+B)}{A(C+1)} \right) + B \ln \left( \frac{A+B}{B(C+1)} \right) \right] \quad (21)$$

where  $A$  is the experimental signal distribution (numerator),  $B$  is the experimental background distribution (denominator), and  $C$  is the theoretical fit correlation function.

The LednickyFitter uses Equations 5 – 7 to build the theoretical fit, and Equation 21 as the statistic quantifying the quality of the fit. The parameters to be varied by MINUIT are:  $\lambda$ ,  $R$ ,  $f_0$  ( $\mathbb{R}f_0$  and  $\mathbb{I}f_0$  separately),  $d_0$ , and normalization  $N$ . The fitter currently includes methods to correct for momentum resolution and a non-flat background. These corrections are applied to the fit function, the data is never



**Fig. 28:** The use of the Stavinsky method with THERMINATOR 2. Unit weights were used for all numerators, so no femtoscopic signal is included, only background effects. The black points show an ideal, experimentally unreachable, situation of aligning all of the event-plane angles. The green points show the experimental situation of random event-plane angles. The purple points show the affect of applying the Stavinsky method to the case of random event-planes. Finally, the blue points show the effect of applying the Stavinsky method when all of the event-planes are aligned.

touched. The fitter is able to share parameters between different analyses and fit all simultaneously.  
 In a typical fit, a given pair is fit with its conjugate (ex.  $\Lambda K^+$  with  $\bar{\Lambda} K^-$ ) across all centralities (0-10%, 10-30%, 30-50%), for a total of 6 simultaneous analyses. Each analysis has a unique  $\lambda$  and normalization parameter. The radii are shared between analyses of like centrality, as these should have similar source sizes. The scattering parameters ( $\mathbb{R}f_0$ ,  $\mathbb{I}f_0$ ,  $d_0$ ) are shared amongst all.  
 In the case of fitting with residuals, the  $\lambda_{Fit}$  parameter serves as an overall normalization shared by all contributors, such that Eqn 17 becomes:

$$C_{measured}(k_{\Lambda K}^*) = 1 + \sum_i \lambda'_i [C_i(k_{\Lambda K}^*) - 1] \quad (22)$$

$$\lambda'_i = \lambda_{Fit} \lambda_i$$

$$\sum_i \lambda'_i = \lambda_{Fit} \sum_i \lambda_i = \lambda_{Fit}$$

where  $\lambda_i$  is obtained from THERMINATOR, as explained in Section 5.4, and whose values are presented in Tables ?? through ???. For Coulomb-neutral pairs, such as  $\Lambda K$ ,  $\Sigma^0 K$ , and  $\Xi^0 K$ ,  $C_i(k_{\Lambda K}^*)$  is calculated from Eqn. 5, with the help of Eqn. 7. For those residual pairs which include a Coulomb interaction,  $C_i(k_{\Lambda K}^*)$  is either calculated using the CoulombFitter method (Sections 5.2 and 5.7) with no strong interaction, or by using the  $\Xi^{ch} K^{ch}$  data directly. Unless otherwise stated, the  $\Xi^{ch} K^{ch}$  residual contribution

645 is modeled using the experimental  $\Xi^{\text{ch}}\text{K}^{\text{ch}}$  data, and all other charged contributors (ex.  $\Sigma^{\ast\text{ch}}\text{K}^{\text{ch}}$ ) are  
646 modeled using the CoulombFitter technique with no strong interaction contribution.

647 To summarize, the complete fit function is constructed as follows:

648 1. The uncorrected correlation function,  $C'_{Fit}(k_{True}^*)$ , is constructed using Eq. 22 (with the help of  
649 Eqns. 5 and 7, as well as Secs. 5.2 and 5.7)

- 650 – in the case of no residual contributions included in the fit,  $\lambda_i = \lambda_{\Lambda K}$  in Eq. 22 is set equal to  
651    1. Then, the extracted  $\lambda_{Fit}$  parameter should be roughly equal to the pair purity.  
652    – when residuals are included, the  $\lambda_i$  values are presented in Tables ?? through ??.

653 2. The correlation function is corrected to account for momentum resolution effects using Eq. 14

$$654 - C'_{Fit}(k_{Rec}^*) = \frac{\sum_{k_{True}^*} M_{k_{Rec}, k_{True}^*} C'_{Fit}(k_{True}^*)}{\sum_{k_{True}^*} M_{k_{Rec}, k_{True}^*}}$$

655 3. Finally, the non-flat background correction is applied, and the final fit function is obtained

$$656 - C_{Fit}(k_{Rec}^*) = C'_{Fit}(k_{Rec}^*) * F_{Bgd}(k_{Rec}^*)$$

657 Figures 30, 31, and 32 (35, 36, and 37, or 42, 43, and 44), in Section 7, show experimental data with fits  
658 for all studied centralities for  $\Lambda K_S^0$  with  $\bar{\Lambda} K_S^0$ ,  $\Lambda K^+$  with  $\bar{\Lambda} K^-$ , and  $\Lambda K^-$  with  $\bar{\Lambda} K^+$ , respectively. In the  
659 figures, the black solid line represents the “raw” fit, i.e. not corrected for momentum resolution effects  
660 nor non-flat background. The green line shows the fit to the non-flat background. The purple points  
661 show the fit after momentum resolution, non-flat background, and residual correlations (if applicable)  
662 corrections have been applied. The initial values of the parameters is listed, as well as the final fit values  
663 with uncertainties.

## 664 5.7 Coulomb Fitter

665 When fitting the  $\Xi^-(\bar{\Xi}^+)\text{K}^\pm$  results, it is necessary to include both strong and Coulomb effects. In this  
666 case, Equation 5 is no longer valid, and, in fact, there is no analytical form with which to fit. Therefore,  
667 we must begin with the wave function describing the pair interaction, and simulate many particle pairs  
668 to obtain a theoretical fit correlation function. The code developed to achieve this functionality is called  
669 “CoulombFitter”. Currently, in order to generate the statistics needed for a stable fit, we find that  $\sim 10^4$   
670 simulated pairs per 10 MeV bin are necessary. Unfortunately, the nature of this process means that the  
671 “CoulombFitter” takes much longer to run than the “LednickyFitter” of Section 5.1.

672 Unfortunately, with this analysis, we are not sensitive to, and therefore not able to distinguish between,  
673 the iso-spin singlet and triplet states. We proceed with our analysis, but the results must be interpreted  
674 as iso-spin averaged scattering parameters.

675 As stated before, to generate a fit correlation function, we must simulate a large number of pairs, calculate  
676 the wave-function, and average  $\Psi^2$  over all pairs in a given  $k^*$  bin. Essentially, we calculate Equation 9  
677 by hand:

$$678 \begin{aligned} C(\mathbf{k}^*) &= \sum_S \rho_S \int S(\mathbf{r}^*) |\Psi_{\mathbf{k}^*}^S(\mathbf{r}^*)|^2 d^3 \mathbf{r}^* \\ &\longrightarrow C(|\mathbf{k}^*|) \equiv C(k^*) = \sum_S \rho_S \langle |\Psi^S(\mathbf{k}_i^*, \mathbf{r}_i^*)|^2 \rangle_i \\ &\longrightarrow C(k^*) = \lambda \sum_S \rho_S \langle |\Psi^S(\mathbf{k}_i^*, \mathbf{r}_i^*)|^2 \rangle_i + (1 - \lambda) \end{aligned} \quad (23)$$

678 where  $\langle \rangle_i$  represents an average over all pairs in a given  $k^*$  bin.

679 In summary, for a given  $k^*$  bin, we must draw  $N_{pairs} \sim 10^4$  pairs, and for each pair:

680 1. Draw a random  $\mathbf{r}^*$  vector according to our Gaussian source distribution  $S(\mathbf{r}^*)$

681 2. Draw a random  $\mathbf{k}^*$  vector satisfying the  $|\mathbf{k}^*|$  restriction of the bin

682 – We draw from real  $k^*$  vectors obtained from the data

683 – However, we find that drawing from a distribution flat in  $k^*$  gives similar results

684 3. Construct the wave-function  $\Psi$

685 After all pairs for a given  $k^*$  bin are simulated and wave-functions obtained, the results are averaged to  
686 give the fit result.

687 Construction of the wave-functions, Equation 10, involves a number of complex functions not included  
688 in standard C++ or ROOT libraries (namely,  $h(\eta)$ ,  $\tilde{G}(\rho, \eta)$ ), and  $F(-i\eta, 1, i\xi)$ . These functions were  
689 even difficult to find and implement from elsewhere. Our solution was to embed a Mathematica kernel  
690 into our C++ code to evaluate these functions. However, having Mathematica work on-the-fly with the  
691 fitter was far too time consuming (fitter would have taken day, maybe weeks to finish). Our solution  
692 was to use Mathematica to create matrices representing these functions for different parameter values.  
693 During fitting, these matrices were then interpolated and the results used to build the wave-functions.  
694 This method decreased the running time dramatically, and we are not able to generate results in under  $\sim$   
695 1 hour. This process will be explained in more detail in future versions of the note.

## 696 6 Systematic Errors

697 In order to understand my systematic uncertainties, the analysis code was run many times using slightly  
698 different values for a number of important cuts, and the results were compared.

699 In order to quantify the systematic errors on the data, all correlation functions built using all varied cut  
700 values were bin-by-bin averaged, and the resulting variance of each bin was taken as the systematic error.  
701 The cuts which were utilized in this study are presented in Sections 6.1.1 ( $\Lambda K_S^0$ ) and 6.2.1 ( $\Lambda K^\pm$ ).

702 Similarly, the fit parameters extracted from all of these correlation functions were averaged, and the  
703 resulting variances were taken as the systematic errors for the fit parameters. As with the systematic  
704 errors on the data, this was performed for all varied cut values. Additionally, a systematic analysis was  
705 done on our fit method (which, for now, just includes our choice of fit range). These two sources of  
706 uncertainty were combined in quadrature to obtain the final systematic uncertainties on the extracted fit  
707 parameters.

### 708 6.1 Systematic Errors: $\Lambda K_S^0$

#### 709 6.1.1 Particle and Pair Cuts

710 The cuts included in the systematic study, as well as the values used in the variations, are listed below.

711 Note, the central value corresponds to that used in the analysis.

#### 712 6.1.2 Non-Flat Background

713 We fit our non-flat background with a linear function. To study the contribution of this choice to our sys-  
714 tematic errors, we also fit with a quadratic and Gaussian form. The resulting uncertainties are combined  
715 with the uncertainties arising from our particle cuts.

$\Lambda K_S^0$ systematics	
DCA $\Lambda(\bar{\Lambda})$	4, 5, 6 mm
DCA $K_S^0$	2, 3, 4 mm
DCA $\Lambda(\bar{\Lambda})$ Daughters	3, 4, 5 mm
DCA $K_S^0$ Daughters	2, 3, 4 mm
$\Lambda(\bar{\Lambda})$ Cosine of Pointing Angle	0.9992, 0.9993, 0.9994
$K_S^0$ Cosine of Pointing Angle	0.9992, 0.9993, 0.9994
DCA to Primary Vertex of $p(\bar{p})$ Daughter of $\Lambda(\bar{\Lambda})$	0.5, 1, 2 mm
DCA to Primary Vertex of $\pi^-(\pi^+)$ Daughter of $\Lambda(\bar{\Lambda})$	2, 3, 4 mm
DCA to Primary Vertex of $\pi^+$ Daughter of $K_S^0$	2, 3, 4 mm
DCA to Primary Vertex of $\pi^-$ Daughter of $K_S^0$	2, 3, 4 mm
Average Separation of Like-Charge Daughters	5, 6, 7 cm

**Table 2:**  $\Lambda K_S^0$  systematics

716 **6.1.3 Fit Range**

717 Our choice of  $k^*$  fit range was varied by  $\pm 25\%$ . The resulting uncertainties in the extracted parameter  
718 sets were combined with our uncertainties arising from our particle and pair cuts.

719 **6.2 Systematic Errors:  $\Lambda K^\pm$**

720 **6.2.1 Particle and Pair Cuts**

721 The cuts included in the systematic study, as well as the values used in the variations, are listed below.  
722 Note, the central value corresponds to that used in the analysis.

$\Lambda K^\pm$ systematics	
DCA $\Lambda(\bar{\Lambda})$	4, 5, 6 mm
DCA $\Lambda(\bar{\Lambda})$ Daughters	3, 4, 5 mm
$\Lambda(\bar{\Lambda})$ Cosine of Pointing Angle	0.9992, 0.9993, 0.9994
DCA to Primary Vertex of $p(\bar{p})$ Daughter of $\Lambda(\bar{\Lambda})$	0.5, 1, 2 mm
DCA to Primary Vertex of $\pi^-(\pi^+)$ Daughter of $\Lambda(\bar{\Lambda})$	2, 3, 4 mm
Average Separation of $\Lambda(\bar{\Lambda})$ Daughter with Same Charge as $K^\pm$	7, 8, 9 cm
Max. DCA to Primary Vertex in Transverse Plane of $K^\pm$	1.92, 2.4, 2.88
Max. DCA to Primary Vertex in Longitudinal Direction of $K^\pm$	2.4, 3.0, 3.6

**Table 3:**  $\Lambda K^\pm$  systematics

723 **6.2.2 Non-Flat Background**

724 We fit our non-flat background with a linear function. To study the contribution of this choice to our sys-  
725 tematic errors, we also fit with a quadratic and Gaussian form. The resulting uncertainties are combined  
726 with the uncertainties arising from our particle cuts.

727 **6.2.3 Fit Range**

728 Our choice of  $k^*$  fit range was varied by  $\pm 25\%$ . The resulting uncertainties in the extracted parameter  
729 sets were combined with our uncertainties arising from our particle and pair cuts.

730 **6.3 Systematic Errors:  $\Xi K^\pm$**

731 **6.3.1 Particle and Pair Cuts**

732 The cuts included in the systematic study, as well as the values used in the variations, are listed below.

733 Note, the central value corresponds to that used in the analysis.

$\Xi^- K^\pm$  systematics

Max. DCA $\Xi(\bar{\Xi})$	2, 3, 4 mm
Max. DCA $\Xi(\bar{\Xi})$ Daughters	2, 3, 4 mm
Min. $\Xi(\bar{\Xi})$ Cosine of Pointing Angle to Primary Vertex	0.9991, 0.9992, 0.9993
Min. $\Lambda(\bar{\Lambda})$ Cosine of Pointing Angle to $\Xi(\bar{\Xi})$ Decay Vertex	0.9992, 0.9993, 0.9994
Min. DCA Bachelor $\pi$	0.5, 1, 2 mm
Min. DCA $\Lambda(\bar{\Lambda})$	1, 2, 3 mm
Max. DCA $\Lambda(\bar{\Lambda})$ Daughters	3, 4, 5 mm
Min. DCA to Primary Vertex of $p(\bar{p})$ Daughter of $\Lambda(\bar{\Lambda})$	0.5, 1, 2 mm
Min. DCA to Primary Vertex of $\pi^-(\pi^+)$ Daughter of $\Lambda(\bar{\Lambda})$	2, 3, 4 mm
Min. Average Separation of $\Lambda(\bar{\Lambda})$ Daughter and $K^\pm$ with like charge	7, 8, 9 cm
Min. Average Separation of Bachelor $\pi$ and $K^\pm$ with like charge	7, 8, 9 cm
Max. DCA to Primary Vertex in Transverse Plane of $K^\pm$	1.92, 2.4, 2.88
Max. DCA to Primary Vertex in Longitudinal Direction of $K^\pm$	2.4, 3.0, 3.6

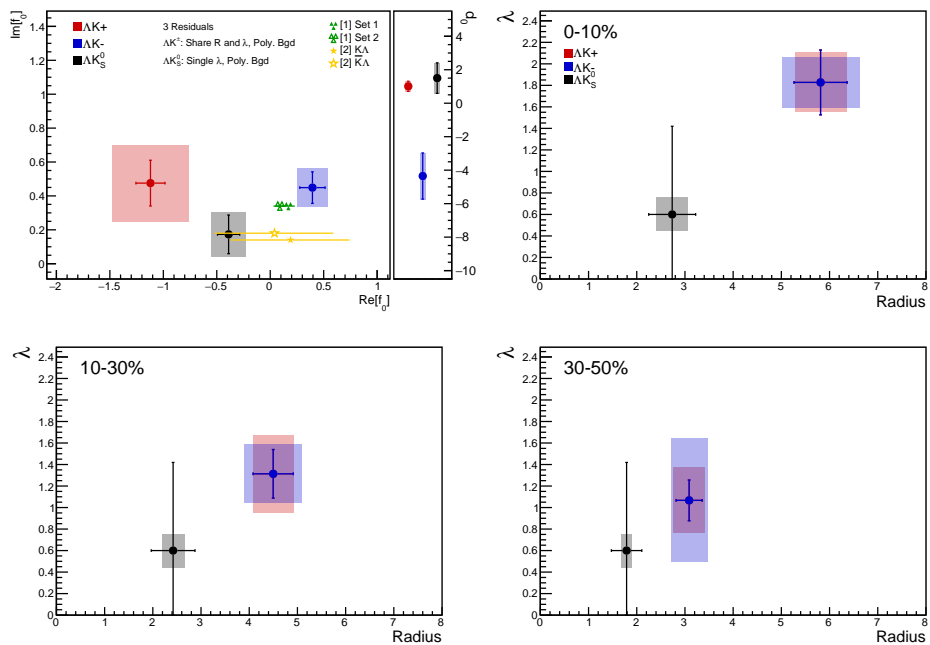
Table 4:  $\Xi^- K^\pm$  systematics

734 **7 Results and Discussion**

735 **7.1 Results:  $\Lambda K_S^0$  and  $\Lambda K^\pm$**

736 In the following sections, we present results assuming (i) no residual correlations (Sec. 7.1.1), (ii) three  
 737 residual contributors (Sec. 7.1.2), and (iii) ten residual contributors (Sec. 7.1.3). We find the case of  
 738 three and ten contributors to be consistent, therefore we will quote the result utilizing three residuals as  
 739 our final result. The results shown, unless otherwise noted, use a polynomial fit to the THERMINATOR  
 740 simulation to handle the non-flat background, and  $\Lambda K^+(\bar{\Lambda} K^-)$  radii are shared with  $\Lambda K^-(\bar{\Lambda} K^+)$ .

741 Before beginning, I first collect a summary of my final results in Figure 29. In the summary plot, we  
 742 show the extracted scattering parameters in the form of a  $\text{Im}[f_0]$  vs  $\text{Re}[f_0]$  plot, which includes the  $d_0$   
 743 values to the right side. We also show the  $\lambda$  vs. radius parameters for all three of our studied centrality  
 744 bins. In Fig. 29, three residual contributors were used, and the background was modeled by a (6<sup>th</sup>-  
 745 )order polynomial fit to THERMINATOR simulation. For the  $\Lambda K_S^0$  results shown in the figure, the  $\Lambda K_S^0$   
 746 and  $\bar{\Lambda} K_S^0$  analyses were fit simultaneously across all centralities (0-10%, 10-30%, 30-50%); scattering  
 747 parameters and a single  $\lambda$  parameter were shared amongst all, the radii were shared amongst results  
 748 of like-centrality, and each has a unique normalization parameter. For the  $\Lambda K^\pm$  results shown, all four  
 749 pair combinations were fit simultaneously ( $\Lambda K^+, \bar{\Lambda} K^-, \Lambda K^-, \bar{\Lambda} K^+$ ) across all centralities. Scattering  
 750 parameters were shared between pair-conjugate systems (i.e. a parameter set describing  $\Lambda K^+$  &  $\bar{\Lambda} K^-$ ,  
 751 and a separate set describing  $\Lambda K^-$  &  $\bar{\Lambda} K^+$ ). For each centrality, a radius and  $\lambda$  parameters were shared  
 752 between all pairs. Each analysis has a unique normalization parameter.



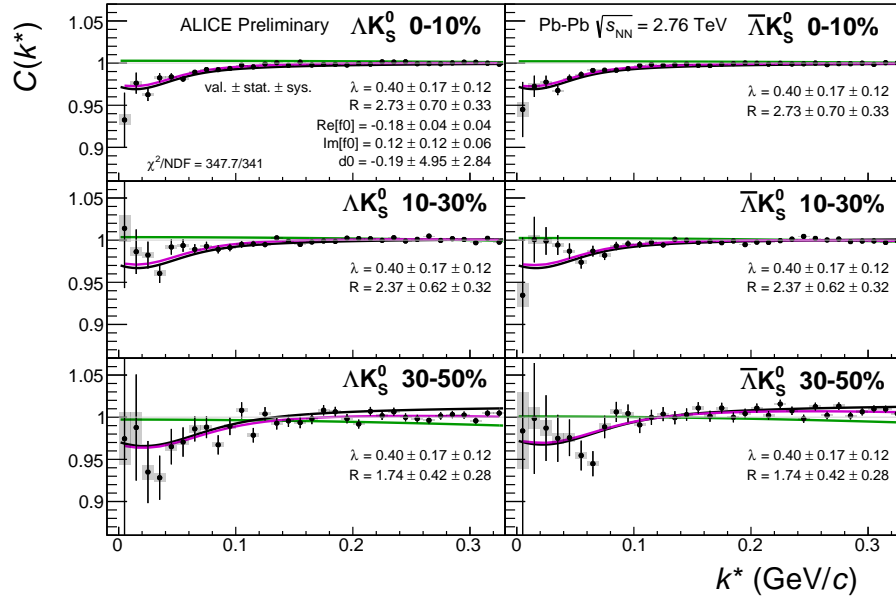
**Fig. 29:** Extracted scattering parameters for the case of 3 residual contributors for all of our  $\Lambda K$  systems. [Top Left]:  $\text{Im}[f_0]$  vs.  $\text{Re}[f_0]$ , together with  $d_0$  to the right. [Top Right (Bottom Left, Bottom Right)]:  $\lambda$  vs. Radius for the 0-10% (10-30%, 30-50%) bin. The green [9] and yellow [10] points show theoretical predictions made using chiral perturbation theory.

753 **7.1.1 Results:  $\Lambda K_S^0$  and  $\Lambda K^\pm$ : No Residual Correlations Included in Fit**

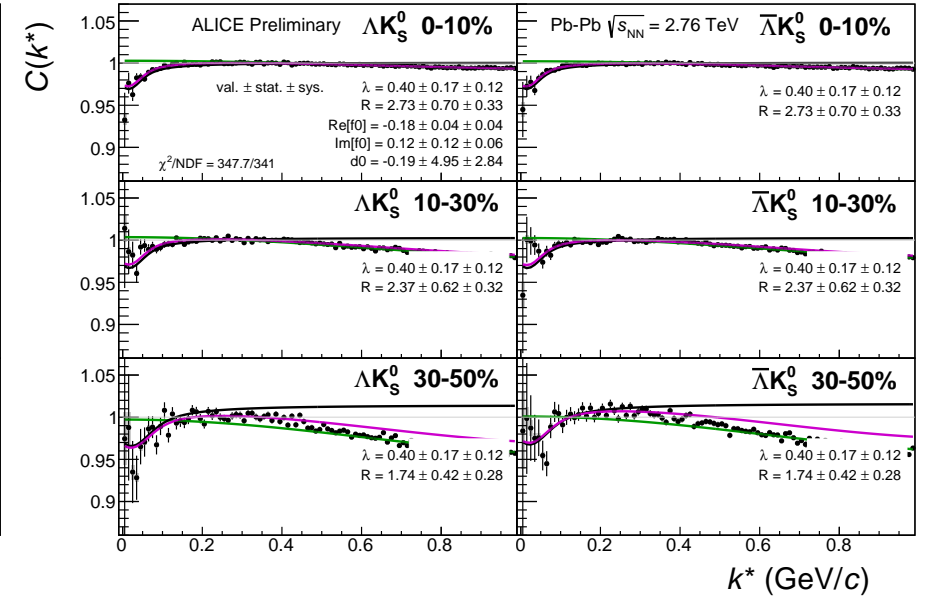
754 Figures 30, 31, and 32 (Section 7) show experimental data with fits for all studied centralities for  $\Lambda K_S^0$   
755 with  $\bar{\Lambda} K_S^0$ ,  $\Lambda K^+$  with  $\bar{\Lambda} K^-$ , and  $\Lambda K^-$  with  $\bar{\Lambda} K^+$ , respectively. The parameter sets extracted from the fits  
756 can be found in Tables 5 and 6. All correlation functions were normalized in the range  $0.32 < k^* < 0.40$   
757 GeV/c, and fit in the range  $0.0 < k^* < 0.30$  GeV/c. For the  $\Lambda K^-$  and  $\bar{\Lambda} K^+$  analyses, the region  $0.19$   
758  $< k^* < 0.23$  GeV/c was excluded from the fit to exclude the bump caused by the  $\Omega^-$  resonance. The  
759 non-flat background was fit with a linear form from  $0.6 < k^* < 0.9$  GeV/c. The theoretical fit function  
760 was then multiplied by this background during the fitting process.

761 In the figures (30, 31, and 32), the black solid line represents the “raw” fit, i.e. not corrected for momen-  
762 tum resolution effects nor non-flat background. The green line shows the fit to the non-flat background.  
763 The purple points show the fit after momentum resolution and non-flat background corrections have been  
764 applied. The initial values of the parameters is listed, as well as the final fit values with uncertainties.

765 For the  $\Lambda K_S^0$  fits without residuals,  $\lambda$  was restricted to [0.4, 0.6].

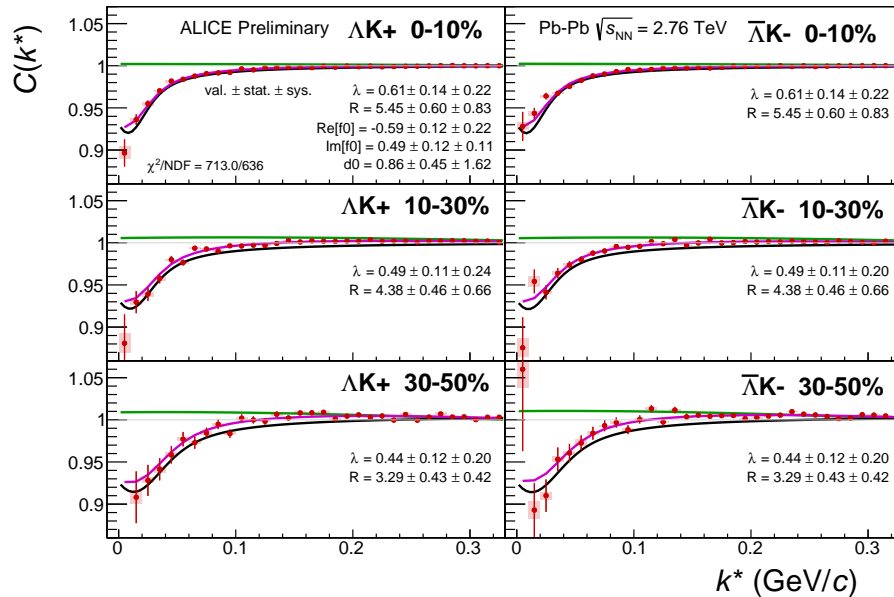


(a) Signal region view ( $k^* \lesssim 0.3$  GeV/c)

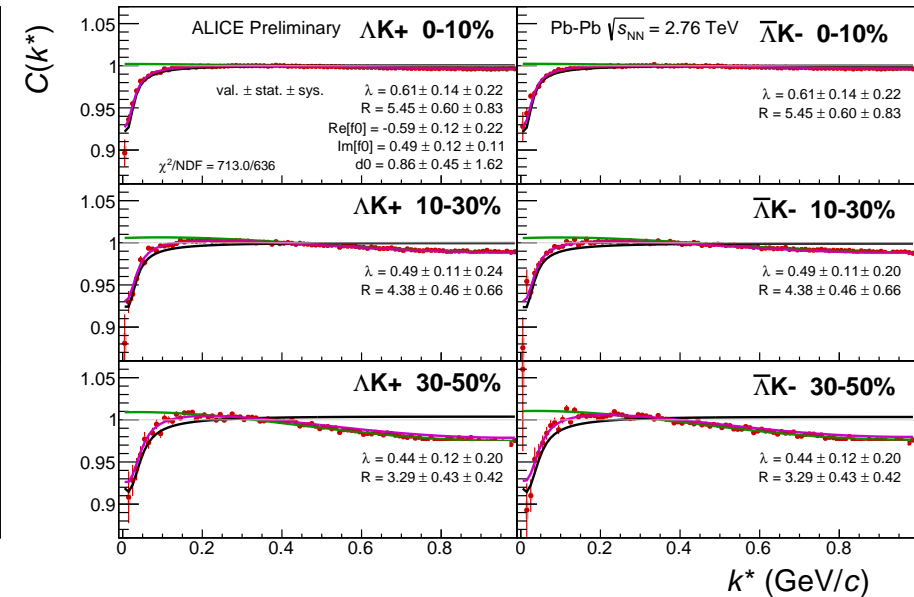


(b) Wide view ( $k^* \lesssim 1.0$  GeV/c)

**Fig. 30:** Fits, with NO residual correlations included, to the  $\Lambda K_S^0$  (left) and  $\bar{\Lambda} K_S^0$  (right) data for the centralities 0-10% (top), 10-30% (middle), and 30-50% (bottom). The lines represent the statistical errors, while the boxes represent the systematic errors. Each has unique  $\lambda$  and normalization parameters. The radii are shared amongst like centralities; the scattering parameters ( $\mathbb{R}f_0$ ,  $\mathbb{I}f_0$ ,  $d_0$ ) are shared amongst all. The black solid line represents the “raw” fit, i.e. not corrected for momentum resolution effects nor non-flat background. The green line shows the fit to the non-flat background. The purple points show the fit after momentum resolution and non-flat background corrections have been applied. The initial values of the parameters is listed, as well as the final fit values with uncertainties. Here,  $R$  was restricted to [2.,10.] and  $\Lambda$  was restricted to [0.1,0.8].

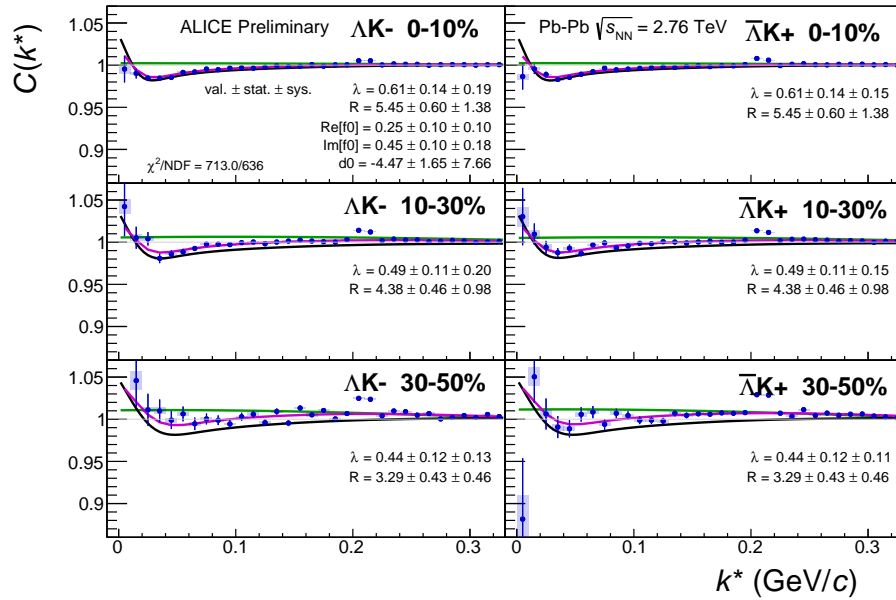


(a) Signal region view ( $k^* \lesssim 0.3 \text{ GeV}/c$ )

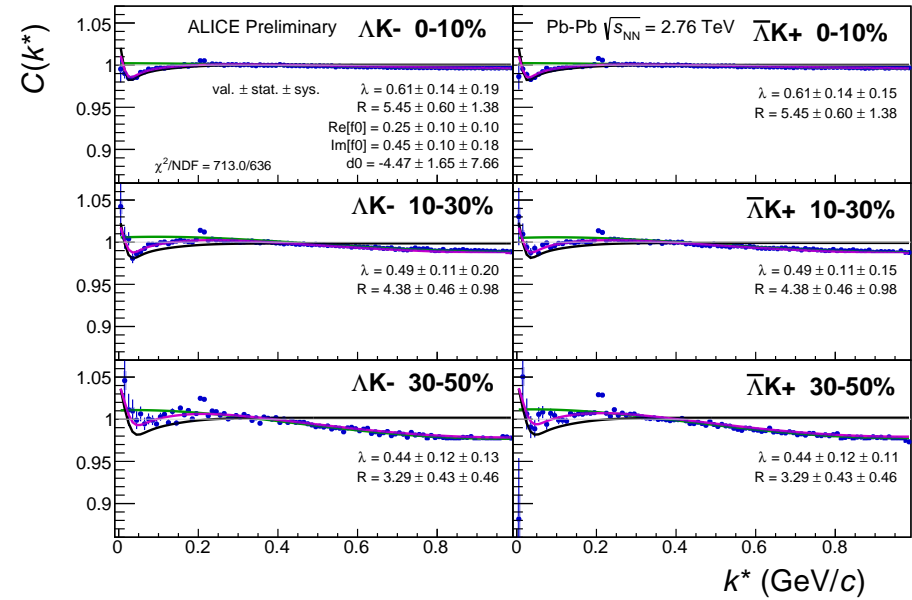


(b) Wide view ( $k^* \lesssim 1.0 \text{ GeV}/c$ )

**Fig. 31:** Fits to the  $\Lambda K^+$  (left) and  $\bar{\Lambda} K^-$  (right) data for the centralities 0-10% (top), 10-30% (middle), and 30-50% (bottom). The lines represent the statistical errors, while the boxes represent the systematic errors. Each has unique  $\lambda$  and normalization parameters. The radii are shared amongst like centralities; the scattering parameters ( $\text{Re}[f_0]$ ,  $\text{Im}[f_0]$ ,  $d_0$ ) are shared amongst all. The black solid line represents the “raw” fit, i.e. not corrected for momentum resolution effects nor non-flat background. The green line shows the fit to the non-flat background. The purple points show the fit after momentum resolution and non-flat background corrections have been applied. The initial values of the parameters is listed, as well as the final fit values with uncertainties.



(a) Signal region view ( $k^* \lesssim 0.3 \text{ GeV}/c$ )



(b) Wide view ( $k^* \lesssim 1.0 \text{ GeV}/c$ )

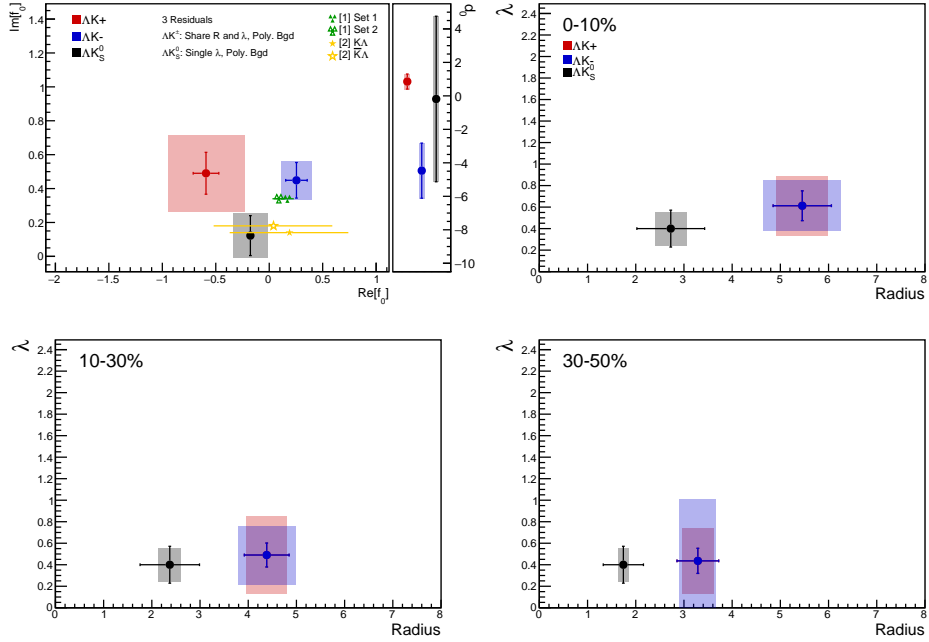
**Fig. 32:** Fits, with NO residual correlations included, to the  $\Lambda K^-$  (left) with  $\bar{\Lambda} K^+$  (right) data for the centralities 0-10% (top), 10-30% (middle), and 30-50% (bottom). The lines represent the statistical errors, while the boxes represent the systematic errors. Each has unique  $\lambda$  and normalization parameters. The radii are shared amongst like centralities; the scattering parameters ( $\Re f_0$ ,  $\Im f_0$ ,  $d_0$ ) are shared amongst all. The black solid line represents the “raw” fit, i.e. not corrected for momentum resolution effects nor non-flat background. The green line shows the fit to the non-flat background. The purple points show the fit after momentum resolution and non-flat background corrections have been applied. The initial values of the parameters is listed, as well as the final fit values with uncertainties.

Fit Results $\Lambda(\bar{\Lambda})K_S^0$						
System	Centrality	Fit Parameters				
		$\lambda$	$R$	$\mathbb{R}f_0$	$\mathbb{I}f_0$	$d_0$
$\Lambda K_S^0 \& \bar{\Lambda} K_S^0$	0-10%			$2.73 \pm 0.70$ (stat.) $\pm 0.33$ (sys.)		
	10-30%	$0.40 \pm 0.17$ (stat.) $\pm 0.16$ (sys.)	$2.37 \pm 0.62$ (stat.) $\pm 0.23$ (sys.)	$-0.18 \pm 0.04$ (stat.) $\pm 0.16$ (sys.)	$0.12 \pm 0.12$ (stat.) $\pm 0.13$ (sys.)	$-0.19 \pm 4.95$ (stat.) $\pm 0.62$ (sys.)
	30-50%			$1.74 \pm 0.42$ (stat.) $\pm 0.11$ (sys.)		

**Table 5:** Fit Results  $\Lambda(\bar{\Lambda})K_S^0$ , with no residual correlations included. Each pair is fit simultaneously with its conjugate (ie.  $\Lambda K_S^0$  with  $\bar{\Lambda} K_S^0$ ) across all centralities (0-10%, 10-30%, 30-50%), for a total of 6 simultaneous analyses in the fit. A single  $\lambda$  parameter is shared amongst all. Each analysis has a unique normalization parameter. The radii are shared between analyses of like centrality, as these should have similar source sizes. The scattering parameters ( $\mathbb{R}f_0$ ,  $\mathbb{I}f_0$ ,  $d_0$ ) are shared amongst all. The background is modeled by a (6<sup>th</sup>-)degree polynomial fit to THERMINATOR simulation. The fit is done on the data with only statistical error bars. The errors marked as “stat.” are those returned by MINUIT. The errors marked as “sys.” are those which result from my systematic analysis (as outlined in Section 6).

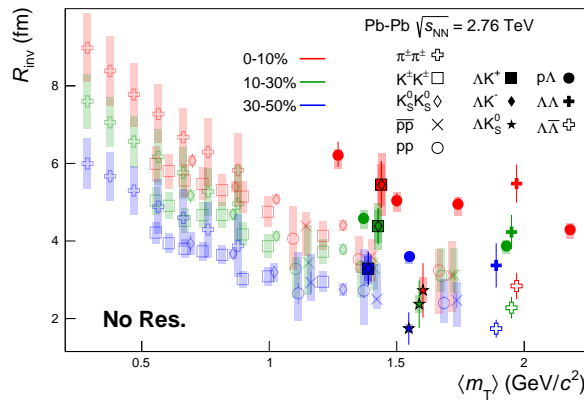
Fit Results $\Lambda(\bar{\Lambda})K^\pm$						
System	Centrality	Fit Parameters				
		$\lambda$	$R$	$\mathbb{R}f_0$	$\mathbb{I}f_0$	$d_0$
$\Lambda K^+ \& \bar{\Lambda} K^-$	0-10%	$0.61 \pm 0.14$ (stat.) $\pm 0.28$ (sys.)	$5.45 \pm 0.60$ (stat.) $\pm 0.54$ (sys.)	$-0.59 \pm 0.12$ (stat.) $\pm 0.36$ (sys.)	$0.49 \pm 0.12$ (stat.) $\pm 0.23$ (sys.)	$0.86 \pm 0.45$ (stat.) $\pm 0.53$ (sys.)
	10-30%	$0.49 \pm 0.11$ (stat.) $\pm 0.36$ (sys.)	$4.38 \pm 0.46$ (stat.) $\pm 0.42$ (sys.)			
$\Lambda K^+ \& \bar{\Lambda} K^-$	30-50%	$0.44 \pm 0.12$ (stat.) $\pm 0.31$ (sys.)	$3.29 \pm 0.43$ (stat.) $\pm 0.32$ (sys.)	$0.25 \pm 0.10$ (stat.) $\pm 0.14$ (sys.)	$0.45 \pm 0.10$ (stat.) $\pm 0.11$ (sys.)	$-4.47 \pm 1.65$ (stat.) $\pm 1.33$ (sys.)

**Table 6:** Fit Results  $\Lambda(\bar{\Lambda})K^\pm$ , with no residual correlations included. All  $\Lambda K^\pm$  analyses are fit simultaneously across all centralities (0-10%, 10-30%, 30-50%). Scattering parameters ( $\mathbb{R}f_0$ ,  $\mathbb{I}f_0$ ,  $d_0$ ) are shared between pair-conjugate systems (i.e. a parameter set describing the  $\Lambda K^+ \& \bar{\Lambda} K^-$  system, and a separate set describing the  $\Lambda K^- \& \bar{\Lambda} K^+$  system). For each centrality, a radius and  $\lambda$  parameters are shared between all pairs ( $\Lambda K^+, \bar{\Lambda} K^-, \Lambda K^-, \bar{\Lambda} K^+$ ). Each analysis has a unique normalization parameter. The background is modeled by a (6<sup>th</sup>-)degree polynomial fit to THERMINATOR simulation. The fit is done on the data with only statistical error bars. The errors marked as “stat.” are those returned by MINUIT. The errors marked as “sys.” are those which result from my systematic analysis (as outlined in Section 6).



**Fig. 33:** Extracted scattering parameters for the case of NO residual contributors for all of our AK systems. [Top Left]:  $\text{Im}f_0$  vs.  $\text{Re}f_0$ , together with  $d_0$  to the right. [Top Right (Bottom Left, Bottom Right)]:  $\lambda$  vs. Radius for the 0-10% (10-30%, 30-50%) bin. The green [9] and yellow [10] points show theoretical predictions made using chiral perturbation theory.

766 Figure 34 shows extracted  $R_{\text{inv}}$  parameters as a function of transverse mass ( $m_T$ ) for various pair systems  
 767 over several centralities. The published ALICE data [11] is shown with transparent, open symbols. The  
 768 new AK results are shown with opaque, filled symbols. The radii shown an increasing size with increas-  
 769 ing centrality, as is expected from the simple geometric picture of the collisions. The radii decrease  
 770 in size with increasing  $m_T$ , and we see an approximate scaling of the radii with transverse mass, as is  
 771 expected in the presence of collective flow in the system.



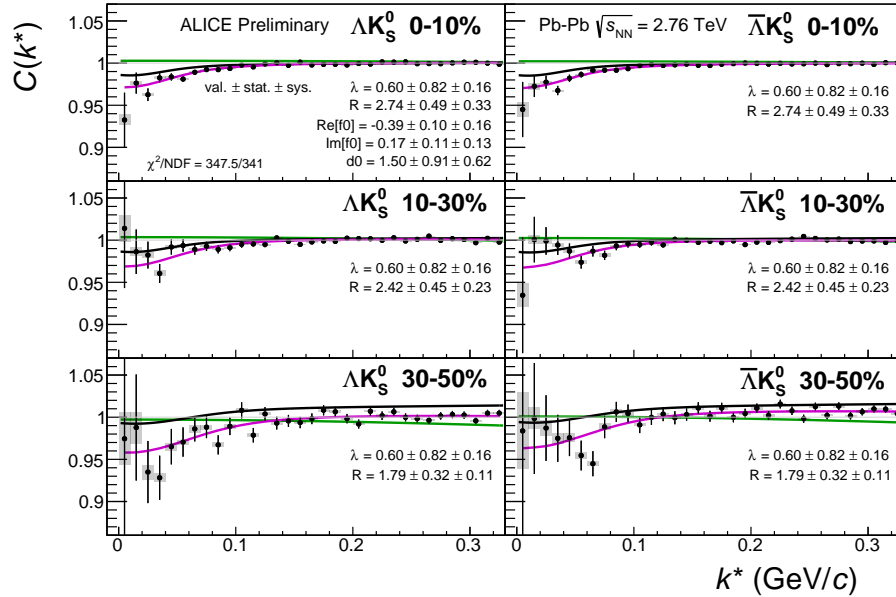
**Fig. 34:** No residual correlations in AK fits. Extracted fit  $R_{\text{inv}}$  parameters as a function of pair transverse mass ( $m_T$ ) for various pair systems over several centralities. The ALICE published data [11] is shown with transparent, open symbols. The new AK results are shown with opaque, filled symbols. In the left, the  $\Lambda K^+$  (with its conjugate pair) results are shown separately from the  $\Lambda K^-$  (with its conjugate pair) results. In the right, all  $\Lambda K^\pm$  results are averaged.

772 **7.1.2 Results:  $\Lambda K_S^0$  and  $\Lambda K^\pm$ : 3 Residual Correlations Included in Fit**

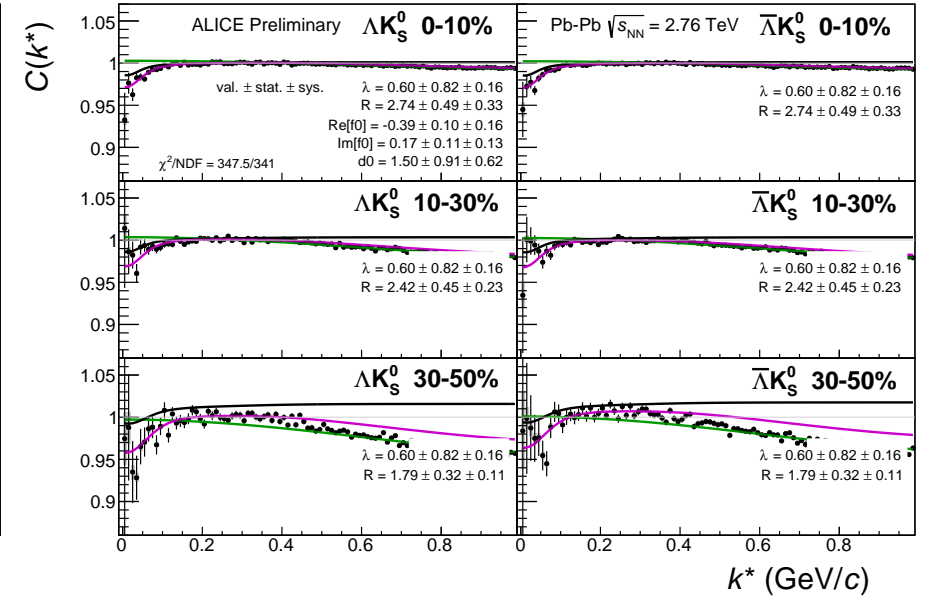
773 Figures 35, 36, and 37 (Section 7) show experimental data with fits for all studied centralities for  $\Lambda K_S^0$   
774 with  $\bar{\Lambda} K_S^0$ ,  $\Lambda K^+$  with  $\bar{\Lambda} K^-$ , and  $\Lambda K^-$  with  $\bar{\Lambda} K^+$ , respectively. The parameter sets extracted from the fits  
775 can be found in Tables 7 and 8. All correlation functions were normalized in the range  $0.32 < k^* < 0.40$   
776 GeV/c, and fit in the range  $0.0 < k^* < 0.30$  GeV/c. For the  $\Lambda K^-$  and  $\bar{\Lambda} K^+$  analyses, the region  $0.19$   
777  $< k^* < 0.23$  GeV/c was excluded from the fit to exclude the bump caused by the  $\Omega^-$  resonance. The  
778 non-flat background was fit with a linear form from  $0.6 < k^* < 0.9$  GeV/c. The theoretical fit function  
779 was then multiplied by this background during the fitting process.

780 In the figures (35, 36, and 37), the black solid line represents the “raw” fit, i.e. not corrected for momen-  
781 tumb resolution effects nor non-flat background. The green line shows the fit to the non-flat background.  
782 The purple points show the fit after momentum resolution and non-flat background corrections have been  
783 applied. The initial values of the parameters is listed, as well as the final fit values with uncertainties.

784 For the  $\Lambda K_S^0$  fits without residuals,  $\lambda$  was restricted to [0.4, 0.6].

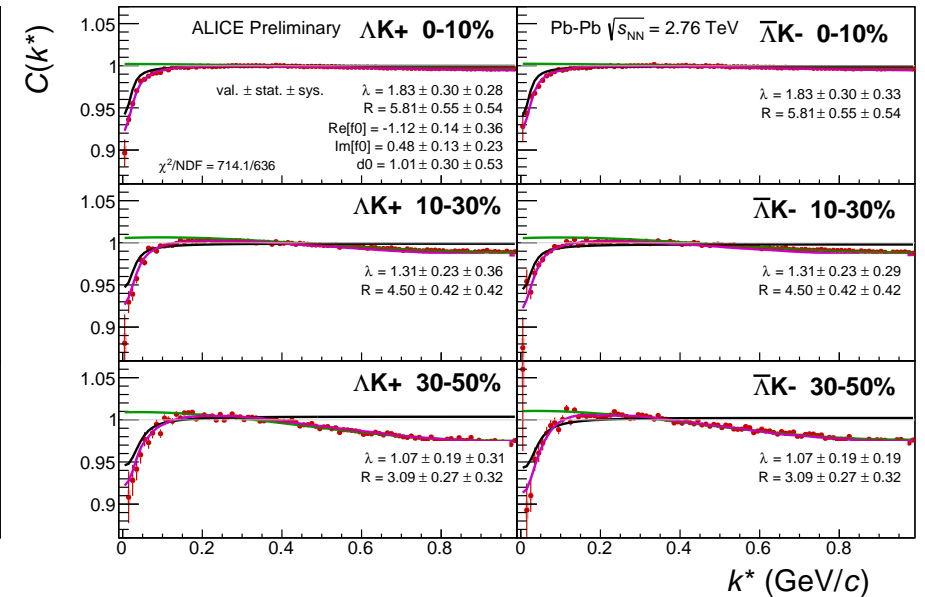
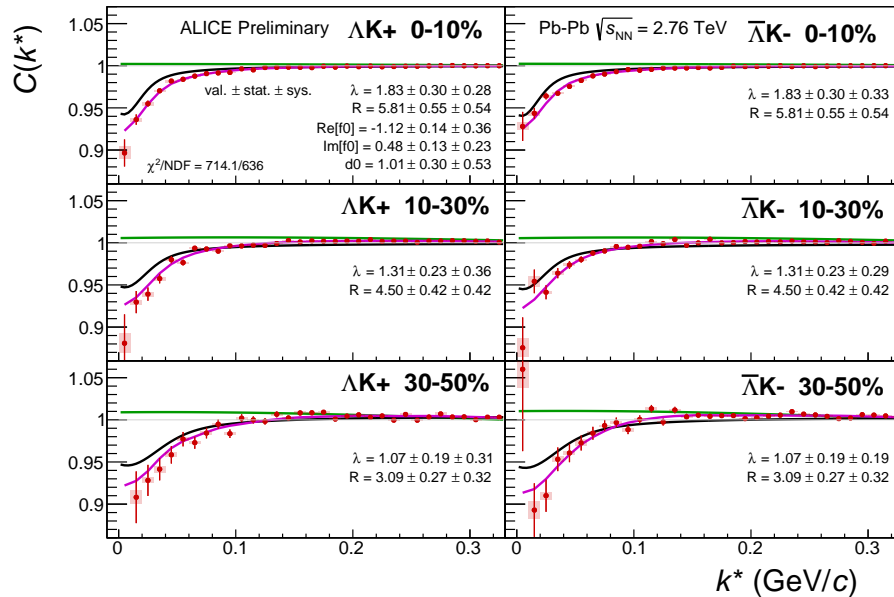


(a) Signal region view ( $k^* \lesssim 0.3$  GeV/c)



(b) Wide view ( $k^* \lesssim 1.0$  GeV/c)

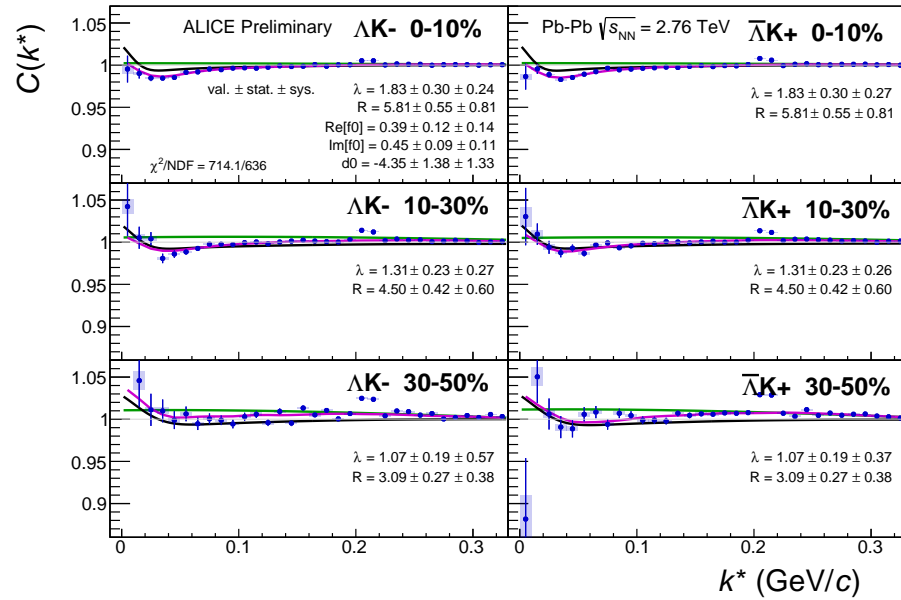
**Fig. 35:** Fits, with 3 residual correlations included, to the  $\Lambda K_S^0$  (left) and  $\bar{\Lambda} K_S^0$  (right) data for the centralities 0-10% (top), 10-30% (middle), and 30-50% (bottom). The lines represent the statistical errors, while the boxes represent the systematic errors. Each has unique  $\lambda$  and normalization parameters. The radii are shared amongst like centralities; the scattering parameters ( $\mathbb{R}f_0, \mathbb{I}f_0, d_0$ ) are shared amongst all. The black solid line represents the “raw” fit, i.e. not corrected for momentum resolution effects nor non-flat background. The green line shows the fit to the non-flat background. The purple points show the fit after momentum resolution and non-flat background corrections have been applied. The initial values of the parameters is listed, as well as the final fit values with uncertainties. Here,  $R$  was restricted to [2.,10.] and  $\lambda$  was restricted to [0.1,0.8].



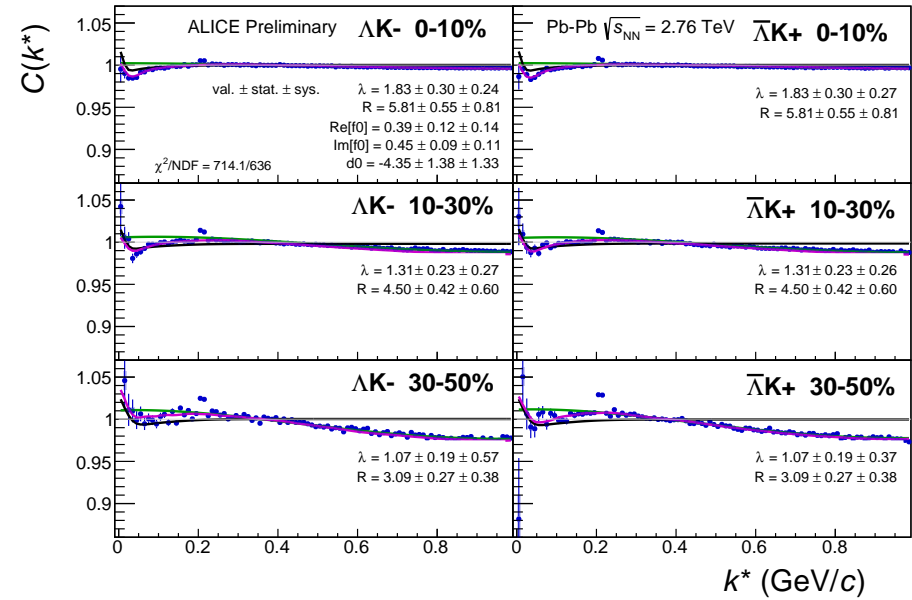
(a) Signal region view ( $k^* \lesssim 0.3 \text{ GeV}/c$ )

(b) Wide view ( $k^* \lesssim 1.0 \text{ GeV}/c$ )

**Fig. 36:** Fits, with 3 residual correlations included, to the  $\Delta K^+$  (left) and  $\Delta K^-$  (right) data for the centralities 0-10% (top), 10-30% (middle), and 30-50% (bottom). The lines represent the statistical errors, while the boxes represent the systematic errors. Each has unique  $\lambda$  and normalization parameters. The radii are shared amongst like centralities; the scattering parameters ( $\text{Re}[f_0], \text{Im}[f_0], d_0$ ) are shared amongst all. The black solid line represents the “raw” fit, i.e. not corrected for momentum resolution effects nor non-flat background. The green line shows the fit to the non-flat background. The purple points show the fit after momentum resolution and non-flat background corrections have been applied. The initial values of the parameters is listed, as well as the final fit values with uncertainties.

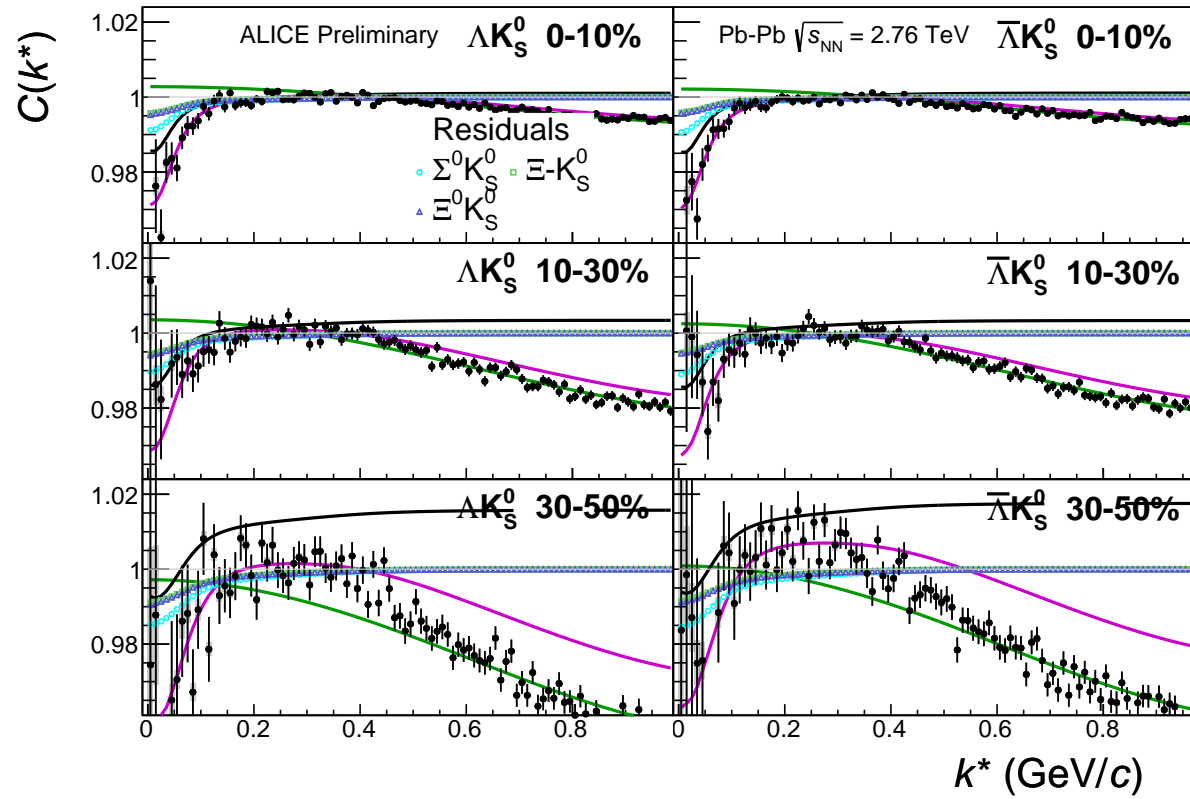


(a) Signal region view ( $k^* \lesssim 0.3 \text{ GeV}/c$ )

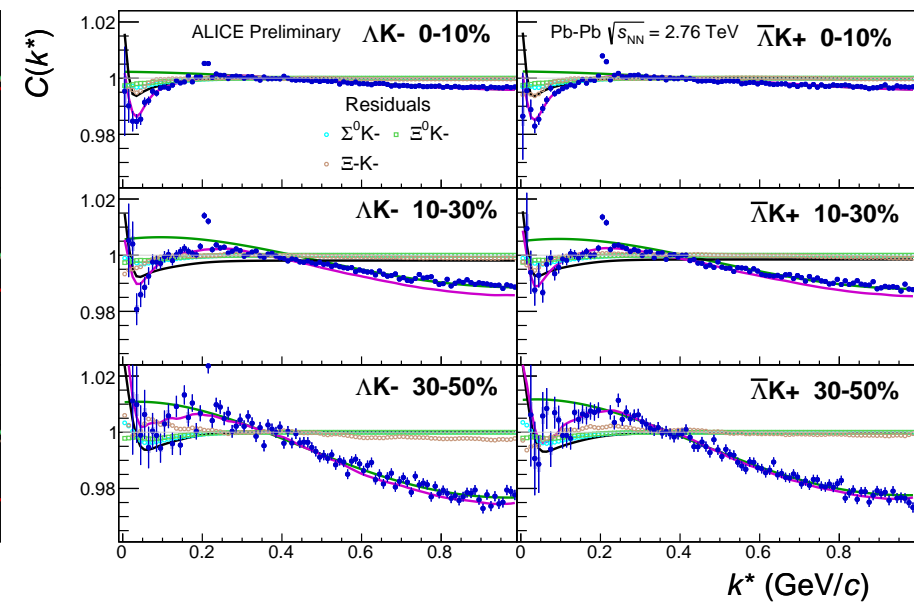
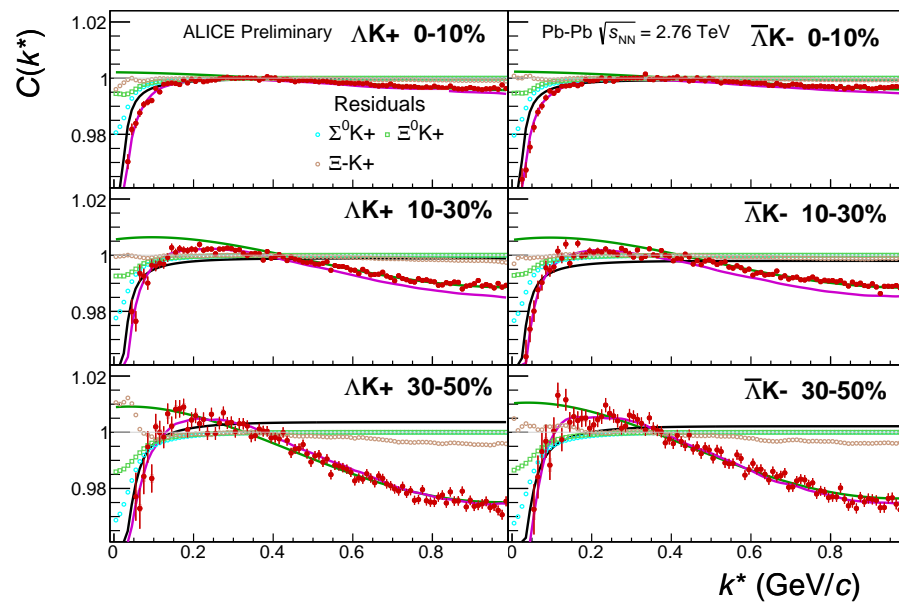


(b) Wide view ( $k^* \lesssim 1.0 \text{ GeV}/c$ )

**Fig. 37:** Fits, with 3 residual correlations included, to the  $\Lambda K^-$  (left) with  $\bar{\Lambda} K^+$  (right) data for the centralities 0-10% (top), 10-30% (middle), and 30-50% (bottom). The lines represent the statistical errors, while the boxes represent the systematic errors. Each has unique  $\lambda$  and normalization parameters. The radii are shared amongst like centralities; the scattering parameters ( $\Re[f_0]$ ,  $\Im[f_0]$ ,  $d_0$ ) are shared amongst all. The black solid line represents the “raw” fit, i.e. not corrected for momentum resolution effects nor non-flat background. The green line shows the fit to the non-flat background. The purple points show the fit after momentum resolution and non-flat background corrections have been applied. The initial values of the parameters is listed, as well as the final fit values with uncertainties.



**Fig. 38:** Fits, with 3 residual correlations included and shown, to the  $\Lambda K_S^0$  (left) and  $\bar{\Lambda} K_S^0$  (right) data for the centralities 0-10% (top), 10-30% (middle), and 30-50% (bottom). The three parent pairs used for the residual correction to the  $\Lambda K_S^0$  ( $\bar{\Lambda} K_S^0$ ) fit are  $\Sigma^0 K_S^0$ ,  $\Xi^0 K_S^0$ , and  $\Xi^- K_S^0$  ( $\bar{\Sigma}^0 K_S^0$ ,  $\bar{\Xi}^0 K_S^0$ , and  $\bar{\Xi}^+ K_S^0$ ).



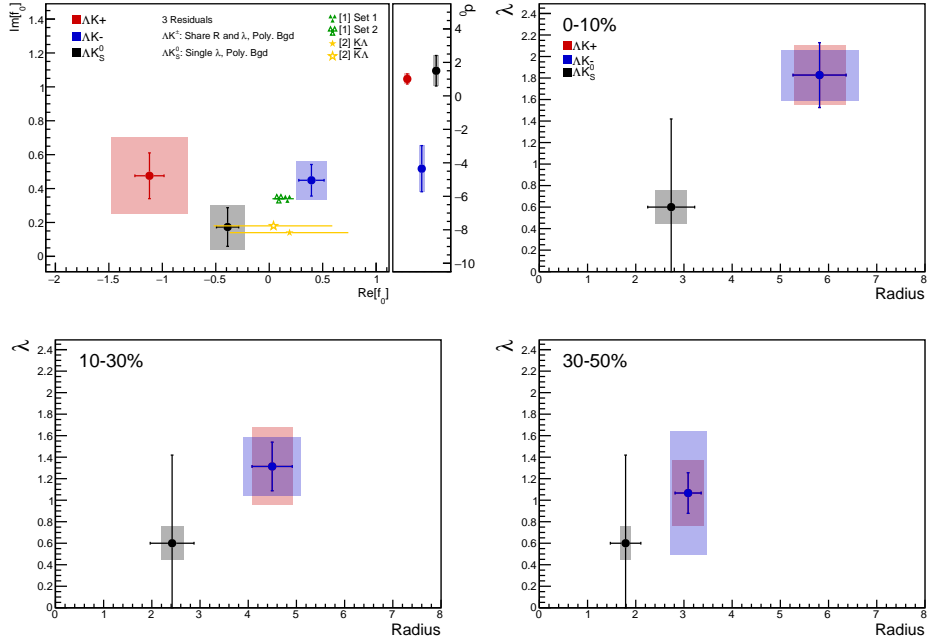
**Fig. 39:** Fits, with 3 residual correlations included and shown, to the  $\Lambda K^+$  &  $\bar{\Lambda} K^-$  (left) and  $\Lambda K^-$  &  $\bar{\Lambda} K^+$  (right) data for the centralities 0-10% (top), 10-30% (middle), and 30-50% (bottom). The three parent pairs used for the residual correction to the  $\Lambda K^+(\bar{\Lambda} K^-)$  fit are  $\Sigma^0 K^+$ ,  $\Xi^0 K^+$ , and  $\Xi^- K^+$  ( $\bar{\Sigma}^0 K^-$ ,  $\bar{\Xi}^0 K^-$ , and  $\bar{\Xi}^- K^-$ ).

Fit Results $\Lambda(\bar{\Lambda})K_S^0$						
System	Centrality	Fit Parameters				
		$\lambda$	$R$	$\mathbb{R}f_0$	$\mathbb{I}f_0$	$d_0$
$\Lambda K_S^0 \& \bar{\Lambda} K_S^0$	0-10%			$2.74 \pm 0.49$ (stat.) $\pm 0.33$ (sys.)		
	10-30%	$0.60 \pm 0.82$ (stat.) $\pm 0.16$ (sys.)	$2.42 \pm 0.45$ (stat.) $\pm 0.23$ (sys.)	$-0.39 \pm 0.10$ (stat.) $\pm 0.16$ (sys.)	$0.17 \pm 0.11$ (stat.) $\pm 0.13$ (sys.)	$1.50 \pm 0.91$ (stat.) $\pm 0.62$ (sys.)
	30-50%			$1.79 \pm 0.32$ (stat.) $\pm 0.11$ (sys.)		

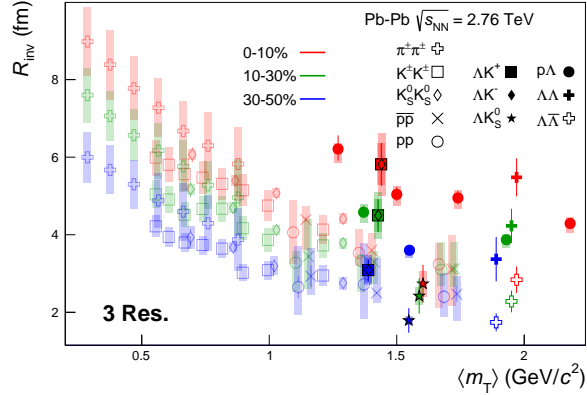
**Table 7:** Fit Results  $\Lambda(\bar{\Lambda})K_S^0$ , with 3 residual correlations included. Each pair is fit simultaneously with its conjugate (ie.  $\Lambda K_S^0$  with  $\bar{\Lambda} K_S^0$ ) across all centralities (0-10%, 10-30%, 30-50%), for a total of 6 simultaneous analyses in the fit. A single  $\lambda$  parameter is shared amongst all. Each analysis has a unique normalization parameter. The radii are shared between analyses of like centrality, as these should have similar source sizes. The scattering parameters ( $\mathbb{R}f_0$ ,  $\mathbb{I}f_0$ ,  $d_0$ ) are shared amongst all. The background is modeled by a (6<sup>th</sup>-)degree polynomial fit to THERMINATOR simulation. The fit is done on the data with only statistical error bars. The errors marked as “stat.” are those returned by MINUIT. The errors marked as “sys.” are those which result from my systematic analysis (as outlined in Section 6).

Fit Results $\Lambda(\bar{\Lambda})K^\pm$						
System	Centrality	Fit Parameters				
		$\lambda$	$R$	$\mathbb{R}f_0$	$\mathbb{I}f_0$	$d_0$
$\Lambda K^+ \& \bar{\Lambda} K^-$	0-10%	$1.83 \pm 0.30$ (stat.) $\pm 0.28$ (sys.)	$5.81 \pm 0.55$ (stat.) $\pm 0.54$ (sys.)			
	10-30%	$1.31 \pm 0.23$ (stat.) $\pm 0.36$ (sys.)	$4.50 \pm 0.42$ (stat.) $\pm 0.42$ (sys.)	$-1.12 \pm 0.14$ (stat.) $\pm 0.36$ (sys.)	$0.48 \pm 0.13$ (stat.) $\pm 0.23$ (sys.)	$1.01 \pm 0.30$ (stat.) $\pm 0.53$ (sys.)
$\Lambda K^+ \& \bar{\Lambda} K^+$	30-50%	$1.07 \pm 0.19$ (stat.) $\pm 0.31$ (sys.)	$3.09 \pm 0.27$ (stat.) $\pm 0.32$ (sys.)	$0.39 \pm 0.12$ (stat.) $\pm 0.14$ (sys.)	$0.45 \pm 0.09$ (stat.) $\pm 0.11$ (sys.)	$-4.35 \pm 1.38$ (stat.) $\pm 1.33$ (sys.)

**Table 8:** Fit Results  $\Lambda(\bar{\Lambda})K^\pm$ , with 3 residual correlations included. All  $\Lambda K^\pm$  analyses are fit simultaneously across all centralities (0-10%, 10-30%, 30-50%). Scattering parameters ( $\mathbb{R}f_0$ ,  $\mathbb{I}f_0$ ,  $d_0$ ) are shared between pair-conjugate systems (i.e. a parameter set describing the  $\Lambda K^+ \& \bar{\Lambda} K^-$  system, and a separate set describing the  $\Lambda K^- \& \bar{\Lambda} K^+$  system). For each centrality, a radius and  $\lambda$  parameters are shared between all pairs ( $\Lambda K^+, \bar{\Lambda} K^-, \Lambda K^-, \bar{\Lambda} K^+$ ). Each analysis has a unique normalization parameter. The background is modeled by a (6<sup>th</sup>-)degree polynomial fit to THERMINATOR simulation. The fit is done on the data with only statistical error bars. The errors marked as “stat.” are those returned by MINUIT. The errors marked as “sys.” are those which result from my systematic analysis (as outlined in Section 6).



**Fig. 40:** Extracted scattering parameters for the case of 3 residual contributors for all of our  $\Lambda K$  systems. [Top Left]:  $\text{Im}f_0$  vs.  $\text{Re}f_0$ , together with  $d_0$  to the right. [Top Right (Bottom Left, Bottom Right)]:  $\lambda$  vs. Radius for the 0-10% (10-30%, 30-50%) bin. The green [9] and yellow [10] points show theoretical predictions made using chiral perturbation theory.



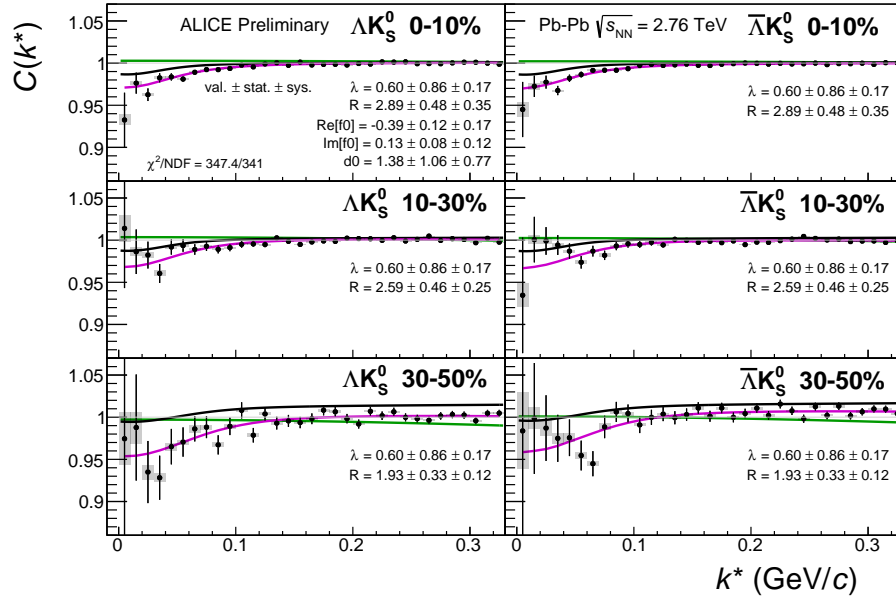
**Fig. 41:** 3 residual correlations in  $\Lambda K$  fits. Extracted fit  $R_{\text{inv}}$  parameters as a function of pair transverse mass ( $m_T$ ) for various pair systems over several centralities. The ALICE published data [11] is shown with transparent, open symbols. The new  $\Lambda K$  results are shown with opaque, filled symbols. In the left, the  $\Lambda K^+$  (with its conjugate pair) results are shown separately from the  $\Lambda K^-$  (with its conjugate pair) results. In the right, all  $\Lambda K^\pm$  results are averaged.

785 **7.1.3 Results:  $\Lambda K_S^0$  and  $\Lambda K^\pm$ : 10 Residual Correlations Included in Fit**

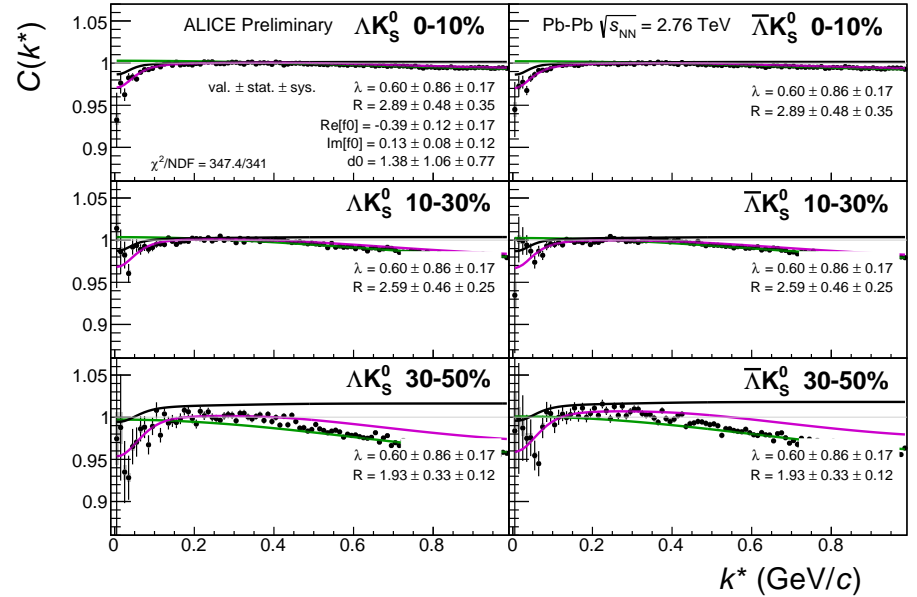
786 Figures 42, 43, and 44 (Section 7) show experimental data with fits for all studied centralities for  $\Lambda K_S^0$   
787 with  $\bar{\Lambda} K_S^0$ ,  $\Lambda K^+$  with  $\bar{\Lambda} K^-$ , and  $\Lambda K^-$  with  $\bar{\Lambda} K^+$ , respectively. The parameter sets extracted from the fits  
788 can be found in Tables 9 and 10. All correlation functions were normalized in the range  $0.32 < k^* <$   
789  $0.40 \text{ GeV}/c$ , and fit in the range  $0.0 < k^* < 0.30 \text{ GeV}/c$ . For the  $\Lambda K^-$  and  $\bar{\Lambda} K^+$  analyses, the region  $0.19$   
790  $< k^* < 0.23 \text{ GeV}/c$  was excluded from the fit to exclude the bump caused by the  $\Omega^-$  resonance. The  
791 non-flat background was fit with a linear form from  $0.6 < k^* < 0.9 \text{ GeV}/c$ . The theoretical fit function  
792 was then multiplied by this background during the fitting process.

793 In the figures (42, 43, and 44), the black solid line represents the “raw” fit, i.e. not corrected for momen-  
794 tum resolution effects nor non-flat background. The green line shows the fit to the non-flat background.  
795 The purple points show the fit after momentum resolution and non-flat background corrections have been  
796 applied. The initial values of the parameters is listed, as well as the final fit values with uncertainties.

797 For the  $\Lambda K_S^0$  fits without residuals,  $\lambda$  was restricted to [0.4, 0.6].

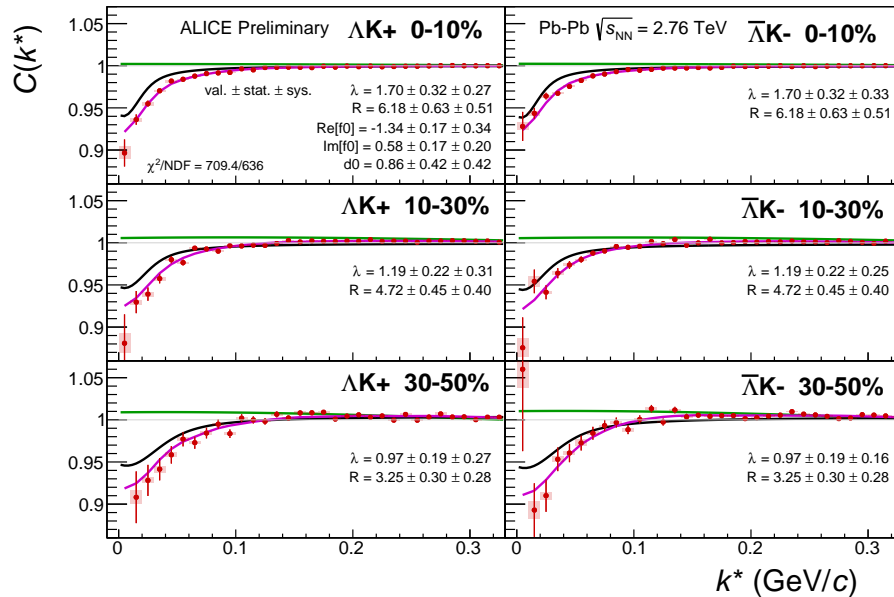


(a) Signal region view ( $k^* \lesssim 0.3$  GeV/c)

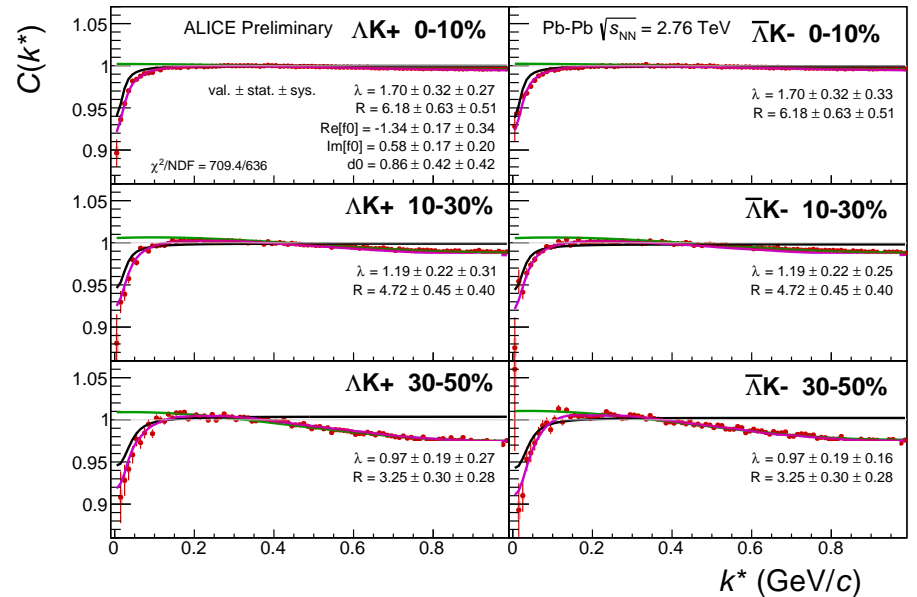


(b) Wide view ( $k^* \lesssim 1.0$  GeV/c)

**Fig. 42:** Fits, with 10 residual correlations included, to the  $\Lambda K_S^0$  (left) and  $\bar{\Lambda} K_S^0$  (right) data for the centralities 0-10% (top), 10-30% (middle), and 30-50% (bottom). The lines represent the statistical errors, while the boxes represent the systematic errors. Each has unique  $\lambda$  and normalization parameters. The radii are shared amongst like centralities; the scattering parameters ( $\mathbb{R} f_0, \mathbb{I} f_0, d_0$ ) are shared amongst all. The black solid line represents the “raw” fit, i.e. not corrected for momentum resolution effects nor non-flat background. The green line shows the fit to the non-flat background. The purple points show the fit after momentum resolution and non-flat background corrections have been applied. The initial values of the parameters is listed, as well as the final fit values with uncertainties. Here,  $R$  was restricted to [2.,10.] and  $\Lambda$  was restricted to [0.1,0.8].

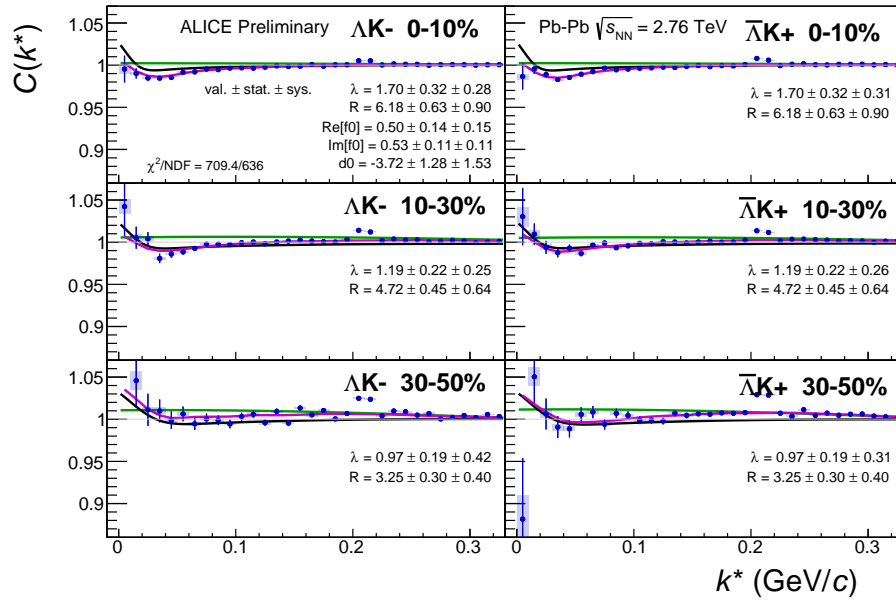


(a) Signal region view ( $k^* \lesssim 0.3 \text{ GeV}/c$ )

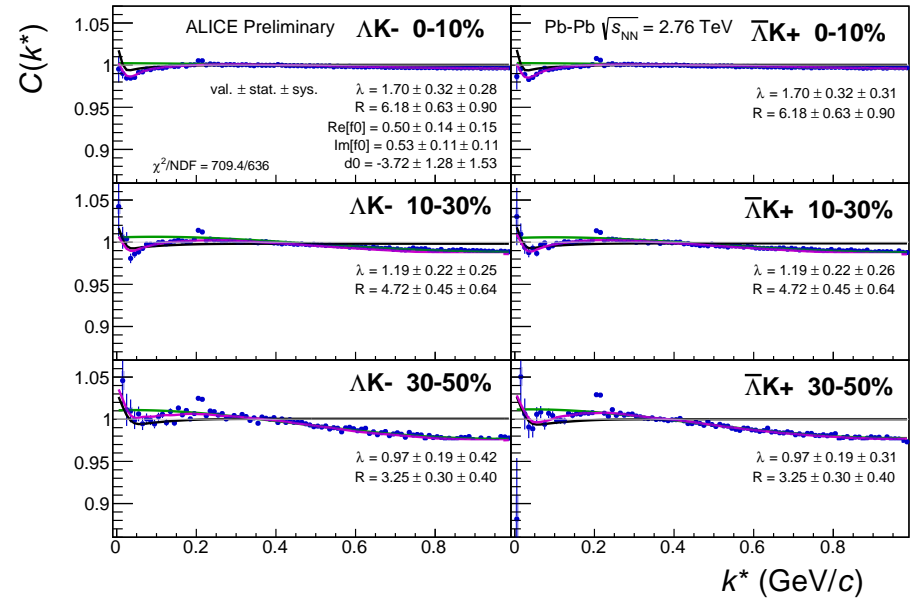


(b) Wide view ( $k^* \lesssim 1.0 \text{ GeV}/c$ )

**Fig. 43:** Fits, with 10 residual correlations included, to the  $\Lambda K^+$  (left) and  $\bar{\Lambda} K^-$  (right) data for the centralities 0-10% (top), 10-30% (middle), and 30-50% (bottom). The lines represent the statistical errors, while the boxes represent the systematic errors. Each has unique  $\lambda$  and normalization parameters. The radii are shared amongst like centralities; the scattering parameters ( $Re[f_0]$ ,  $Im[f_0]$ ,  $d_0$ ) are shared amongst all. The black solid line represents the “raw” fit, i.e. not corrected for momentum resolution effects nor non-flat background. The green line shows the fit to the non-flat background. The purple points show the fit after momentum resolution and non-flat background corrections have been applied. The initial values of the parameters is listed, as well as the final fit values with uncertainties.

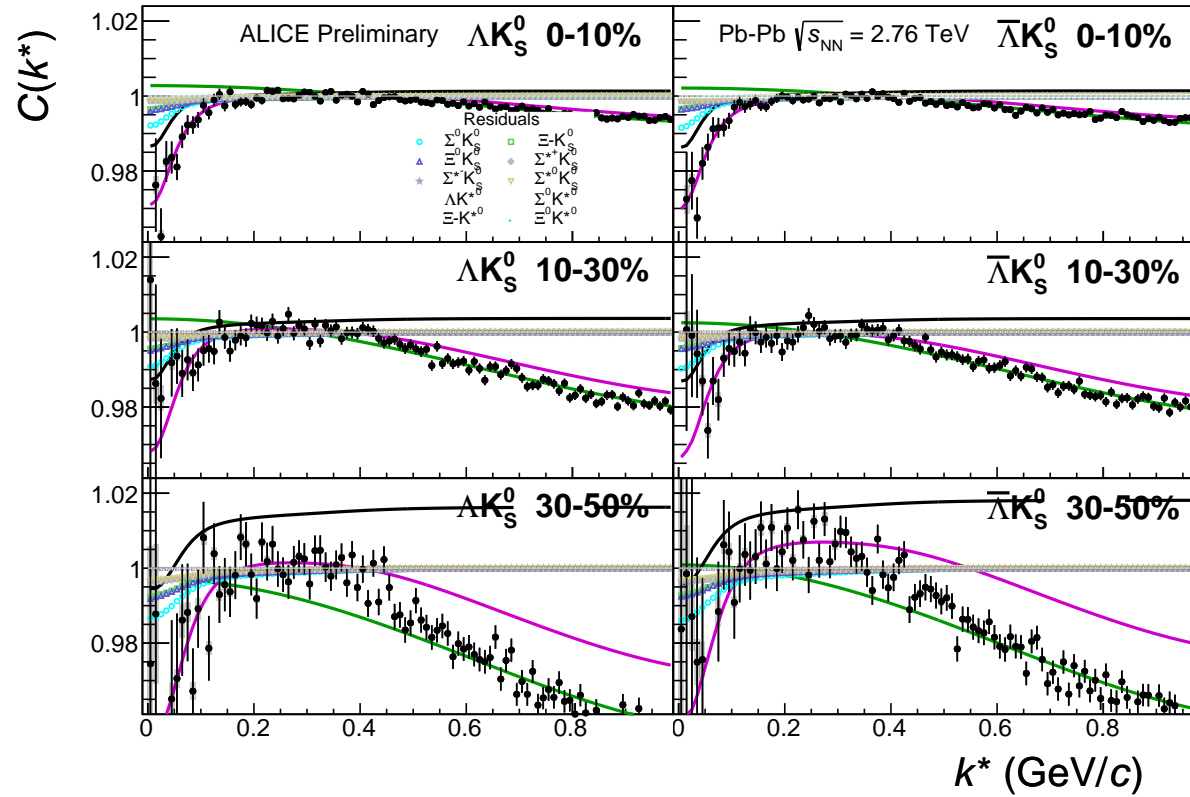


(a) Signal region view ( $k^* \lesssim 0.3 \text{ GeV}/c$ )

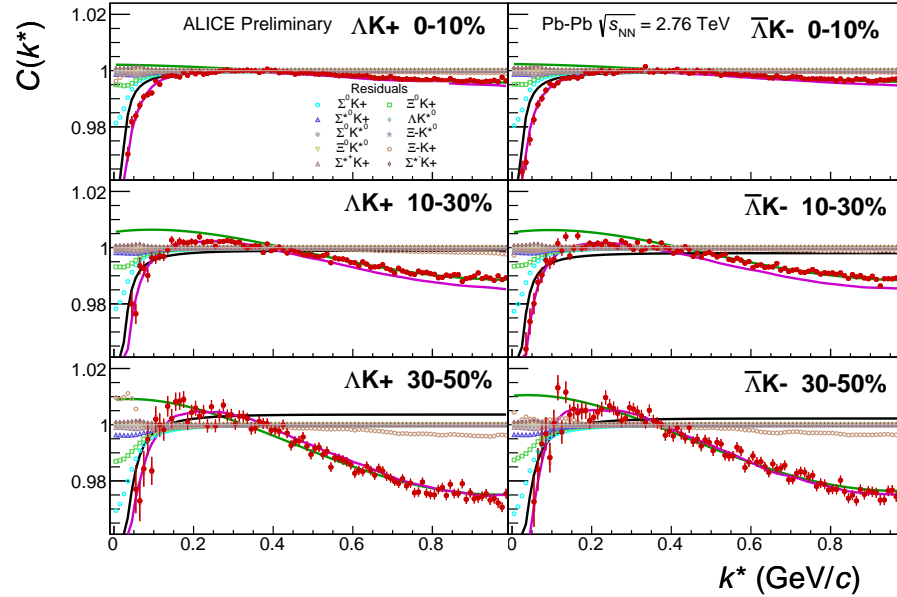


(b) Wide view ( $k^* \lesssim 1.0 \text{ GeV}/c$ )

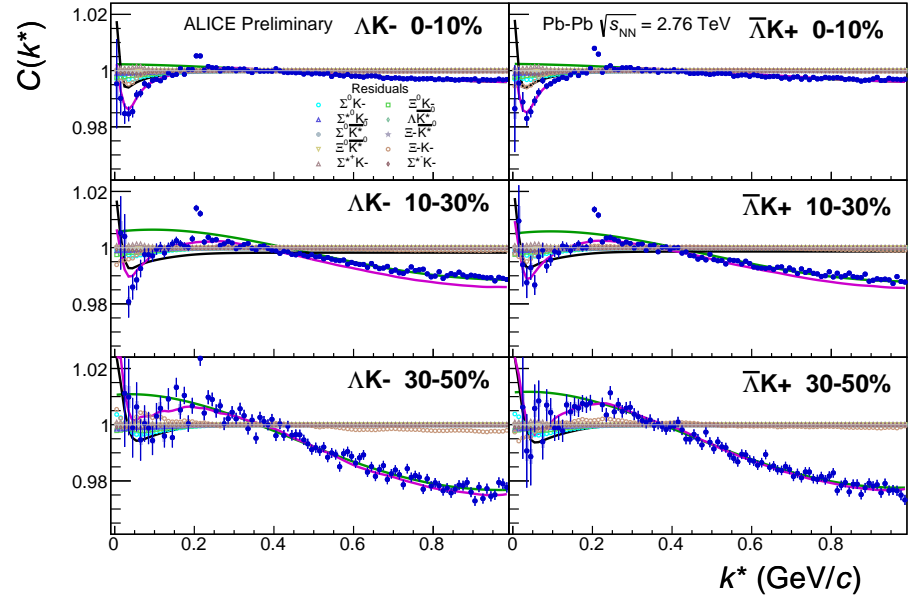
**Fig. 44:** Fits, with 10 residual correlations included, to the  $\Lambda K^-$  (left) with  $\bar{\Lambda} K^+$  (right) data for the centralities 0-10% (top), 10-30% (middle), and 30-50% (bottom). The lines represent the statistical errors, while the boxes represent the systematic errors. Each has unique  $\lambda$  and normalization parameters. The radii are shared amongst like centralities; the scattering parameters ( $\text{Re}[f_0]$ ,  $\text{Im}[f_0]$ ,  $d_0$ ) are shared amongst all. The black solid line represents the “raw” fit, i.e. not corrected for momentum resolution effects nor non-flat background. The green line shows the fit to the non-flat background. The purple points show the fit after momentum resolution and non-flat background corrections have been applied. The initial values of the parameters is listed, as well as the final fit values with uncertainties.



**Fig. 45:** Fits, with 10 residual correlations included and shown, to the  $\Lambda K_S^0$  (left) and  $\bar{\Lambda} K_S^0$  (right) data for the centralities 0-10% (top), 10-30% (middle), and 30-50% (bottom). The ten parent pairs used for the residual correction to the  $\Lambda K_S^0$  ( $\bar{\Lambda} K_S^0$ ) fit are  $\Sigma^0 K_S^0$ ,  $\Xi^0 K_S^0$ ,  $\Xi^- K_S^0$ ,  $\Sigma^{(+,-,0)} K_S^0$ ,  $\Lambda K^{*0}$ ,  $\Sigma^0 K^{*0}$ ,  $\Xi^0 K^{*0}$ , and  $\Xi^- K^{*0}$  ( $\bar{\Sigma}^0 K_S^0$ ,  $\bar{\Xi}^0 K_S^0$ ,  $\bar{\Xi}^+ K_S^0$ ,  $\bar{\Sigma}^{(+,-,0)} K_S^0$ ,  $\bar{\Lambda} K^{*0}$ ,  $\bar{\Sigma}^0 \bar{K}^{*0}$ ,  $\bar{\Xi}^0 \bar{K}^{*0}$ , and  $\bar{\Xi}^+ \bar{K}^{*0}$ ).



(a)  $\Lambda K^+(\bar{\Lambda} K^-)$  fits with residual contributions shown for the centralities 0-10% (top), 10-30% (middle), and 30-50% (bottom)



(b)  $\Lambda K^-(\bar{\Lambda} K^+)$  fits with residual contributions shown for the centralities 0-10% (top), 10-30% (middle), and 30-50% (bottom)

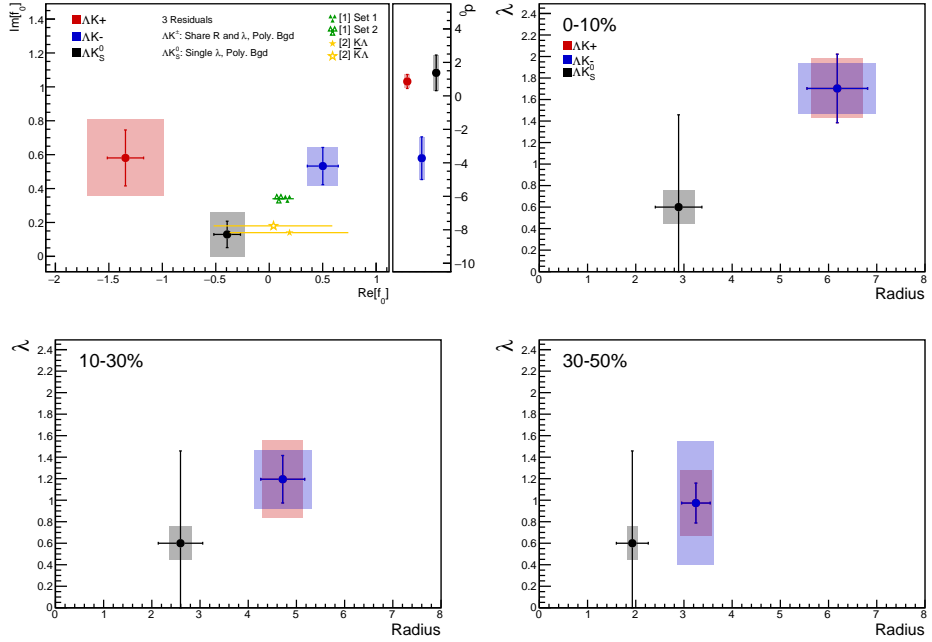
**Fig. 46:** Fits, with 10 residual correlations included and shown, to the  $\Lambda K^+$  &  $\bar{\Lambda} K^-$  (left) and  $\Lambda K^-$  &  $\bar{\Lambda} K^+$  (right) data for the centralities 0-10% (top), 10-30% (middle), and 30-50% (bottom). The ten parent pairs used for the residual correction to the  $\Lambda K^+$  ( $\bar{\Lambda} K^-$ ) fit are  $\Sigma^0 K^+$ ,  $\Xi^0 K^+$ ,  $\Xi^- K^+$ ,  $\Sigma^{*(+,-,0)} K^+$ ,  $\Lambda K^{*0}$ ,  $\Sigma^0 K^{*0}$ ,  $\Xi^0 K^{*0}$ , and  $\Xi^- K^{*0}$  ( $\bar{\Sigma}^0 K^-$ ,  $\bar{\Xi}^0 K^-$ ,  $\bar{\Xi}^+ K^-$ ,  $\bar{\Sigma}^{*(+,-,0)} K^-$ ,  $\bar{\Lambda} \bar{K}^{*0}$ ,  $\bar{\Sigma}^0 \bar{K}^{*0}$ ,  $\bar{\Xi}^0 \bar{K}^{*0}$ , and  $\bar{\Xi}^+ \bar{K}^{*0}$ ).

Fit Results $\Lambda(\bar{\Lambda})K_S^0$						
System	Centrality	Fit Parameters				
		$\lambda$	$R$	$\mathbb{R}f_0$	$\mathbb{I}f_0$	$d_0$
$\Lambda K_S^0 \& \bar{\Lambda} K_S^0$	0-10%					
	10-30%	$0.60 \pm 0.86$ (stat.) $\pm 0.16$ (sys.)	$2.89 \pm 0.48$ (stat.) $\pm 0.33$ (sys.)	$2.59 \pm 0.46$ (stat.) $\pm 0.23$ (sys.)	$-0.39 \pm 0.12$ (stat.) $\pm 0.16$ (sys.)	$0.13 \pm 0.08$ (stat.) $\pm 0.13$ (sys.)
	30-50%			$1.93 \pm 0.33$ (stat.) $\pm 0.11$ (sys.)		$1.38 \pm 1.06$ (stat.) $\pm 0.62$ (sys.)

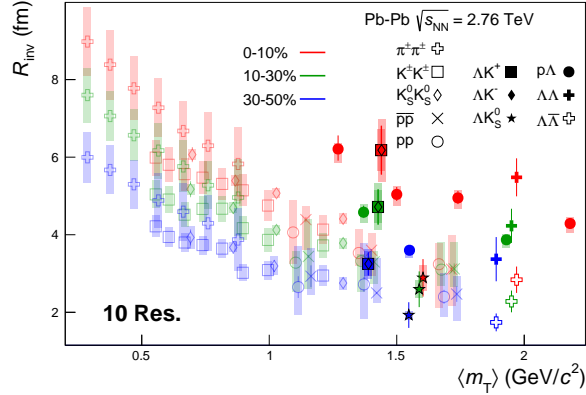
**Table 9:** Fit Results  $\Lambda(\bar{\Lambda})K_S^0$ , with 10 residual correlations included. Each pair is fit simultaneously with its conjugate (ie.  $\Lambda K_S^0$  with  $\bar{\Lambda} K_S^0$ ) across all centralities (0-10%, 10-30%, 30-50%), for a total of 6 simultaneous analyses in the fit. A single  $\lambda$  parameter is shared amongst all. Each analysis has a unique normalization parameter. The radii are shared between analyses of like centrality, as these should have similar source sizes. The scattering parameters ( $\mathbb{R}f_0$ ,  $\mathbb{I}f_0$ ,  $d_0$ ) are shared amongst all. The background is modeled by a (6<sup>th</sup>-)degree polynomial fit to THERMINATOR simulation. The fit is done on the data with only statistical error bars. The errors marked as “stat.” are those returned by MINUIT. The errors marked as “sys.” are those which result from my systematic analysis (as outlined in Section 6).

Fit Results $\Lambda(\bar{\Lambda})K^\pm$						
System	Centrality	Fit Parameters				
		$\lambda$	$R$	$\mathbb{R}f_0$	$\mathbb{I}f_0$	$d_0$
$\Lambda K^+ \& \bar{\Lambda} K^-$	0-10%	$1.70 \pm 0.32$ (stat.) $\pm 0.28$ (sys.)	$6.18 \pm 0.63$ (stat.) $\pm 0.54$ (sys.)	$-1.34 \pm 0.17$ (stat.) $\pm 0.36$ (sys.)	$0.58 \pm 0.17$ (stat.) $\pm 0.23$ (sys.)	$0.86 \pm 0.42$ (stat.) $\pm 0.53$ (sys.)
	10-30%	$1.19 \pm 0.22$ (stat.) $\pm 0.36$ (sys.)	$4.72 \pm 0.45$ (stat.) $\pm 0.42$ (sys.)			
$\Lambda K^+ \& \bar{\Lambda} K^+$	30-50%	$0.97 \pm 0.19$ (stat.) $\pm 0.31$ (sys.)	$3.25 \pm 0.30$ (stat.) $\pm 0.32$ (sys.)	$0.50 \pm 0.14$ (stat.) $\pm 0.14$ (sys.)	$0.53 \pm 0.11$ (stat.) $\pm 0.11$ (sys.)	$-3.72 \pm 1.28$ (stat.) $\pm 1.33$ (sys.)

**Table 10:** Fit Results  $\Lambda(\bar{\Lambda})K^\pm$ , with 10 residual correlations included. All  $\Lambda K^\pm$  analyses are fit simultaneously across all centralities (0-10%, 10-30%, 30-50%). Scattering parameters ( $\mathbb{R}f_0$ ,  $\mathbb{I}f_0$ ,  $d_0$ ) are shared between pair-conjugate systems (i.e. a parameter set describing the  $\Lambda K^+ \& \bar{\Lambda} K^-$  system, and a separate set describing the  $\Lambda K^- \& \bar{\Lambda} K^+$  system). For each centrality, a radius and  $\lambda$  parameters are shared between all pairs ( $\Lambda K^+, \bar{\Lambda} K^-, \Lambda K^-, \bar{\Lambda} K^+$ ). Each analysis has a unique normalization parameter. The background is modeled by a (6<sup>th</sup>-)degree polynomial fit to THERMINATOR simulation. The fit is done on the data with only statistical error bars. The errors marked as “stat.” are those returned by MINUIT. The errors marked as “sys.” are those which result from my systematic analysis (as outlined in Section 6).



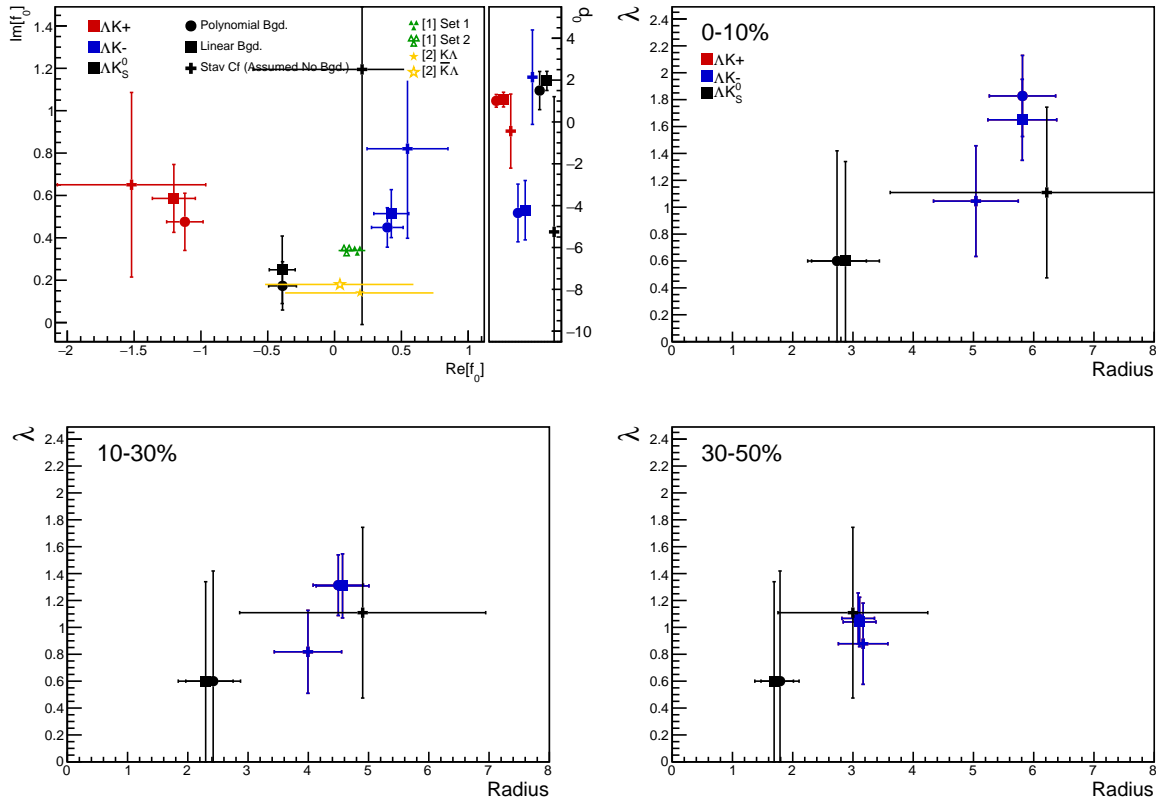
**Fig. 47:** Extracted scattering parameters for the case of 10 residual contributors for all of our  $\Lambda K$  systems. [Top Left]:  $\text{Im}f_0$  vs.  $\text{Re}f_0$ , together with  $d_0$  to the right. [Top Right (Bottom Left, Bottom Right)]:  $\lambda$  vs. Radius for the 0-10% (10-30%, 30-50%) bin. The green [9] and yellow [10] points show theoretical predictions made using chiral perturbation theory.



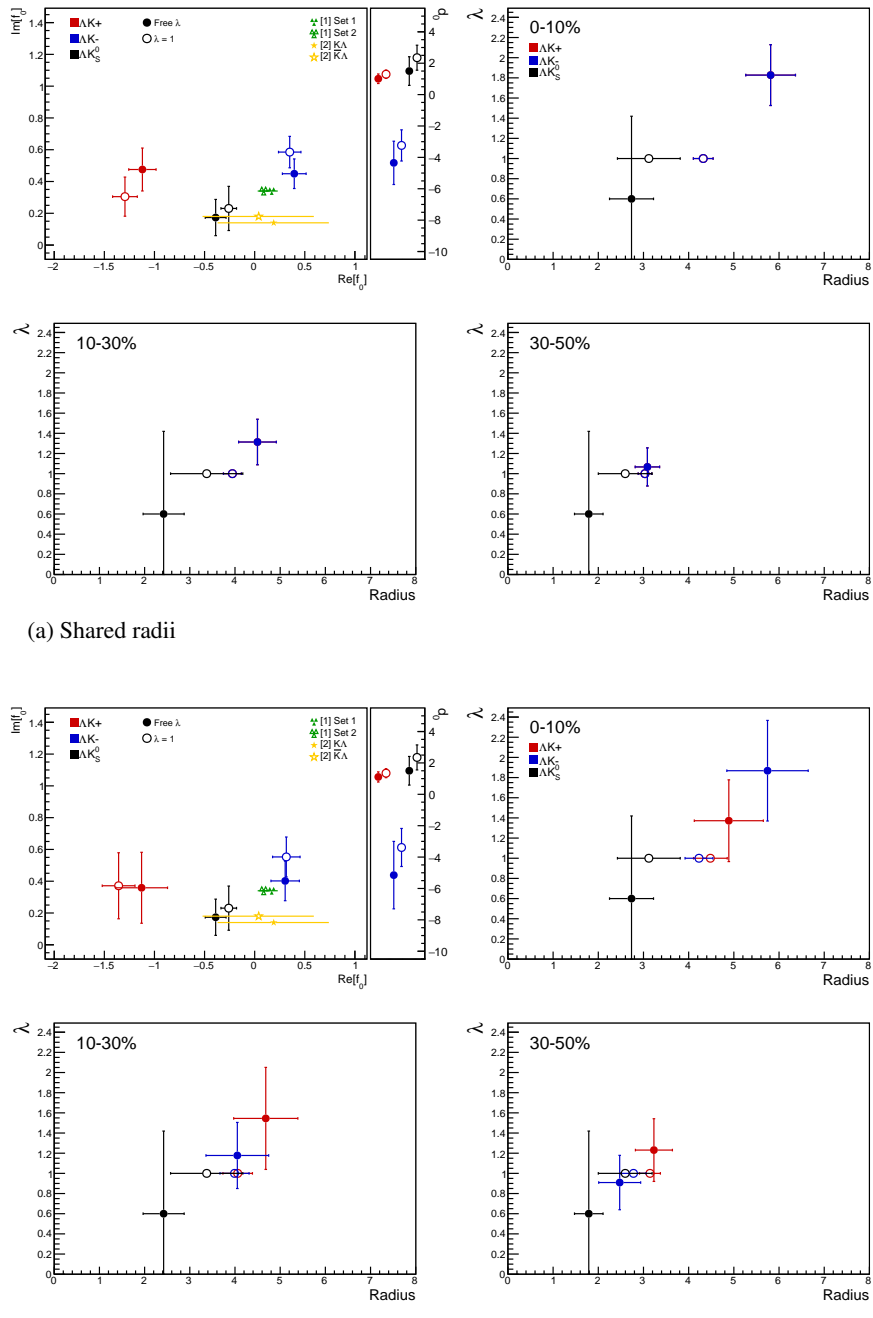
**Fig. 48:** 10 residual correlations in  $\Lambda K$  fits. Extracted fit  $R_{\text{inv}}$  parameters as a function of pair transverse mass ( $m_T$ ) for various pair systems over several centralities. The ALICE published data [11] is shown with transparent, open symbols. The new  $\Lambda K$  results are shown with opaque, filled symbols. In the left, the  $\Lambda K^+$  (with its conjugate pair) results are shown separately from the  $\Lambda K^-$  (with its conjugate pair) results. In the right, all  $\Lambda K^\pm$  results are averaged.

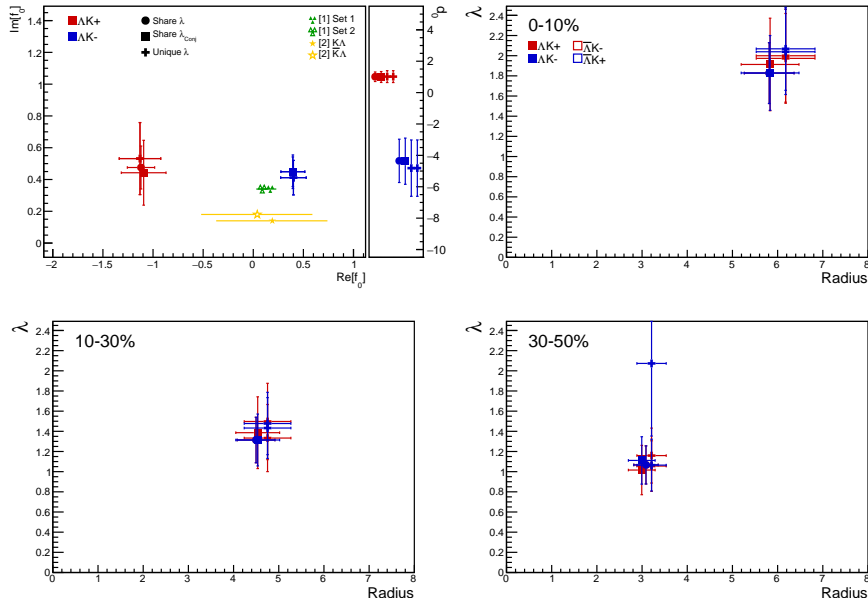
### 798 7.1.4 Results: $\Lambda K_S^0$ and $\Lambda K^\pm$ : Fit Method Comparisons

799 In Figure 49, we show extracted fit parameters for the case of  $\Lambda K^+(\bar{\Lambda}K^-)$  sharing radii with  $\Lambda K^-(\bar{\Lambda}K^+)$ .  
800 The figure shows results for three different treatments of the non-femtoscopic background: a polynomial  
801 fit to THERMINATOR 2 simulation to model the background (circles), a linear fit to the data to model  
802 the background (squares), and the Stavinsky method (crosses).

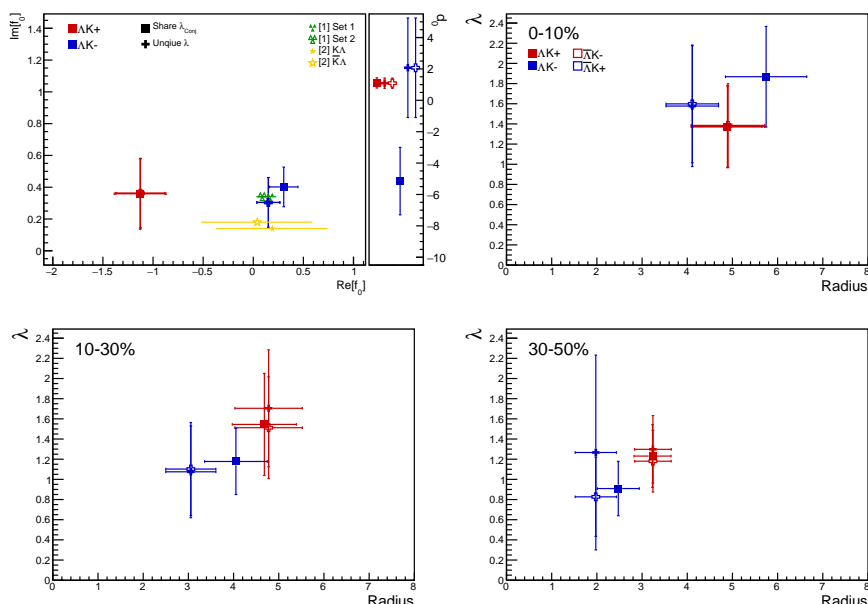


**Fig. 49:** Extracted fit results for all of our  $\Lambda(\bar{\Lambda})K^\pm$  systems across all studied centrality bins (0-10%, 10-30%, 30-50%). The  $\Lambda K^+(\bar{\Lambda}K^-)$  and  $\Lambda K^-(\bar{\Lambda}K^+)$  systems share both a radius and a  $\lambda$  parameter for each centrality bin (i.e. 3 total radius parameters, 3 total  $\lambda$  parameters). The figure shows results for three different treatments of the non-femtoscopic background: a polynomial fit to THERMINATOR 2 simulation to model the background (circles), a linear fit to the data to model the background (squares), and the Stavinsky method (crosses). Note,  $\Lambda K^+$  on the plot is shorthand for  $\Lambda K^+$  and  $\bar{\Lambda}K^- (\Lambda K^+(\bar{\Lambda}K^-))$ , and similar for the others. The green [9] and yellow [10] points show theoretical predictions made using chiral perturbation theory.


**Fig. 50:** Compare Fit Parameters: Free vs fixed  $\lambda$

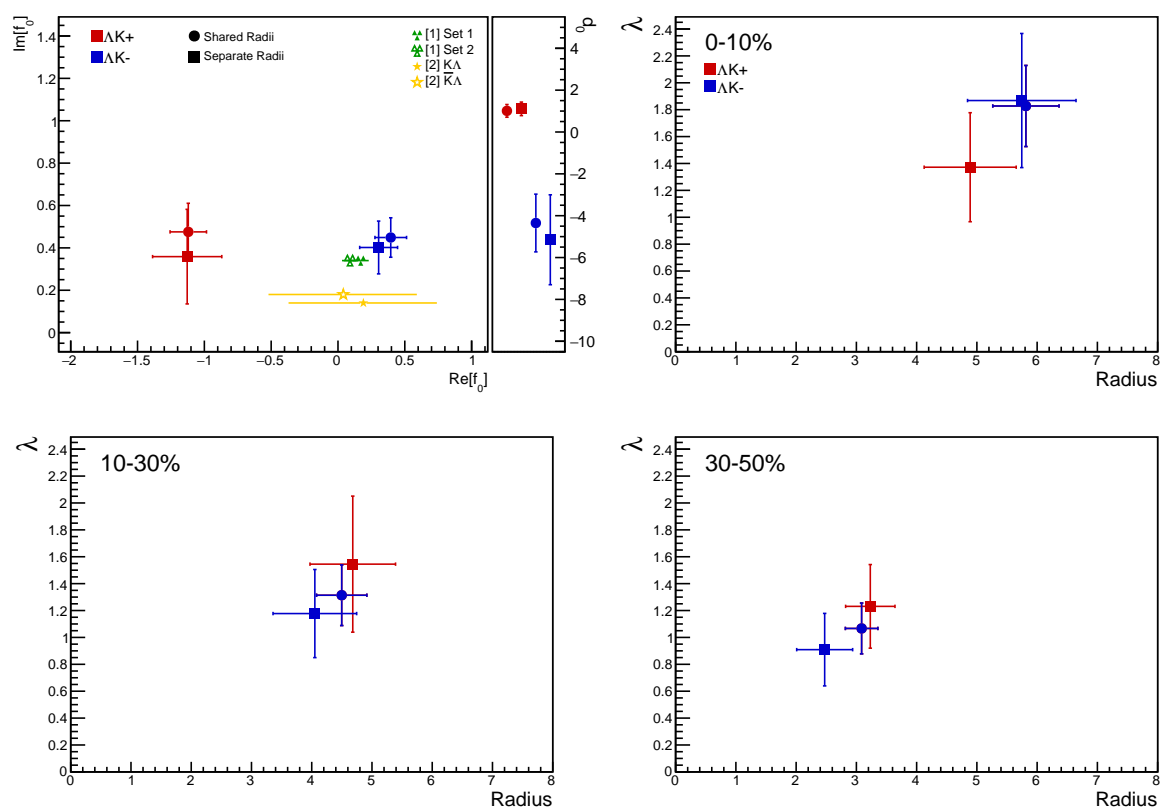


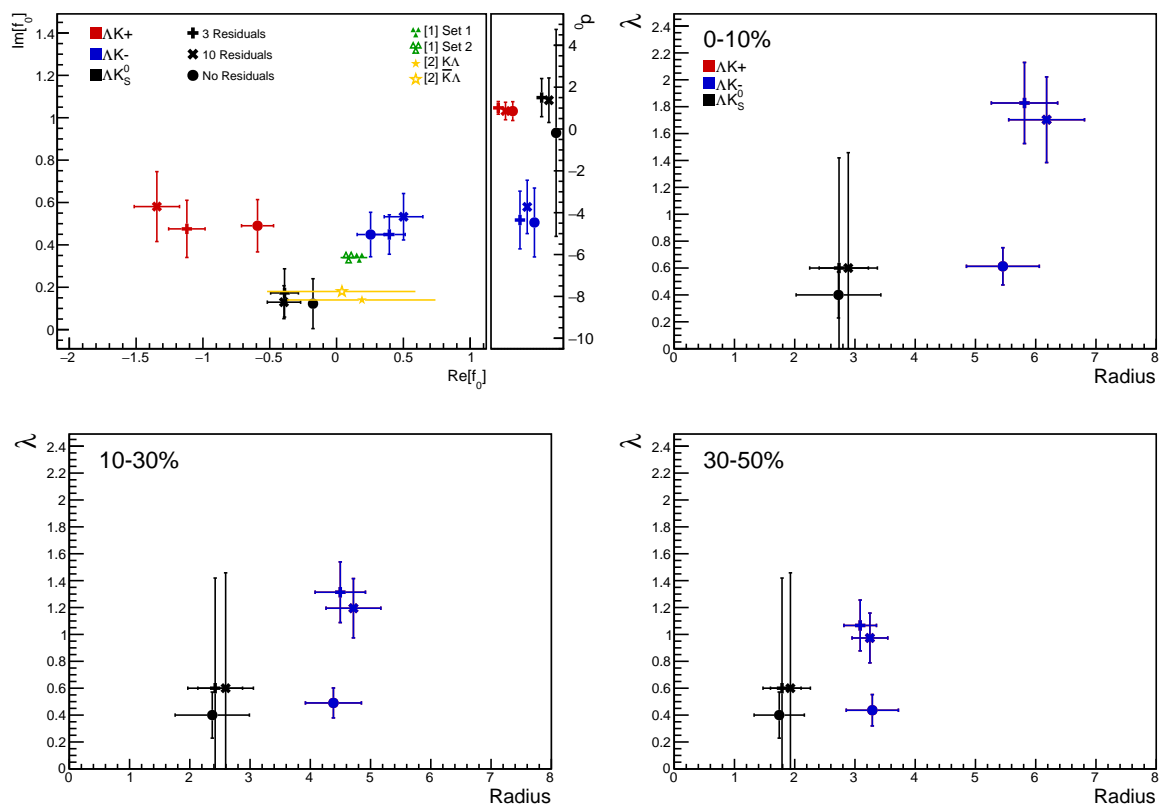
(a) Shared radii



(b) Separate radii

**Fig. 51:** Compare Fit Parameters: Shared vs unique  $\lambda$

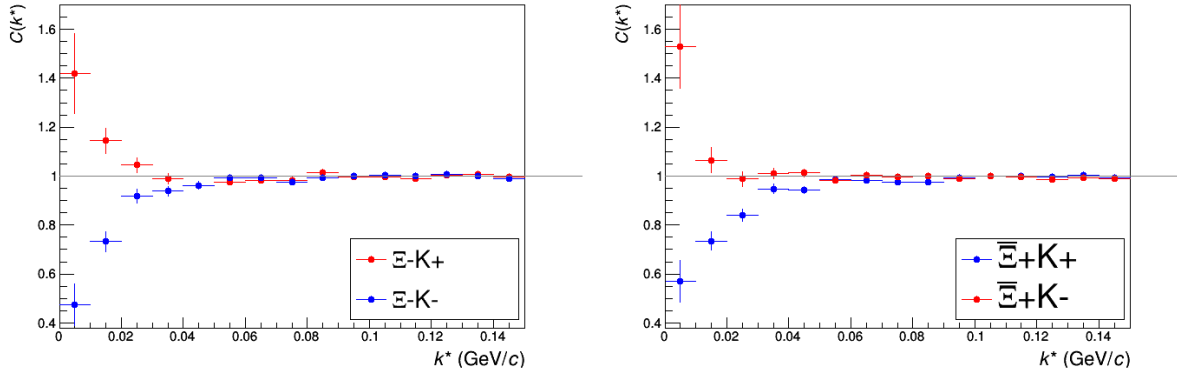
**Fig. 52:** Compare Fit Parameters: Shared vs. Separate Radii



**Fig. 53:** Compare Fit Parameters: Compare number of residuals

803 **7.2 Results:  $\Xi K^\pm$** 

804 Even without any fits to the data, the fact that the  $\Xi^- K^+$  data dips below unity (Fig. 54) is exciting, as  
 805 this cannot occur purely from a Coulomb interaction. We hope that this dip signifies that we are able to  
 806 peer through the overwhelming contribution from the Coulomb interaction to see the effects arising from  
 807 the strong interaction.

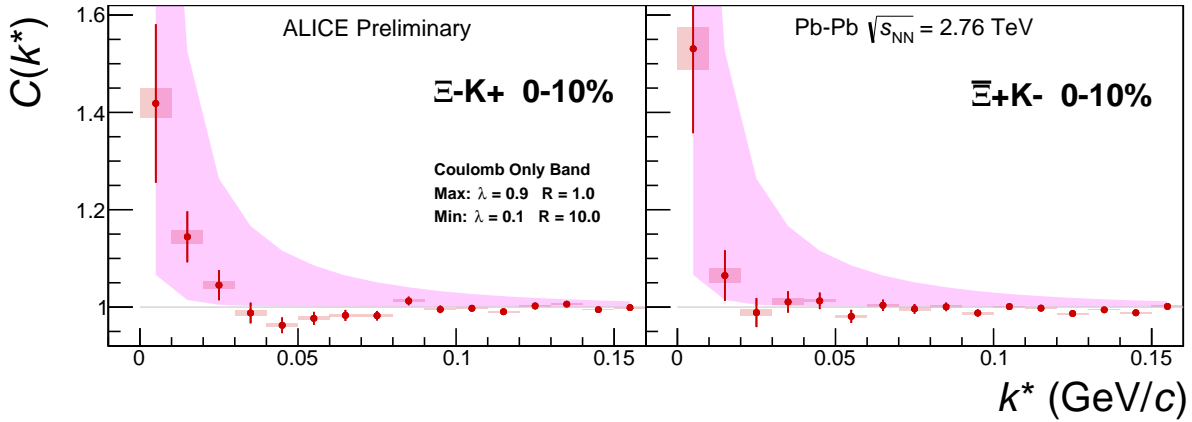
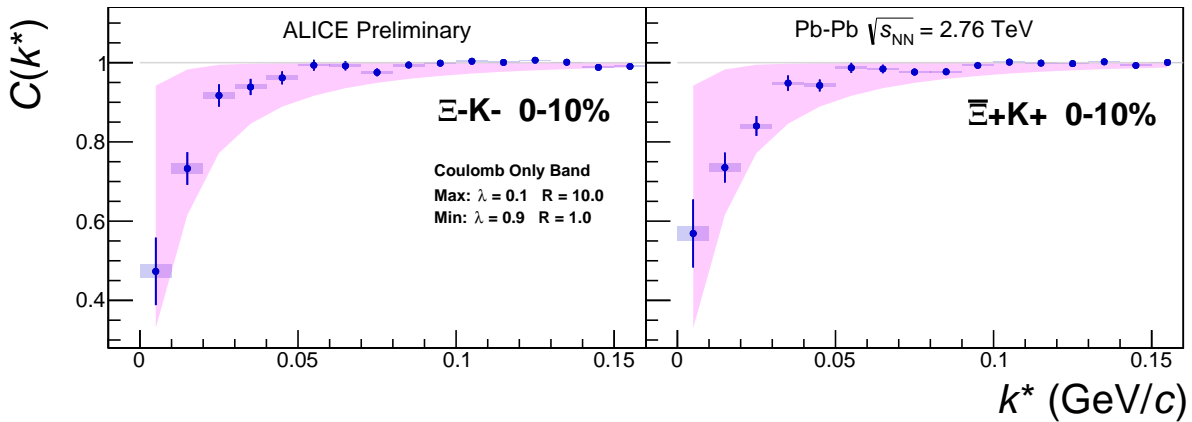


**Fig. 54:**  $\Xi K^\pm$  Results for 0-10% Centrality. (Left)  $\Xi^- K^+$  and  $\Xi^- K^-$  (Right)  $\Xi^+ K^+$  and  $\Xi^+ K^-$

808 Figure 55 demonstrates graphically, that the  $\Xi^- K^+$  results cannot be described by solely the Coulomb  
 809 interaction. In this figure, we present the data along with a Coulomb-only band. The Coulomb-only  
 810 band is spanned by two Coulomb-only curves, whose parameters are given in the figure. The Coulomb-only  
 811 curves were generated using a technique identical to the generation of the fit function, described  
 812 in Sec. 5.2, except, of course, with the nuclear scattering parameters all set to zero. The Coulomb-only  
 813 curves change monotonically with varying  $\lambda$  or varyin radius parametres, therefore, any curves built with  
 814 parameter sets intermediate to those use in the Coulomb-only band will be contained in the band.

815 Including the strong interaction into the simulation can change, sometimes dramatically, the resulting  
 816 correlation function, as shown in Figure 56. In the figure, the solid line represents a Coulomb-only curve,  
 817 i.e. a simulated correlation function with the strong interaction turned off. The dashed lines represent a  
 818 full simulation, including both the strong and Coulomb interactions. The two dashed lines differ only in  
 819 the real part of the assumed scattering length: positive in Set 1, and negative in Set 2. In the top figure,  
 820 for the  $\Xi^- K^+$  simulation, we see that parameter set 2, with a negative real part of the scattering length,  
 821 causes the simulated curve to dip below unity, as is seen in the data. If there is a parallel to be drawn  
 822 between this analysis and the  $\Lambda K$  analysis, we expect to see similar effects in the  $\Lambda K^+$  system and the  
 823  $\Xi^- K^+$  systems. In these systems, we could have an  $s\bar{s}$  annihilation picture. Or, another possible way of  
 824 thinking about these systems is in terms of net strangeness. The  $\Lambda K^+$  system has  $S=0$ , while the  $\Lambda K^-$   
 825 has  $S=-2$ . The  $\Xi^- K^+$  has  $S=-1$ , while the  $\Xi^- K^-$  has  $S=-3$ .

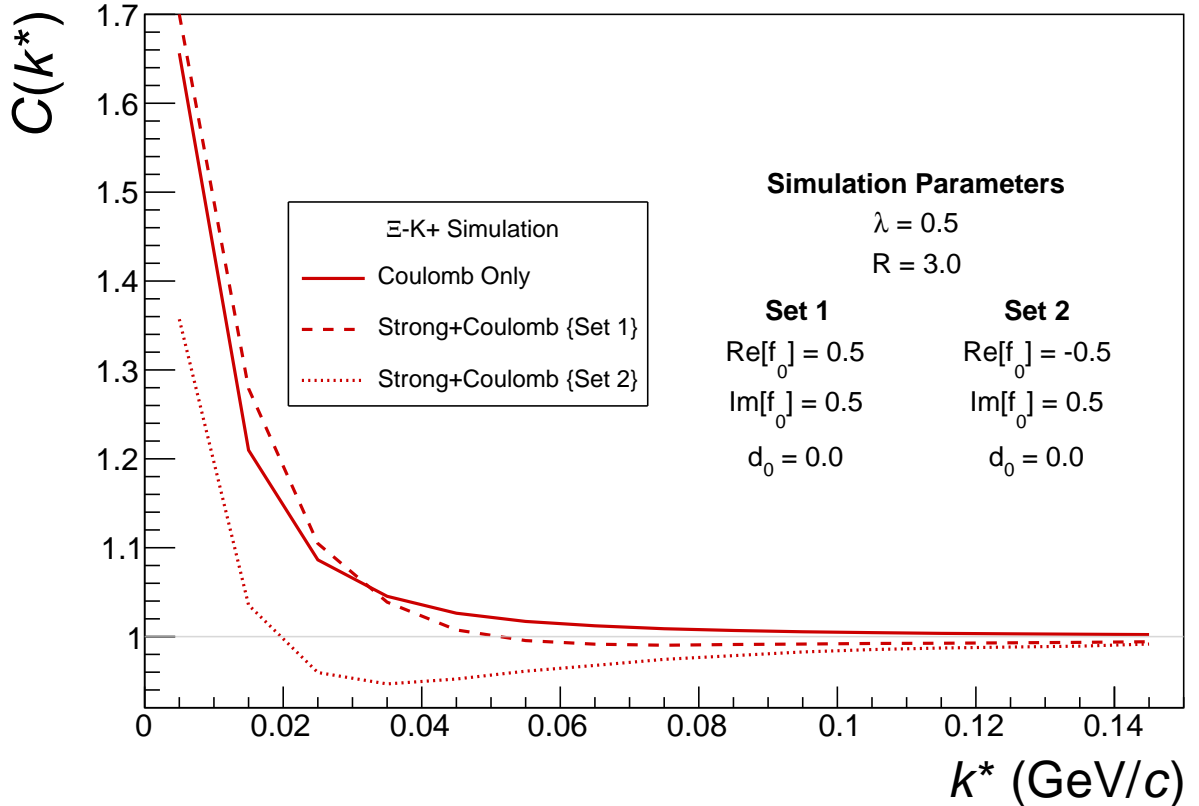
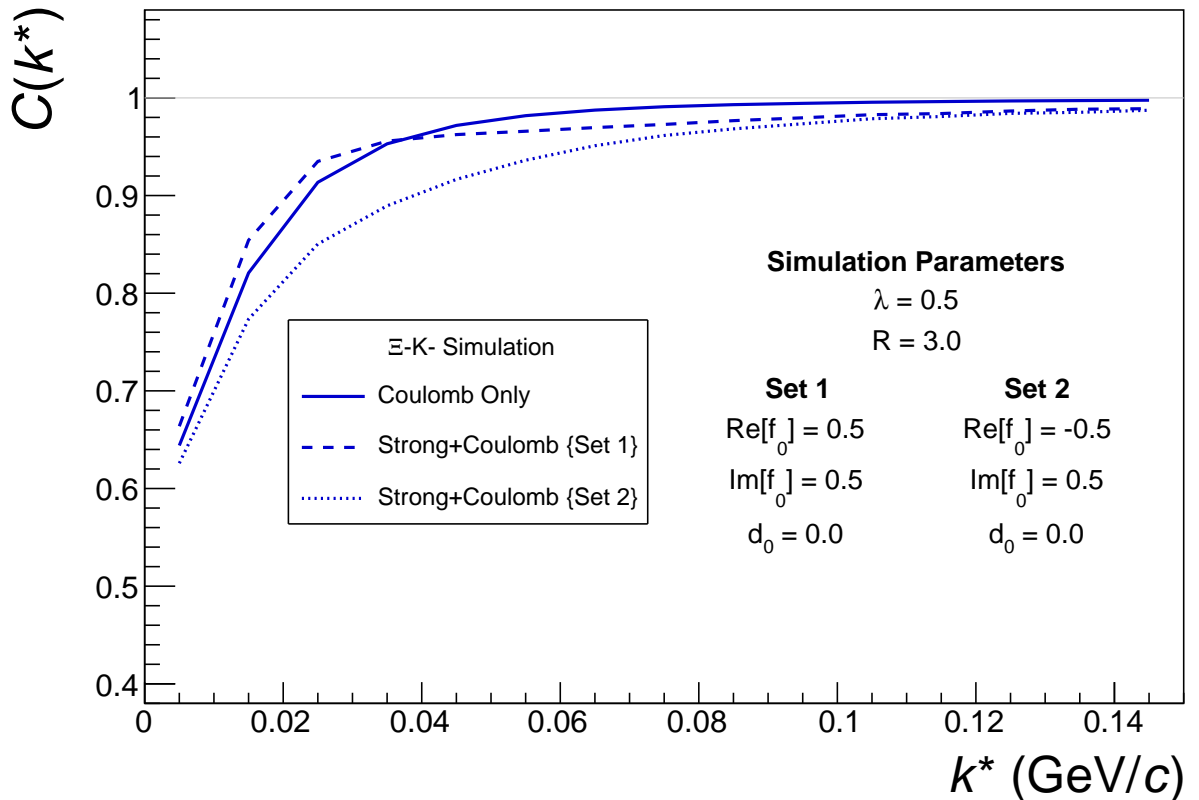
826 The author was asked to perform a global Coulomb-only fit to the data, to ensure that the system truly  
 827 could not be described simply by the Coulomb interaction. In order words, in the fit, the strong force was  
 828 turned off, and the  $\Xi^- K^+$ ,  $\Xi^+ K^-$ ,  $\Xi^- K^-$ ,  $\Xi^+ K^+$  systems all share one sinlge radius parameter, while the  
 829 pair and conjugate pair systems share a  $\lambda$  parameter. The results of this fit are shown in Figures 57 and  
 830 58. In Fig. 57, there was a lower limit of 0.1 fm placed on the radius parameter, and the radius parameter  
 831 was initialized to 3 fm (as seems reasonable, when considering the transverse mass of the system and  
 832 looking at Fig. ??). As is shown in the results, the radius parameter reached this unrealistic lower bound  
 833 of 0.1 fm. In Fig. 58, the parameters were all unbounded, and the radius parameter was initialized to 10  
 834 fm. In this case, the radius parameters reamins high, and ends at an unrealistic value of 10.84 fm. In both  
 835 cases, the  $\lambda$  parameters are too low. From these figures, we conclude that a global Coulomb-only fit is  
 836 not suitable for the data.

(a) (Left)  $\Xi\text{K}^+$  and (Right)  $\Xi\text{K}^-$ (b) (Left)  $\Xi\text{K}^-$  and (Right)  $\Xi\text{K}^+$ 

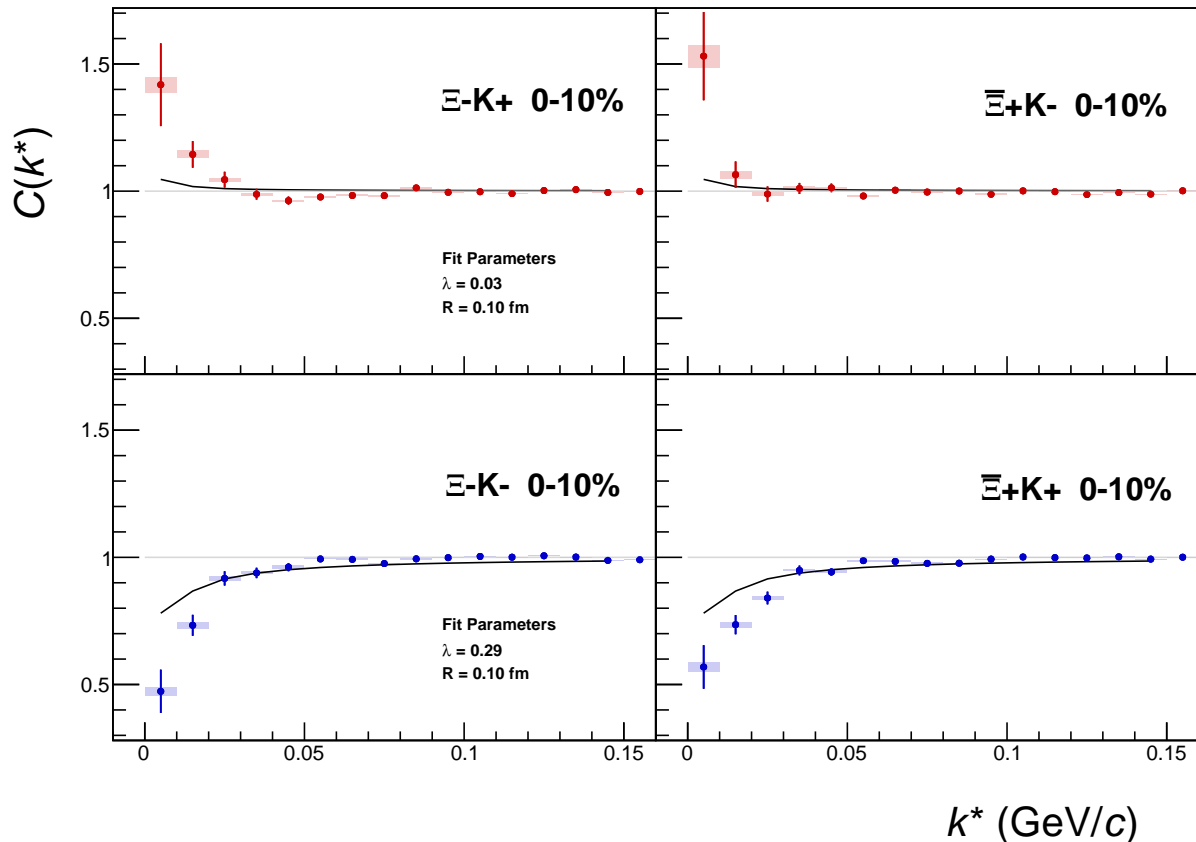
**Fig. 55:**  $\Xi\text{K}^\pm$  data with Coulomb-only bands for the 0-10% centrality bin. The Coulomb-only bands span two sets of Coulomb-only curves: (1)  $\lambda = 0.9$ , R = 1.0 fm and (2)  $\lambda = 0.1$ , R = 10.0 fm. The Coulomb-only curves are simulated correlation functions for the respective pair system assuming only a Coulomb interaction, i.e. ignoring the strong interaction. The Coulomb-only curves change monotonically with varying  $\lambda$  and varying R, therefore, any intermediate parameter set will fall within this Coulomb-only band.

837 Although the global Coulomb-only fit failed, it is possible that a Coulomb-only fit performed on  $\Xi\text{-K}^+$   
 838 and  $\Xi\text{+K}^-$  separately from  $\Xi\text{-K}^-$  and  $\Xi\text{+K}^+$  could be suitable. The result of such fits are shown in  
 839 Figures 59 and 60. Figure 59, shows that the fit is not able to describe the dip in the  $\Xi\text{-K}^+$  data below  
 840 unity. Of course, this is obviously true for an attractive Coulomb-only fit. The radius parameter of  
 841 8.43 fm extracted from this fit is unrealistically large. In Figure 60 shows the Coulomb-only fit can  
 842 described the  $\Xi\text{-K}^-$  data reasonable well; although the extracted radius of 3.73 fm is somewhat larger  
 843 than expected.

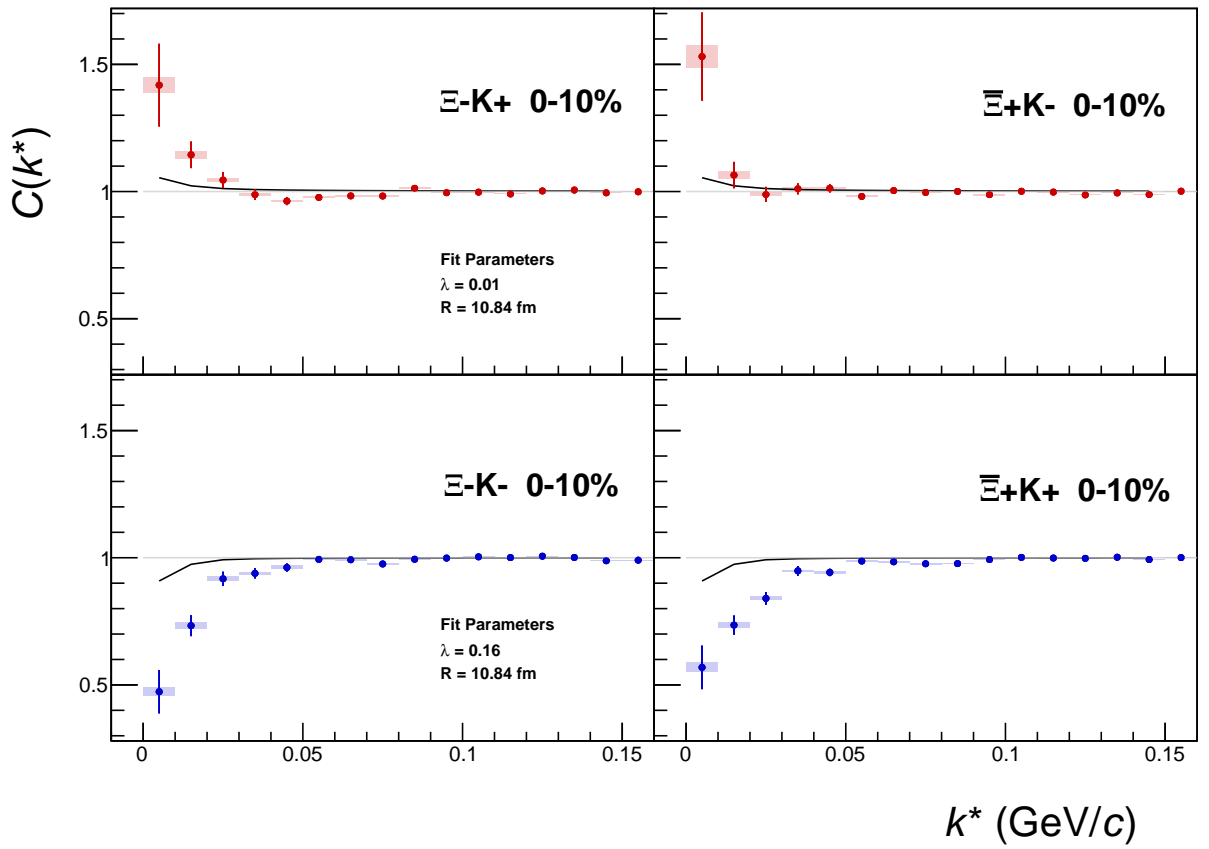
## 8 To Do


 (a)  $\Xi K^+$  and  $\bar{\Xi} K^-$  simulation

 (b)  $\Xi K^-$  and  $\bar{\Xi} K^+$  simulation

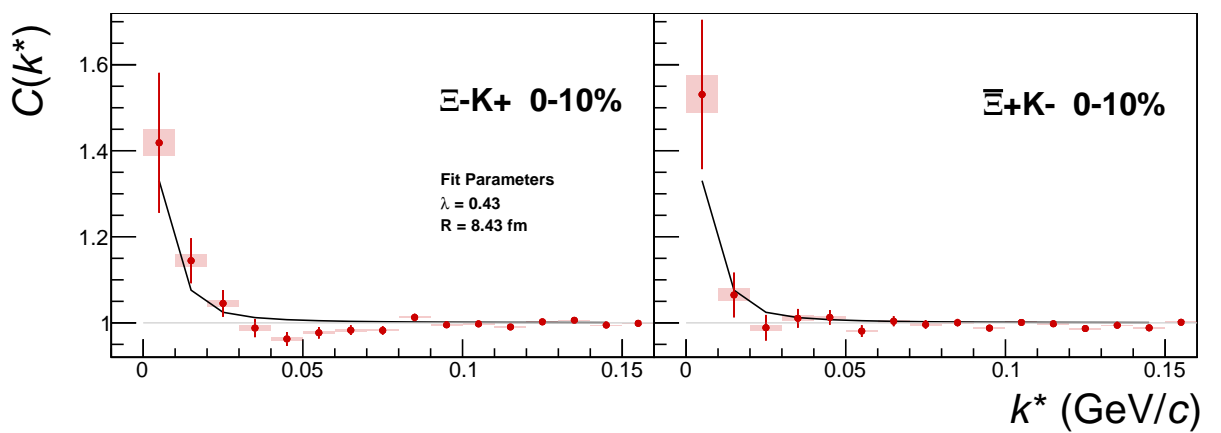
**Fig. 56:** Effect on the Coulomb-only curve of including the strong interaction for  $\Xi K^\pm$  systems. The solid line represents a Coulomb-only curve, i.e. a simulated correlation function with the strong interaction turned off. The dashed lines represent a full simulation, including both the strong and Coulomb interactions. The two dashed lines differ only in the real part of the assumed scattering length: positive in Set 1, and negative in Set 2.



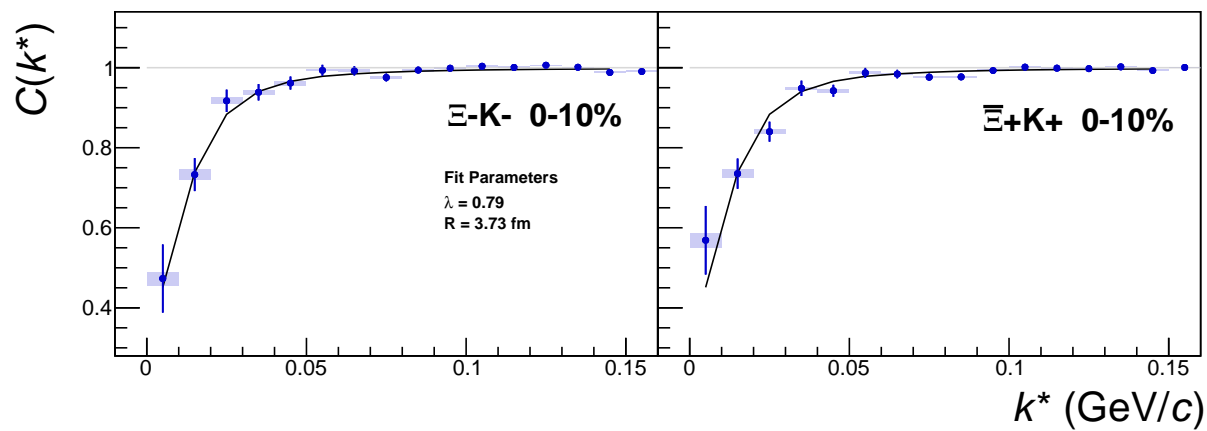
**Fig. 57:**  $\Xi K^\pm$  Global Coulomb-only fit (Set 1) for 0-10% centrality. In this fit, there was a lower limit of 0.1 fm placed on the radius parameter, and the radius parameter was initialized to 3 fm (as seems reasonable, when considering the transverse mass of the system and looking at Fig. ??). As is shown in the results, the radius parameter reached this unrealistic lower bound of 0.1 fm. Also, the extracted  $\lambda$  parameters are too low.



**Fig. 58:**  $\Xi K^\pm$  Global Coulomb-only fit (Set 2) for 0-10% centrality. In this fit, the parameters were all unbounded, and the radius parameter was initialized to 10 fm. In this case, the radius parameters remain high, and ends at an unrealistic value of 10.84 fm. Also, the extracted  $\lambda$  parameters are too low.



**Fig. 59:**  $\Xi^- K^+$  Coulomb-only fit for 0-10% centrality

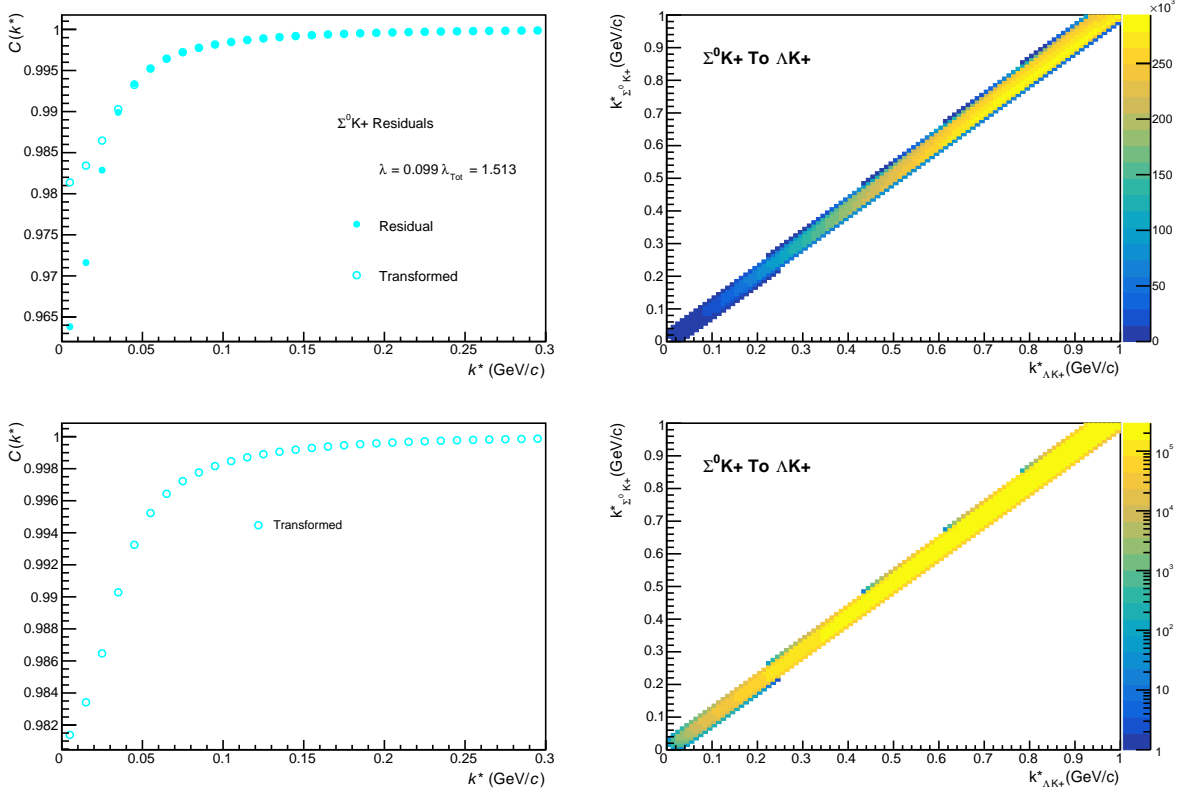


**Fig. 60:**  $\Xi^- K^-$  Coulomb-only fit for 0-10% centrality

845 **9 Additional Figures**

846 **9.1 Residuals**

847 **9.1.1  $\Lambda K^+$  Residuals**



**Fig. 61:** Residuals:  $\Sigma^0 K^+$  to  $\Lambda K^+$  (0-10% Centrality)

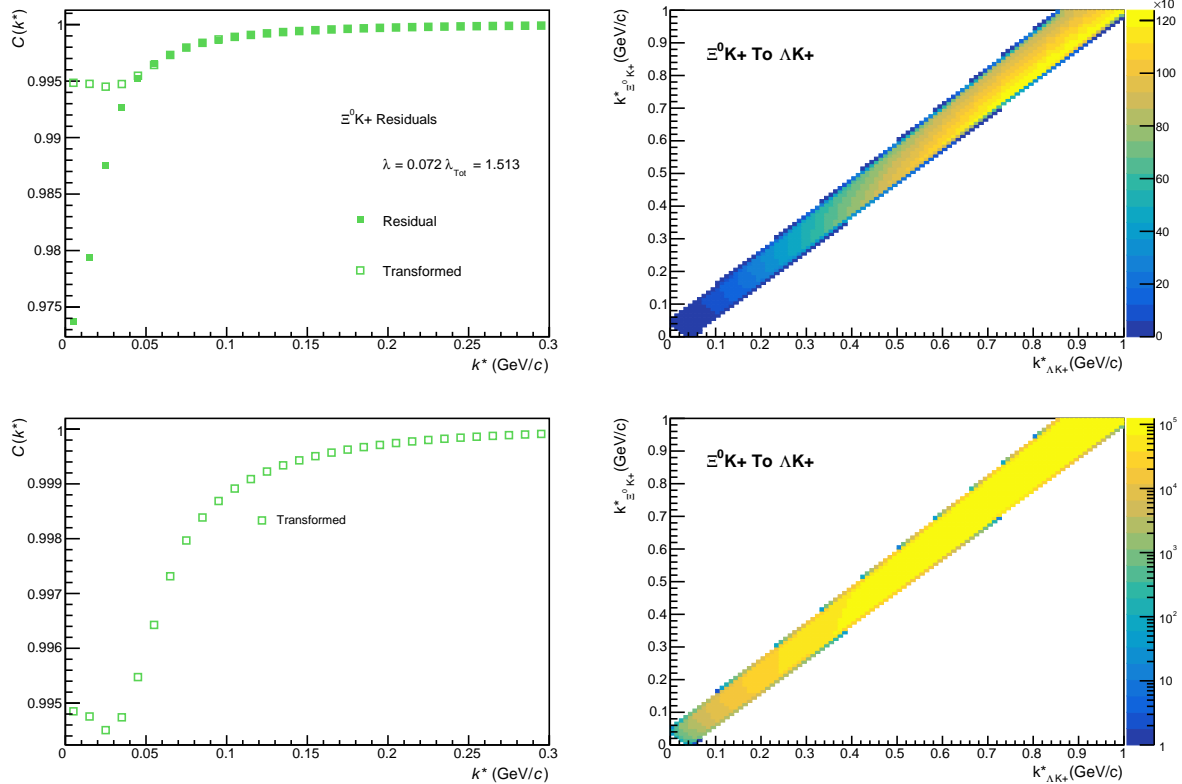


Fig. 62: Residuals:  $\Xi^0 \text{K}^+$  to  $\Lambda \text{K}^+$  (0-10% Centrality)

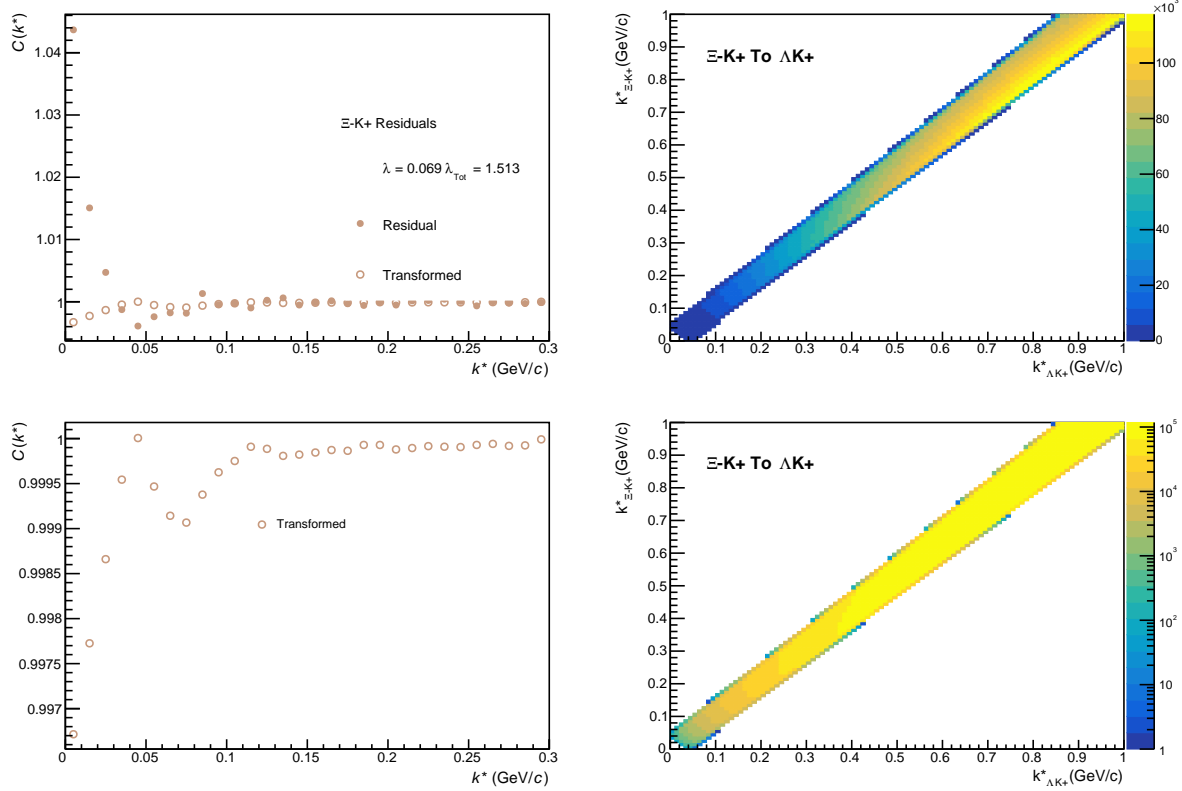
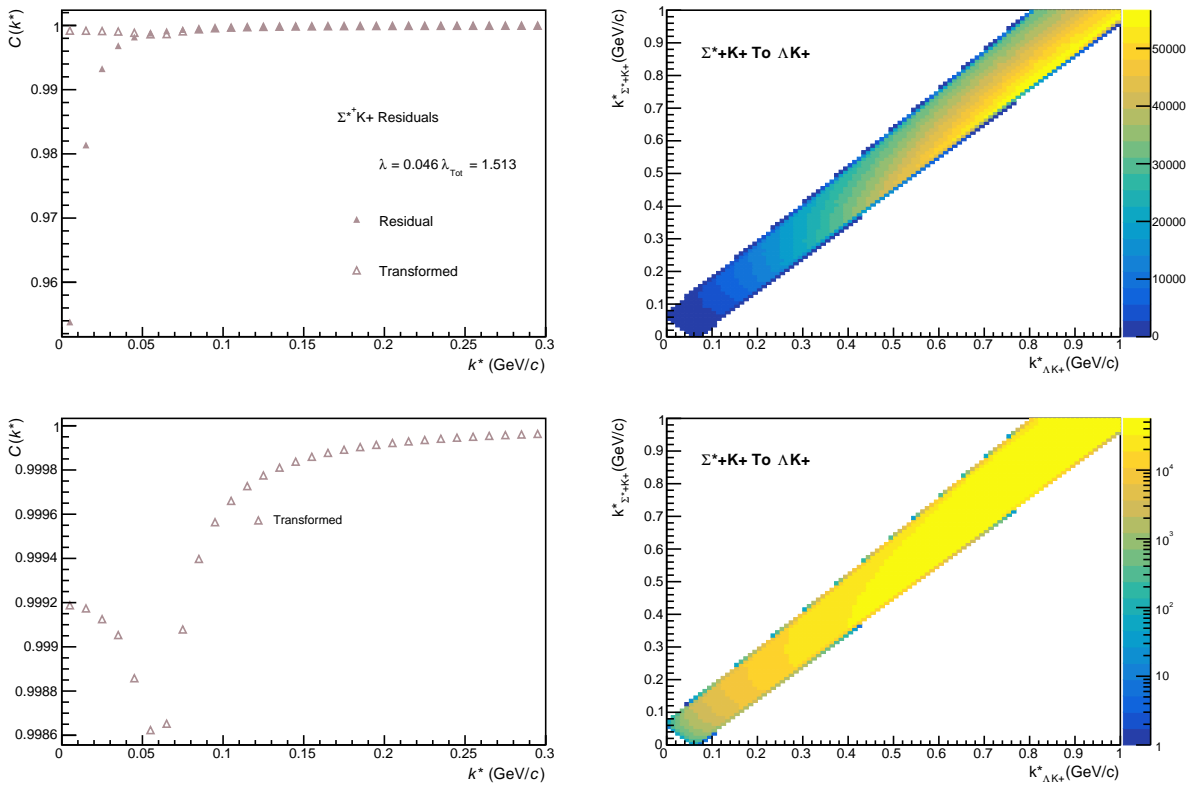
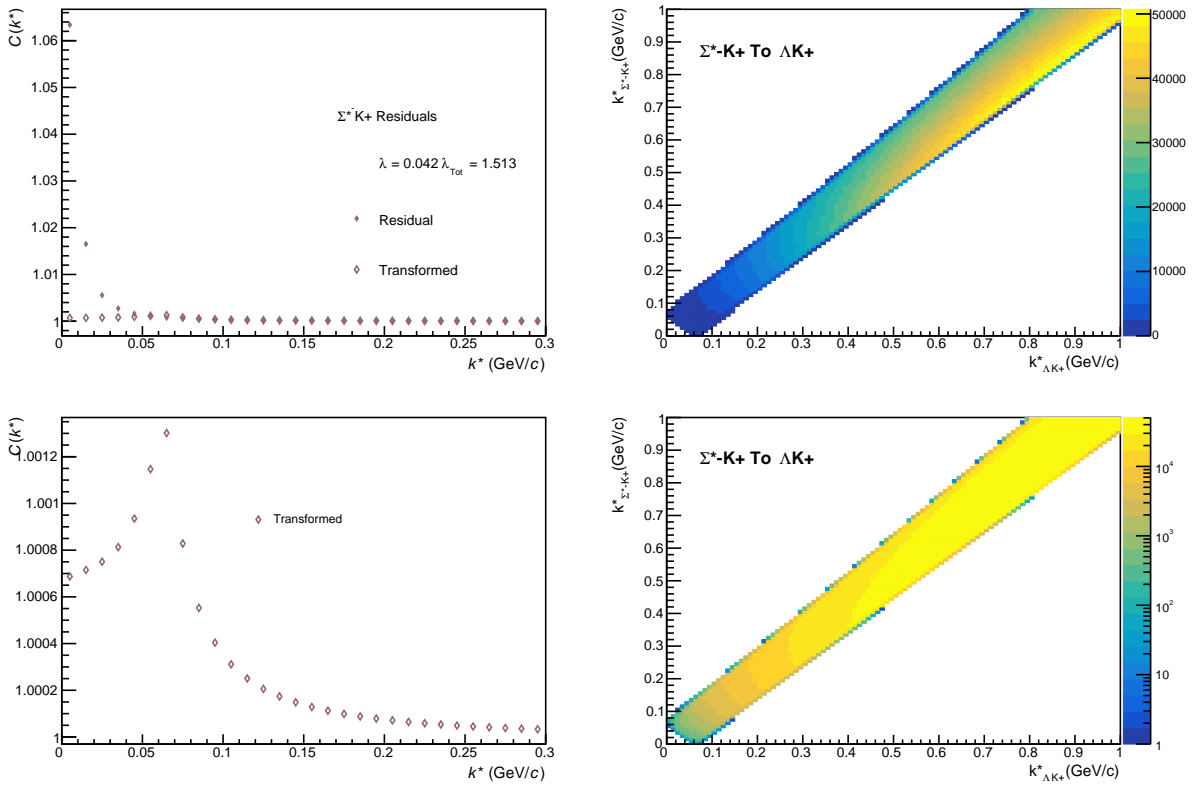
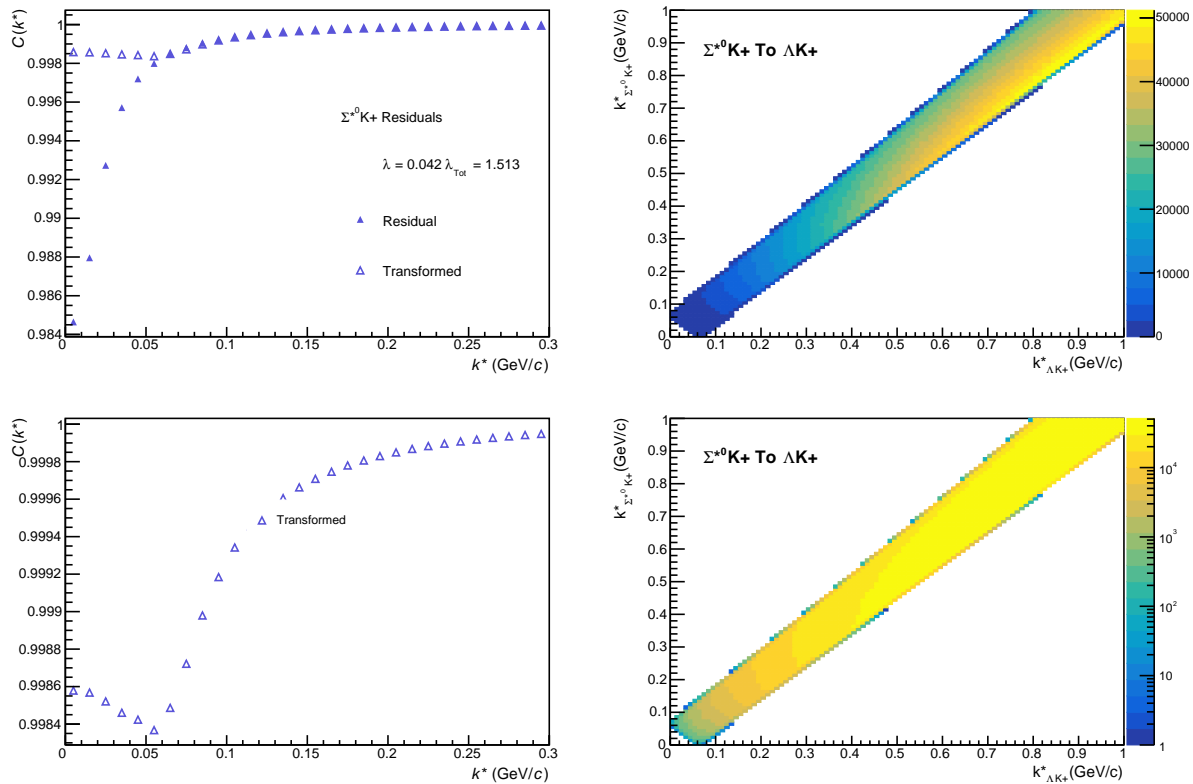
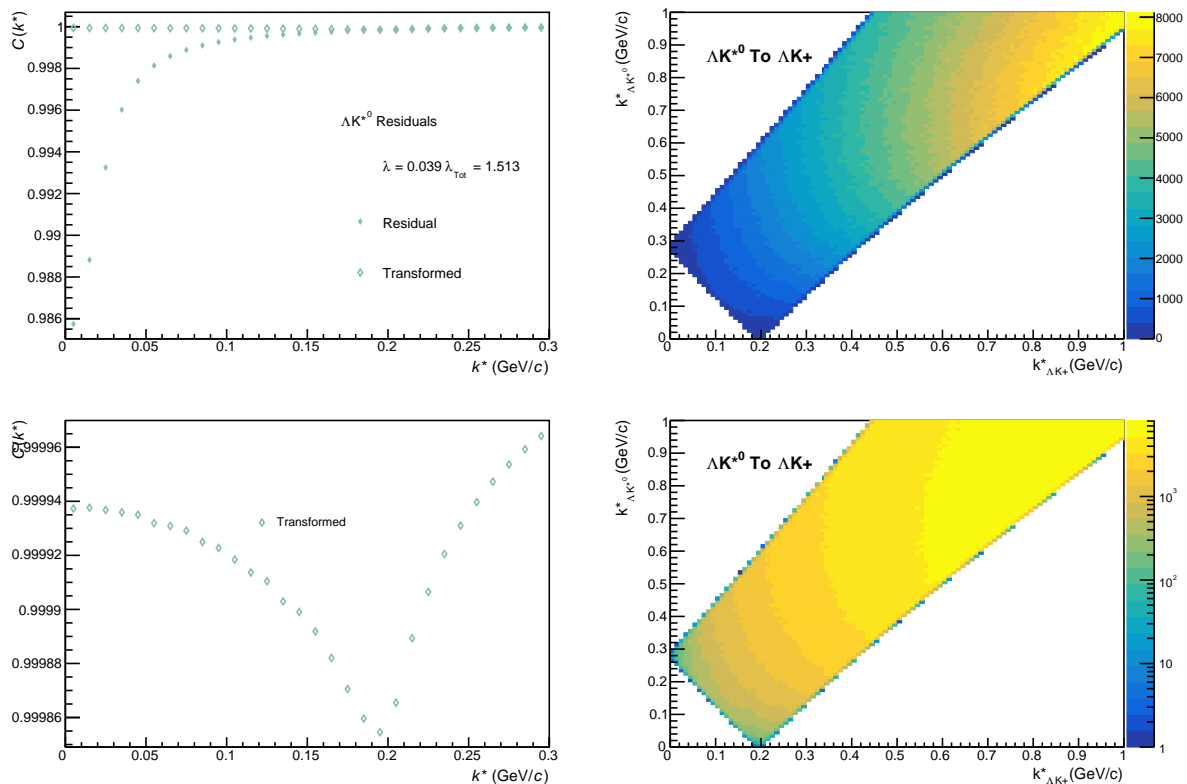


Fig. 63: Residuals:  $\Xi^- \text{K}^+$  to  $\Lambda \text{K}^+$  (0-10% Centrality)

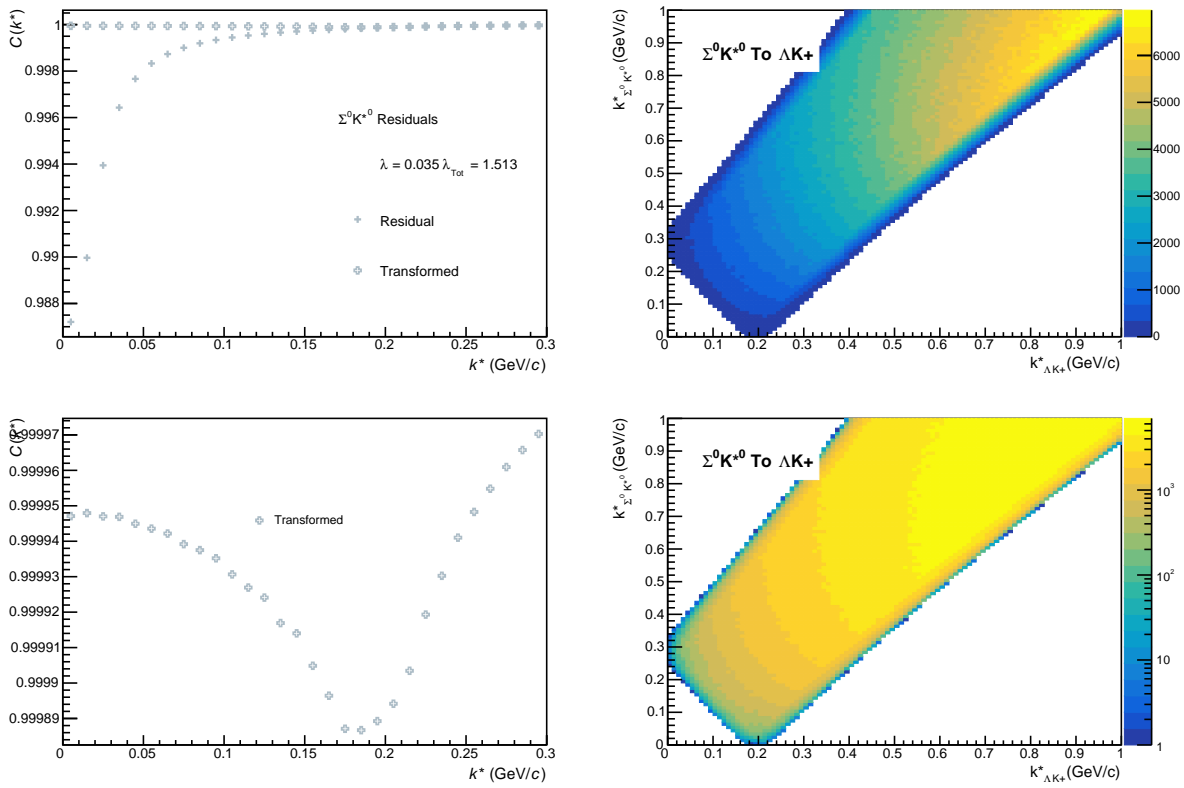
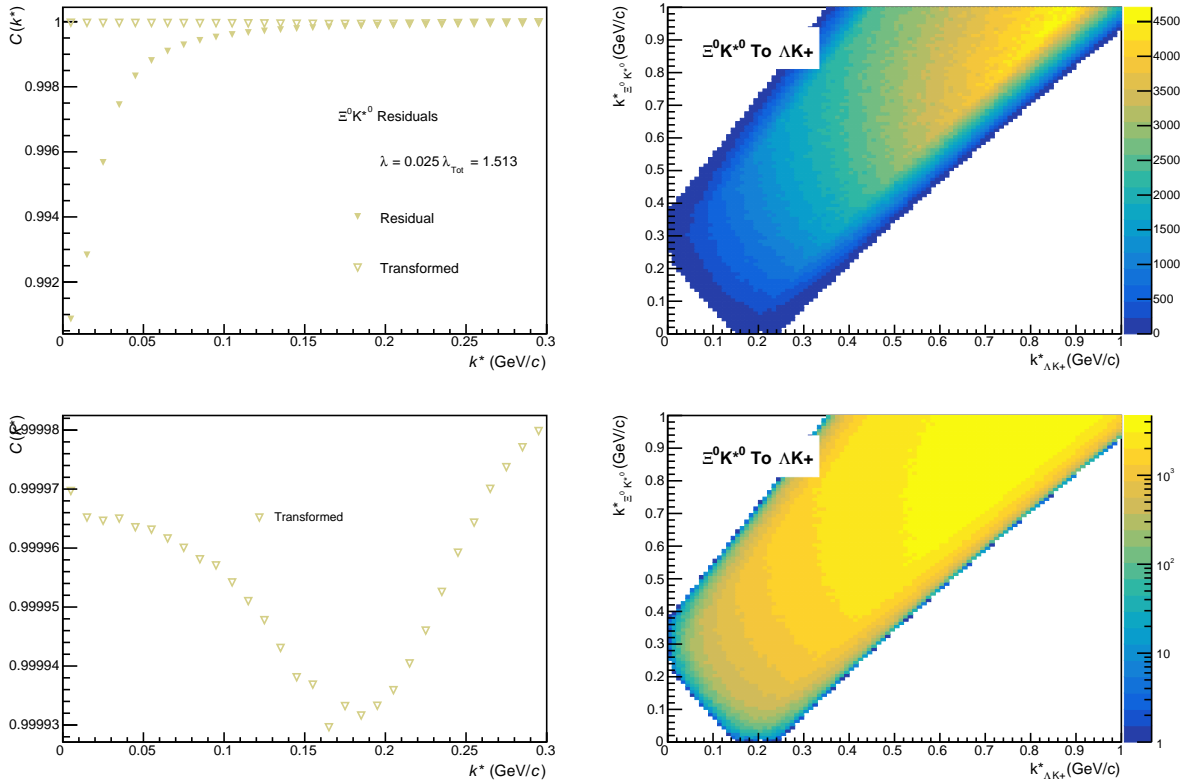

 Fig. 64: Residuals:  $\Sigma^{*+} K^+$  to  $\Lambda K^+$  (0-10% Centrality)

 Fig. 65: Residuals:  $\Sigma^{*-} K^+$  to  $\Lambda K^+$  (0-10% Centrality)

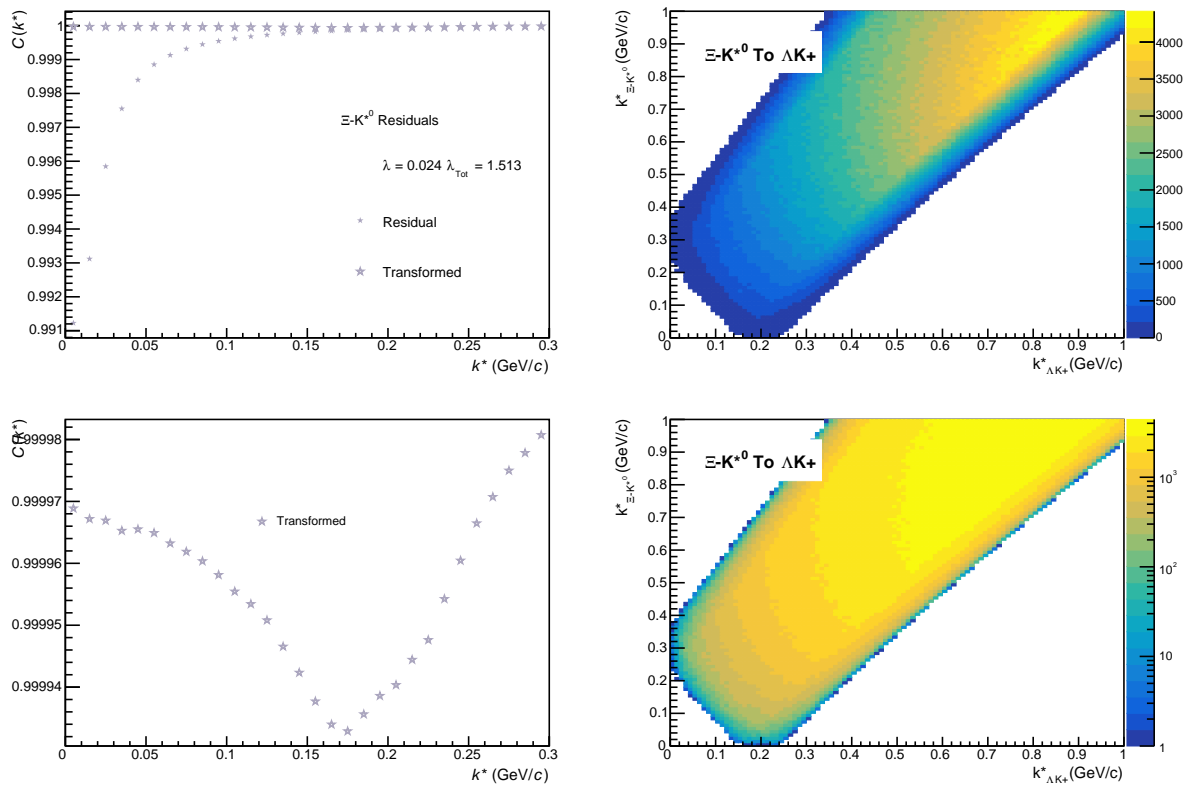


**Fig. 66:** Residuals:  $\Sigma^{*0} \text{K}^+$  to  $\Lambda \text{K}^+$  (0-10% Centrality)

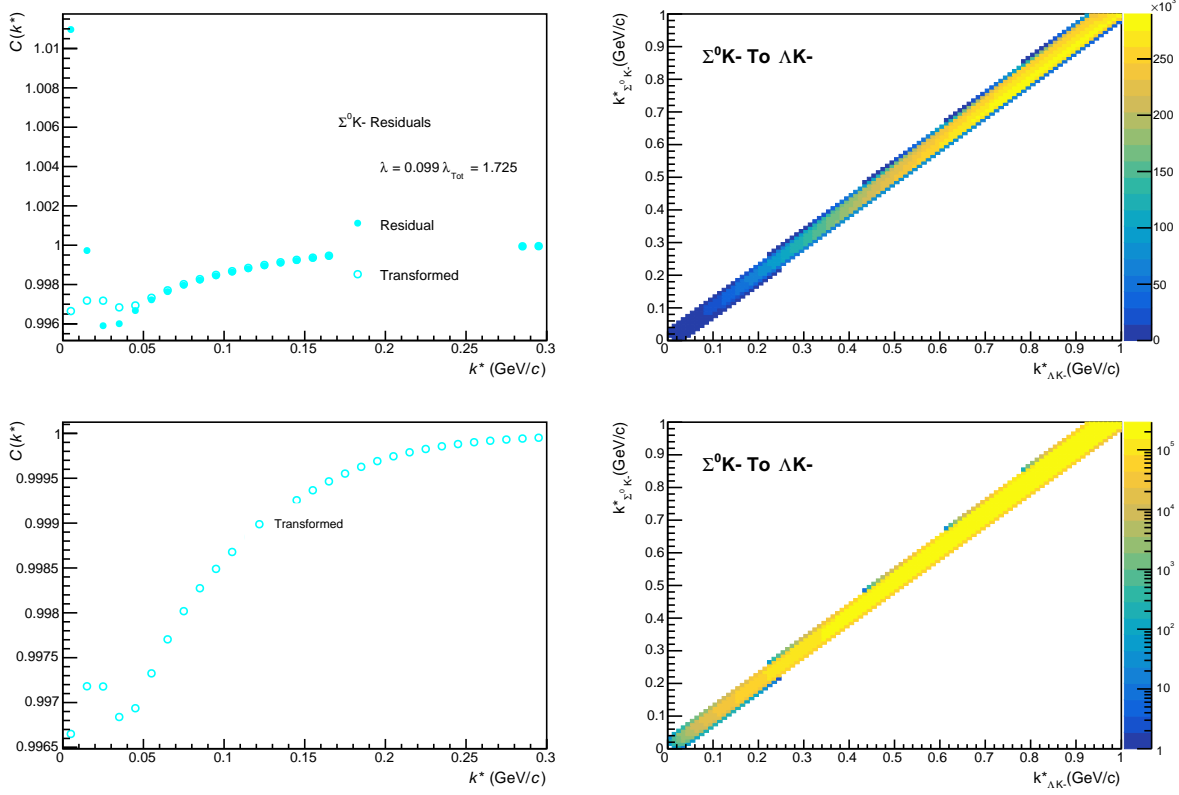


**Fig. 67:** Residuals:  $\Lambda \text{K}^{*0}$  to  $\Lambda \text{K}^+$  (0-10% Centrality)

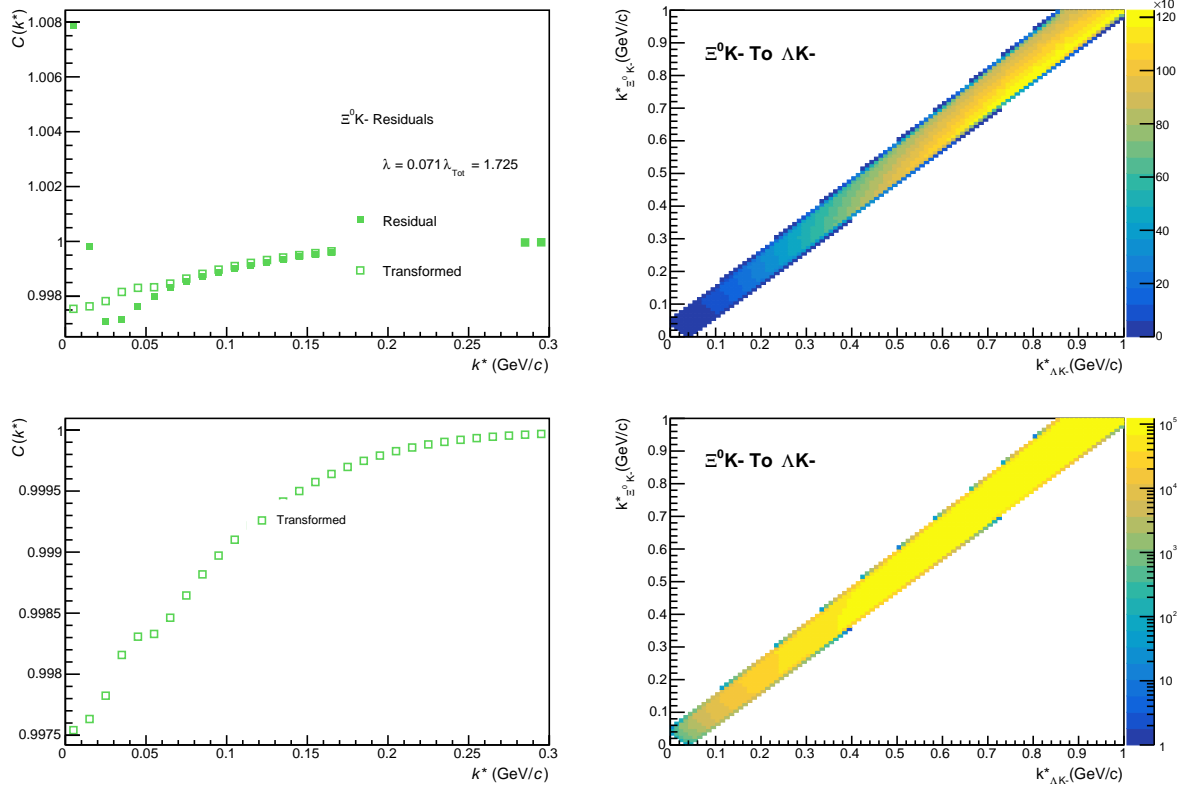

**Fig. 68:** Residuals:  $\Sigma^0 K^{*0}$  to  $\Lambda K^+$  (0-10% Centrality)

**Fig. 69:** Residuals:  $\Xi^0 K^{*0}$  to  $\Lambda K^+$  (0-10% Centrality)



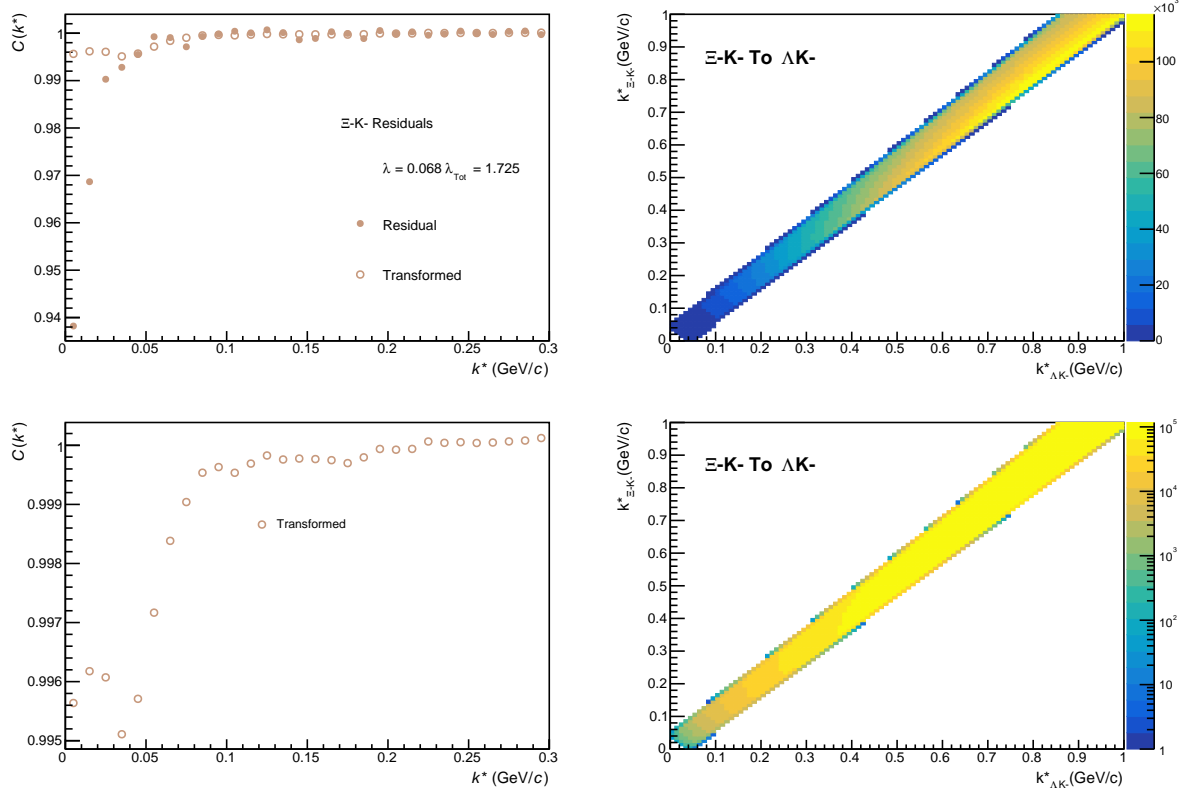
**Fig. 70:** Residuals:  $\Xi^- K^{*0}$  to  $\Lambda K^+$  (0-10% Centrality)

848 **9.1.2  $\Lambda K^-$  Residuals**


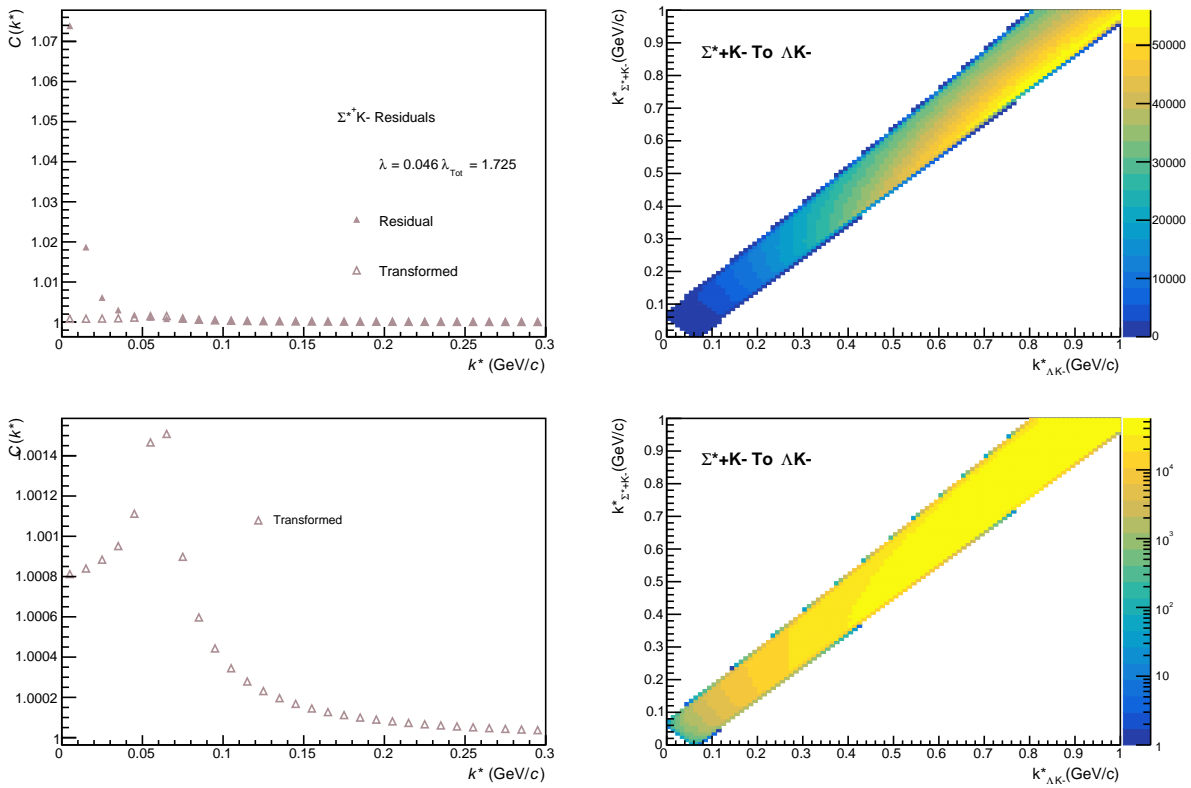
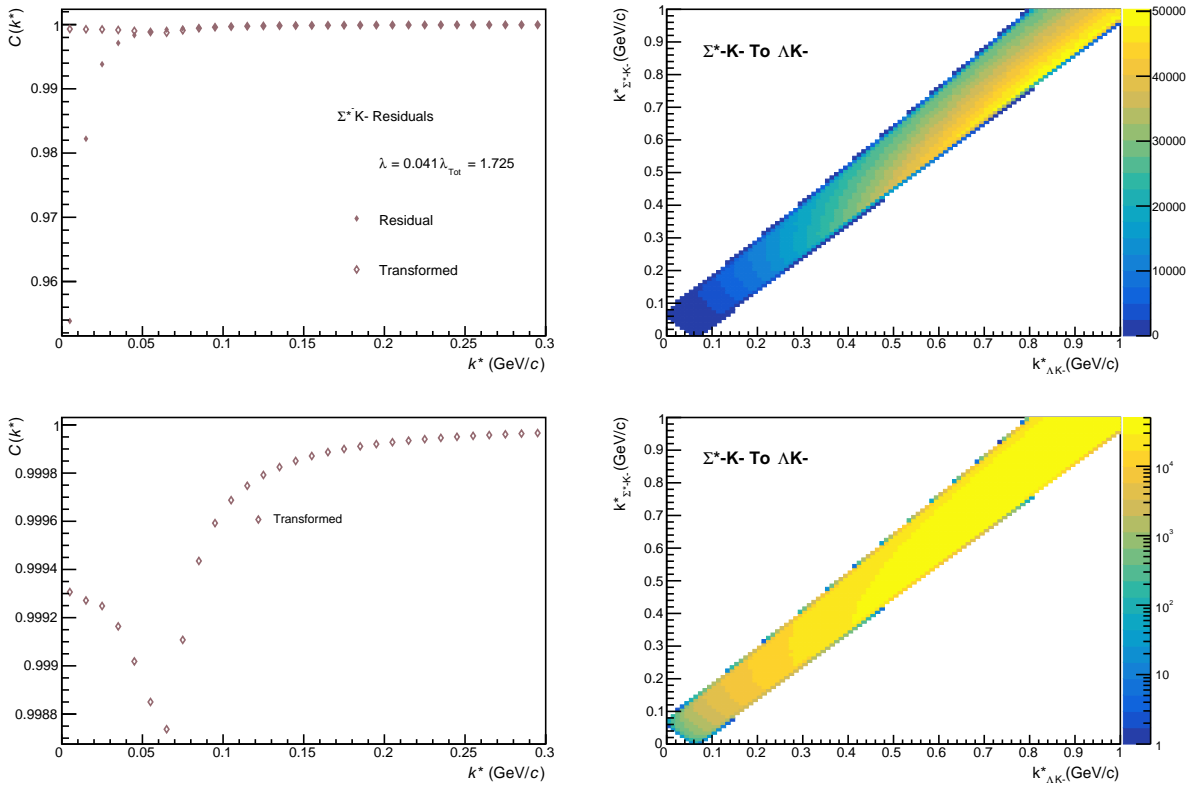
**Fig. 71:** Residuals:  $\Sigma^0 K^-$  to  $\Lambda K^-$  (0-10% Centrality)

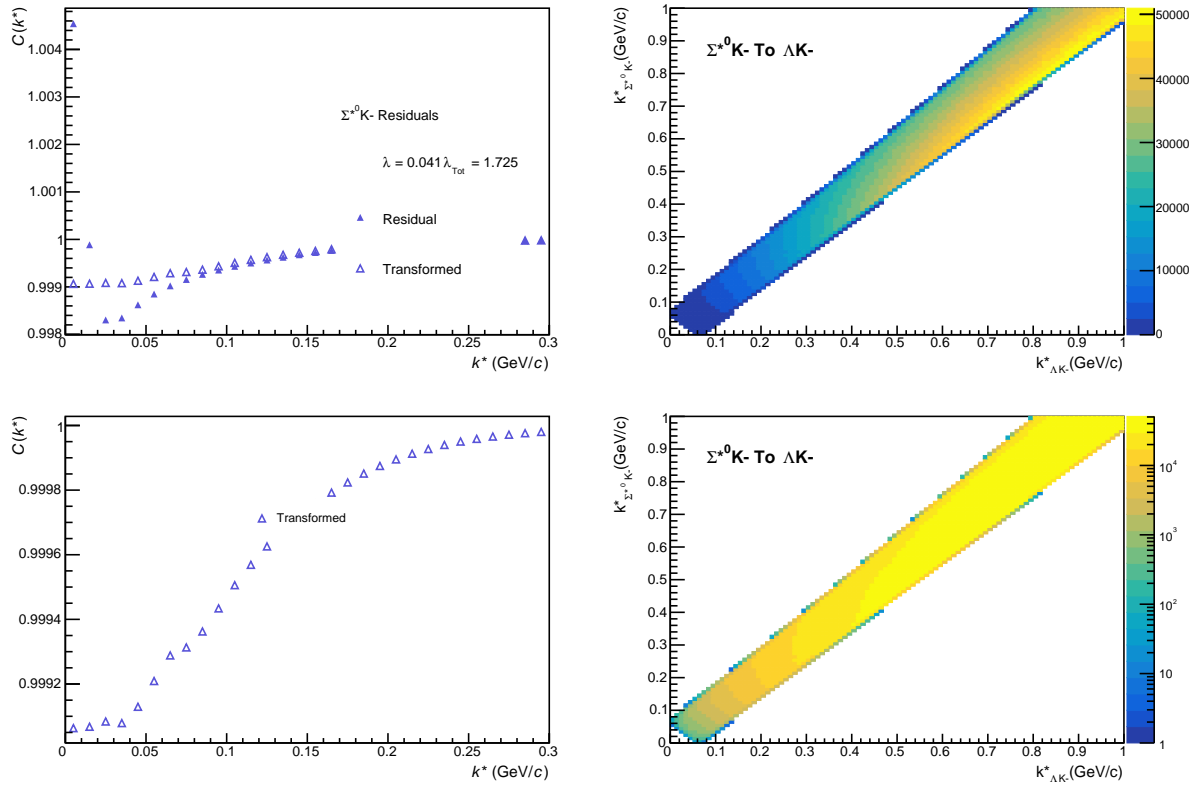


**Fig. 72:** Residuals:  $\Xi^0 \text{K}^-$  to  $\Lambda \text{K}^-$  (0-10% Centrality)

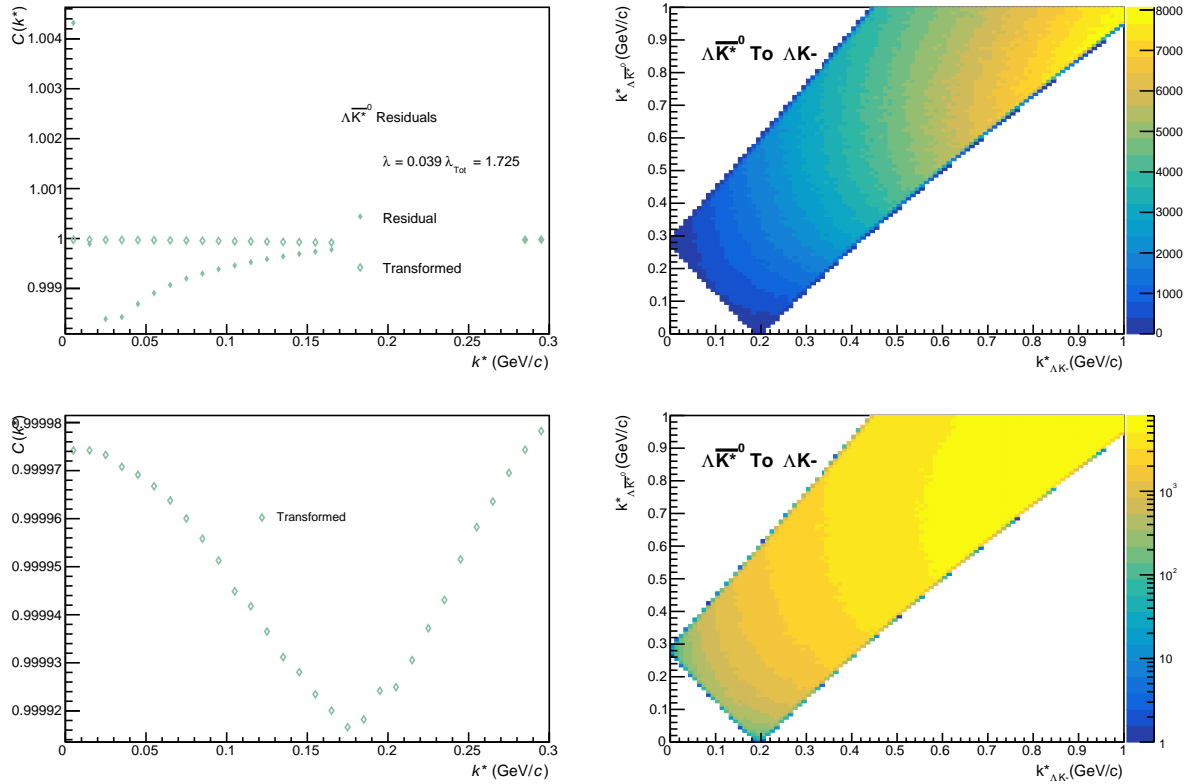


**Fig. 73:** Residuals:  $\Xi^- \text{K}^-$  to  $\Lambda \text{K}^-$  (0-10% Centrality)

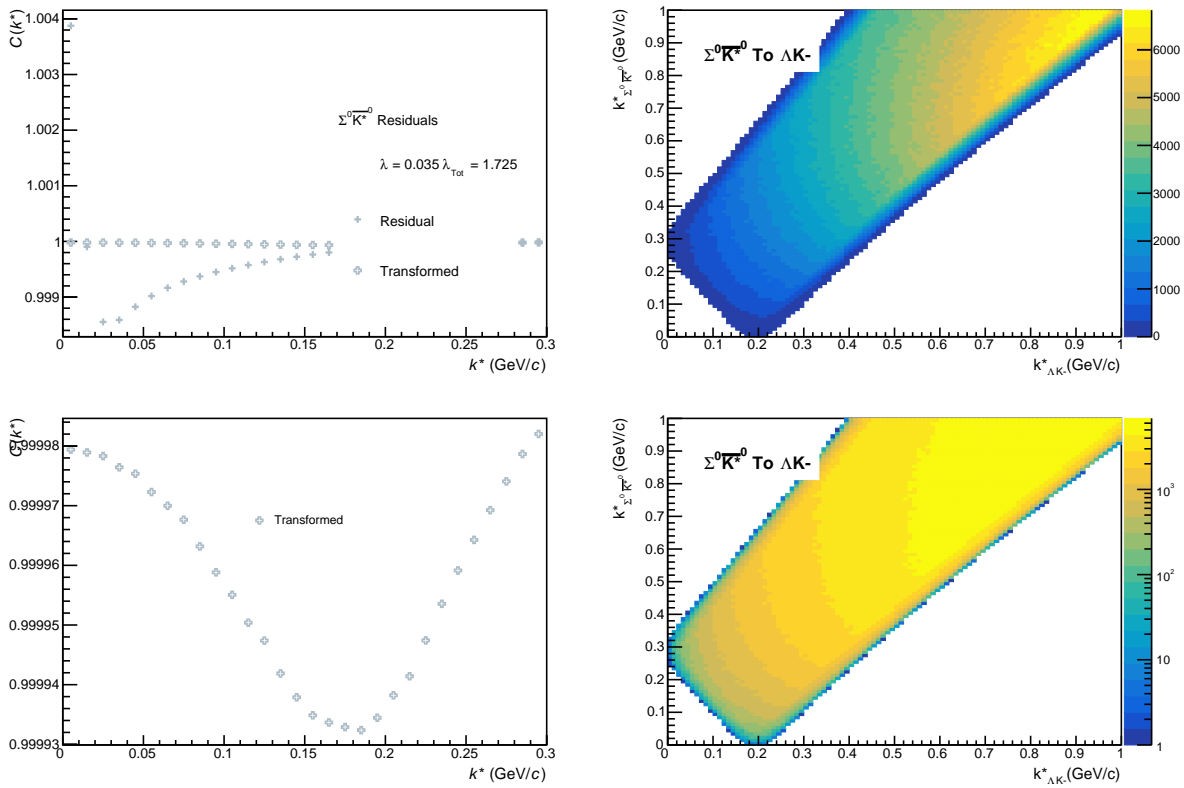
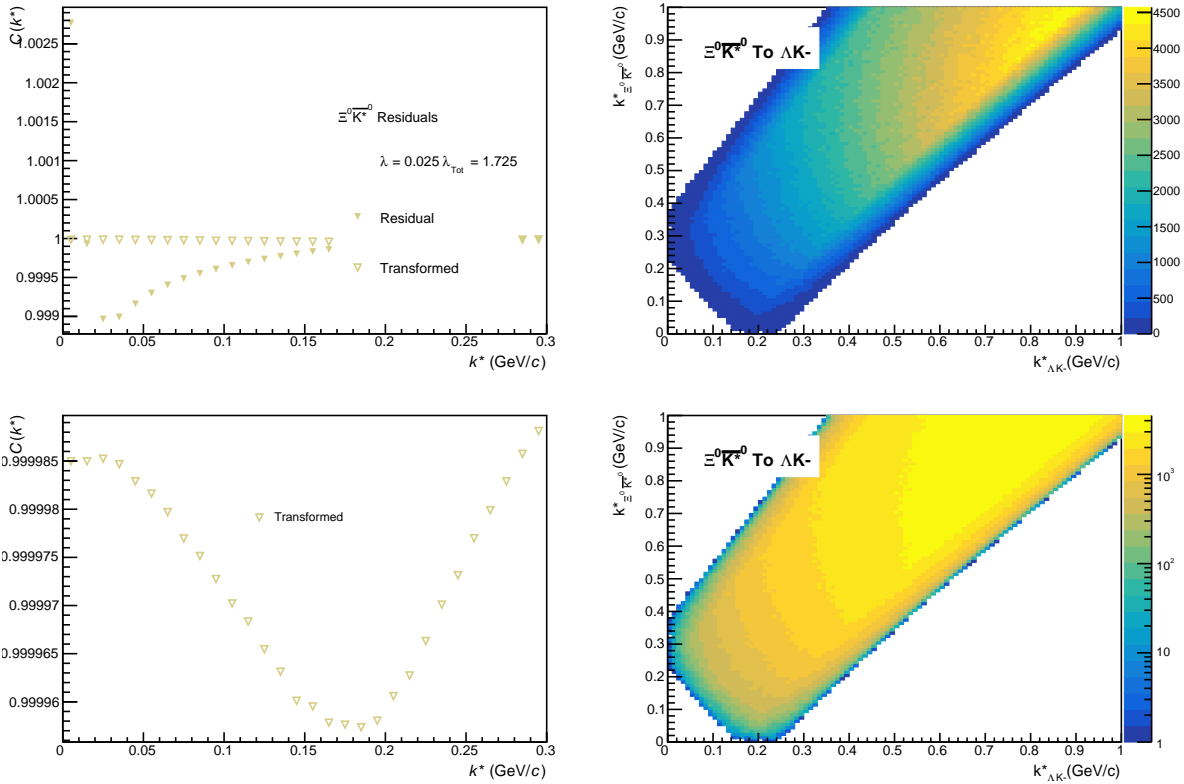

**Fig. 74:** Residuals:  $\Sigma^{*+} K^-$  to  $\Lambda K^-$  (0-10% Centrality)

**Fig. 75:** Residuals:  $\Sigma^{*-} K^-$  to  $\Lambda K^-$  (0-10% Centrality)

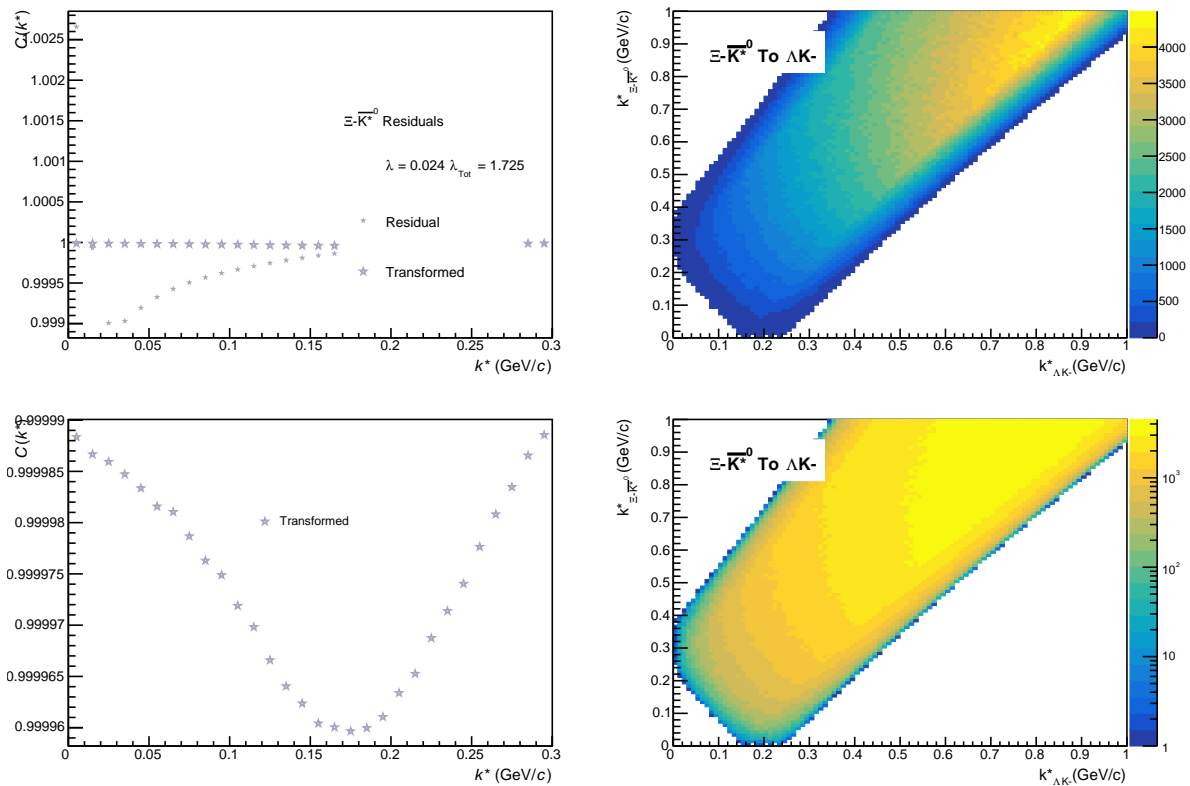


**Fig. 76:** Residuals:  $\Sigma^0 \text{K}^-$  to  $\Lambda \text{K}^-$  (0-10% Centrality)

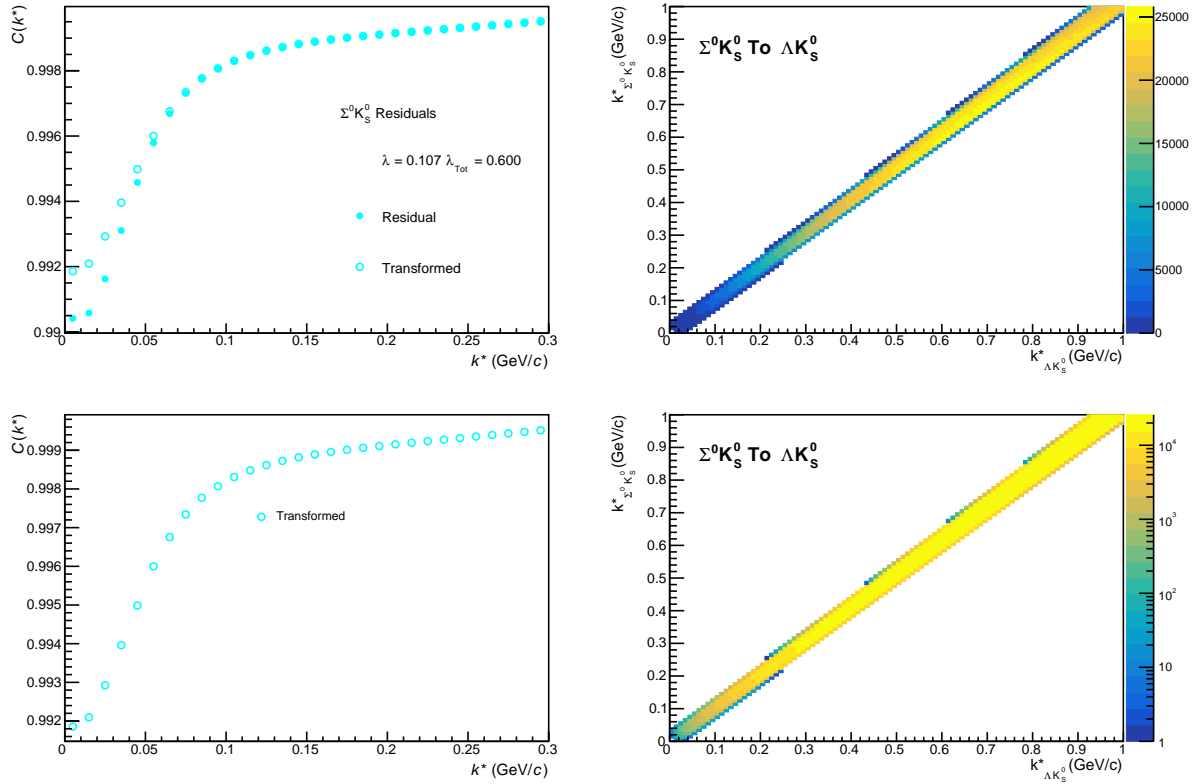


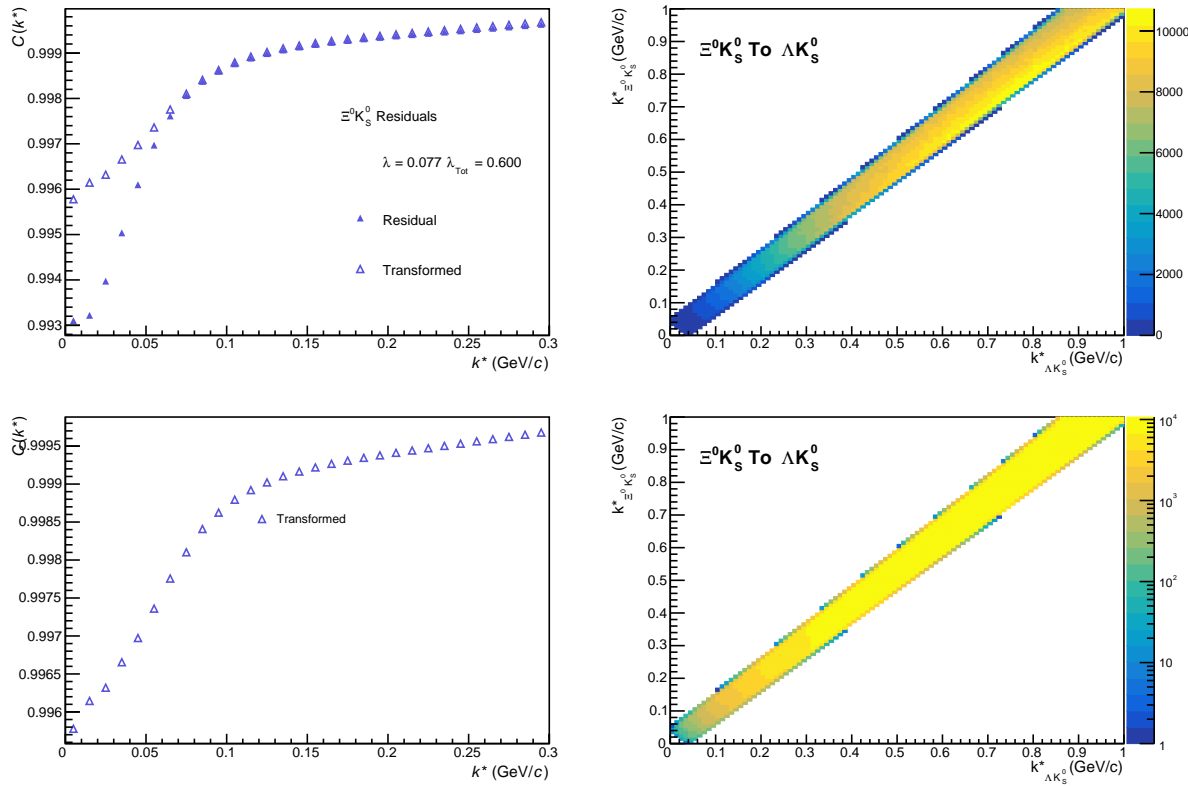
**Fig. 77:** Residuals:  $\Lambda \bar{K}^0$  to  $\Lambda \text{K}^-$  (0-10% Centrality)


**Fig. 78:** Residuals:  $\Sigma^0 \bar{K}^{*0}$  to  $\Lambda K^-$  (0-10% Centrality)

**Fig. 79:** Residuals:  $\Xi^0 \bar{K}^{*0}$  to  $\Lambda K^-$  (0-10% Centrality)

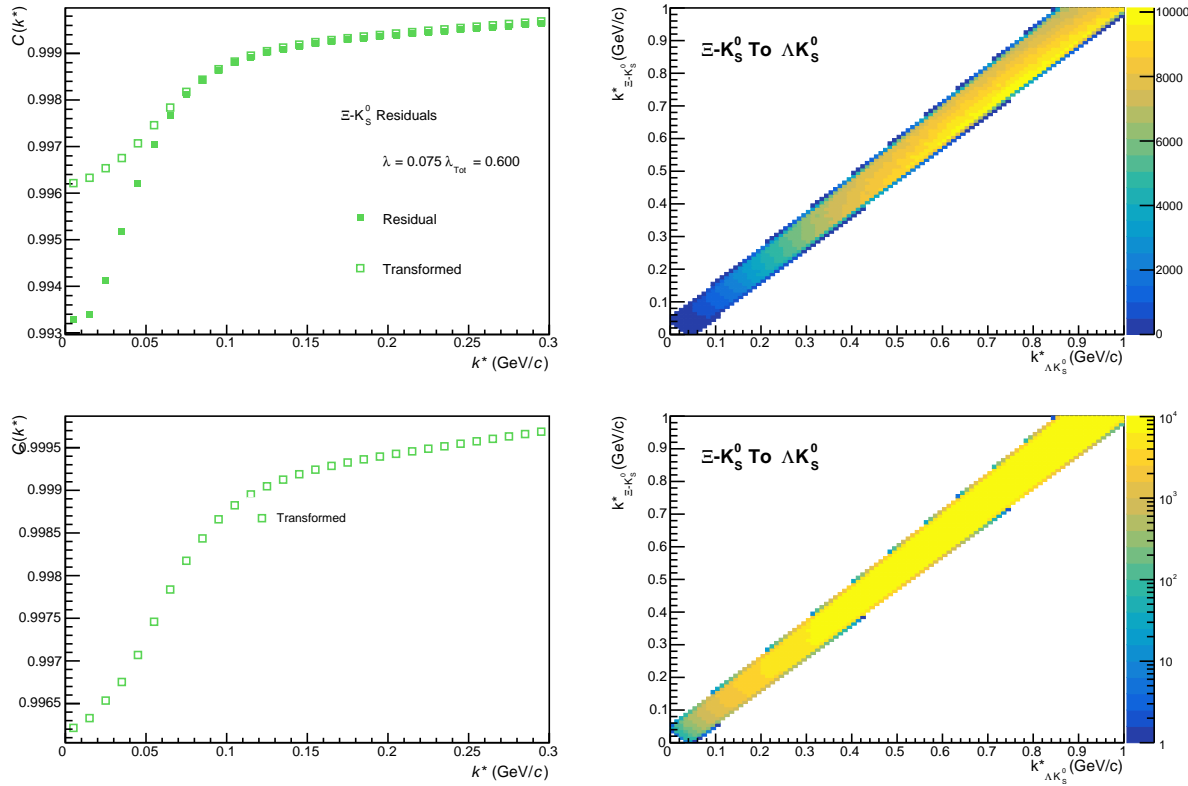


**Fig. 80:** Residuals:  $\Xi^- \bar{K}^{*0}$  to  $\Lambda K^-$  (0-10% Centrality)

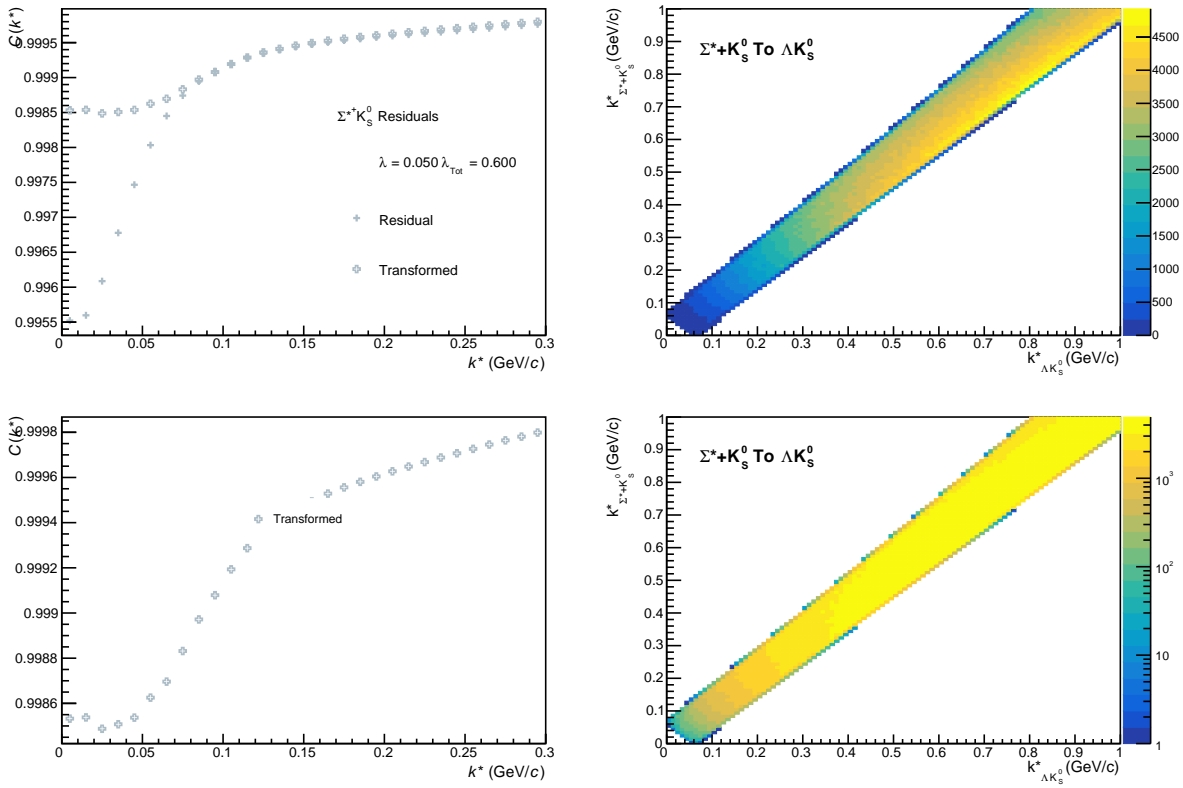
849 **9.1.3  $\Lambda K_S^0$  Residuals**

**Fig. 81:** Residuals:  $\Sigma^0 K_s^0$  to  $\Lambda K_s^0$  (0-10% Centrality)



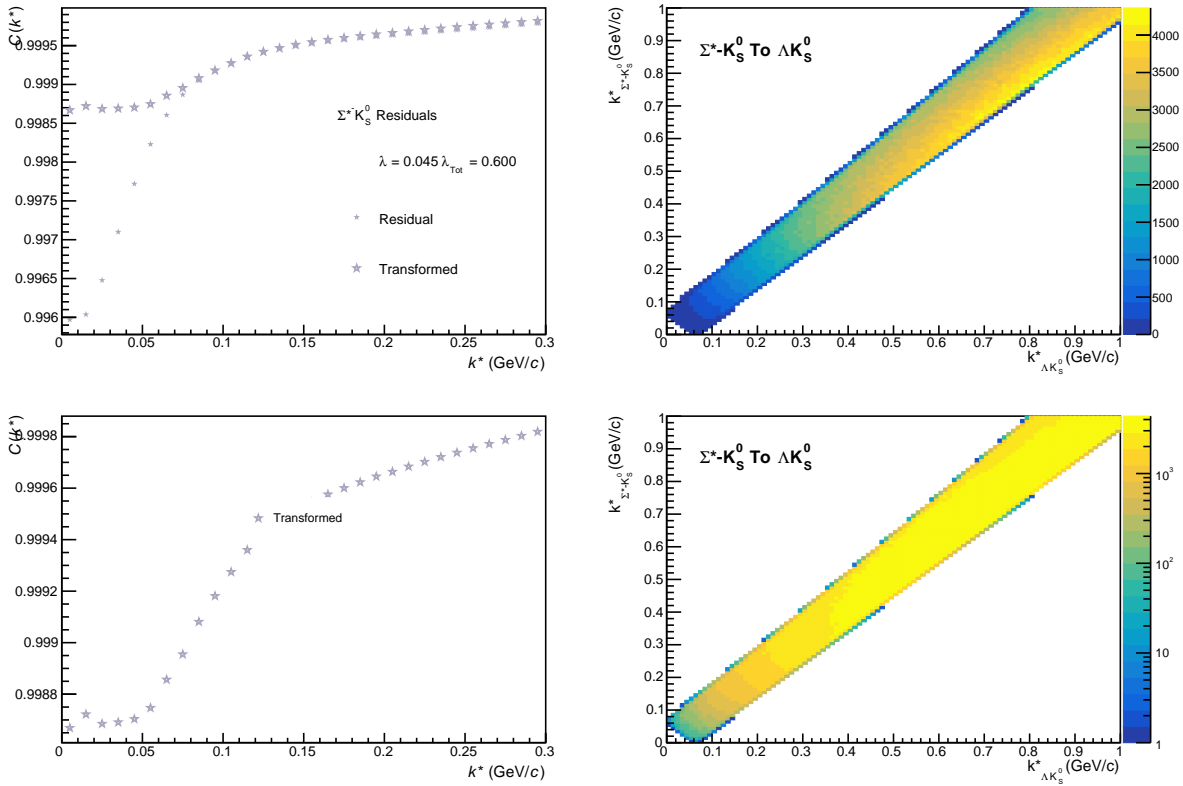
**Fig. 82:** Residuals:  $\Xi^0 K_s^0$  to  $\Lambda K_s^0$  (0-10% Centrality)



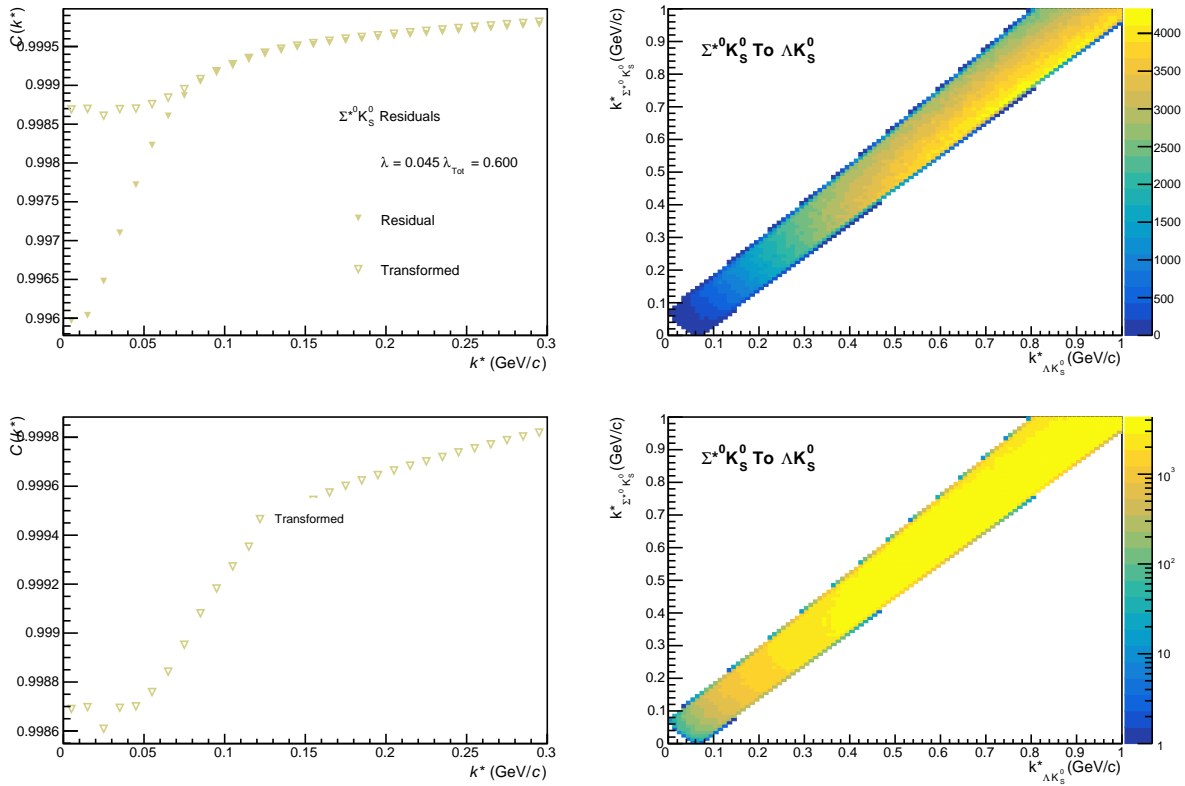
**Fig. 83:** Residuals:  $\Xi^- K_s^0$  to  $\Lambda K_s^0$  (0-10% Centrality)



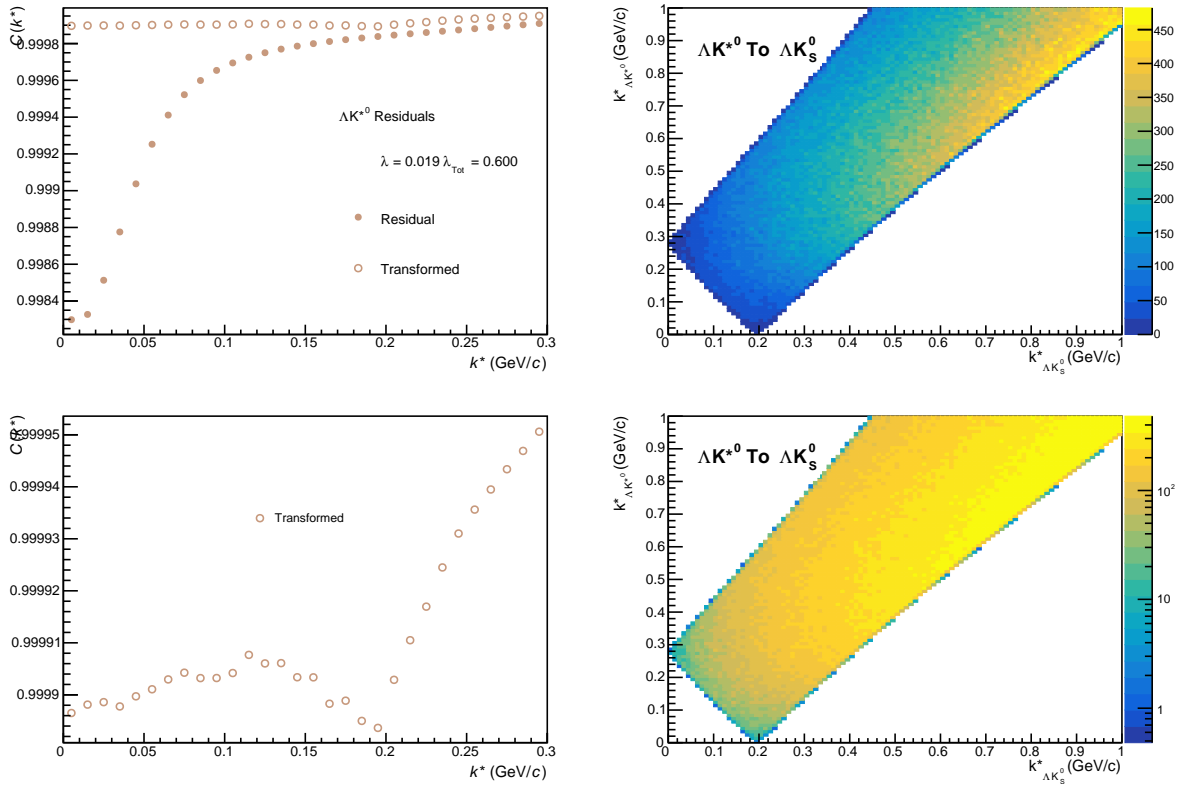
**Fig. 84:** Residuals:  $\Sigma^* + K_s^0 \rightarrow \Lambda K_s^0$  (0-10% Centrality)



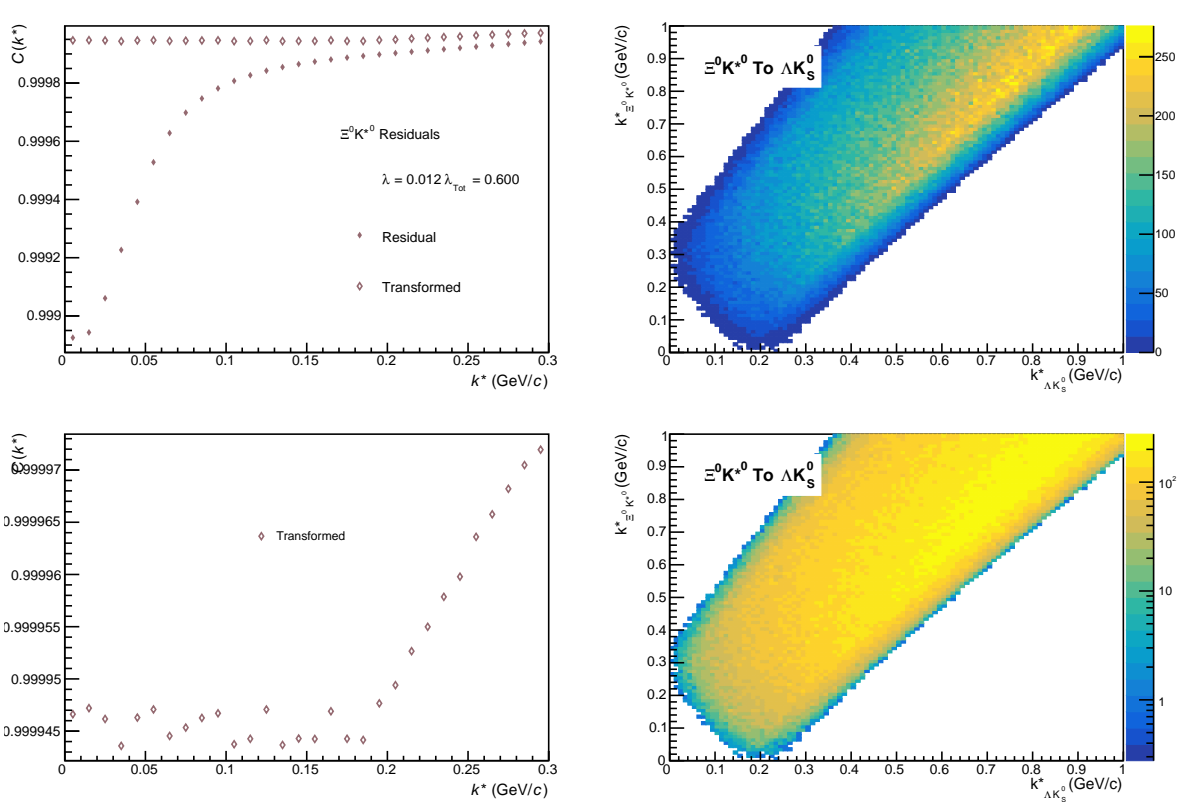
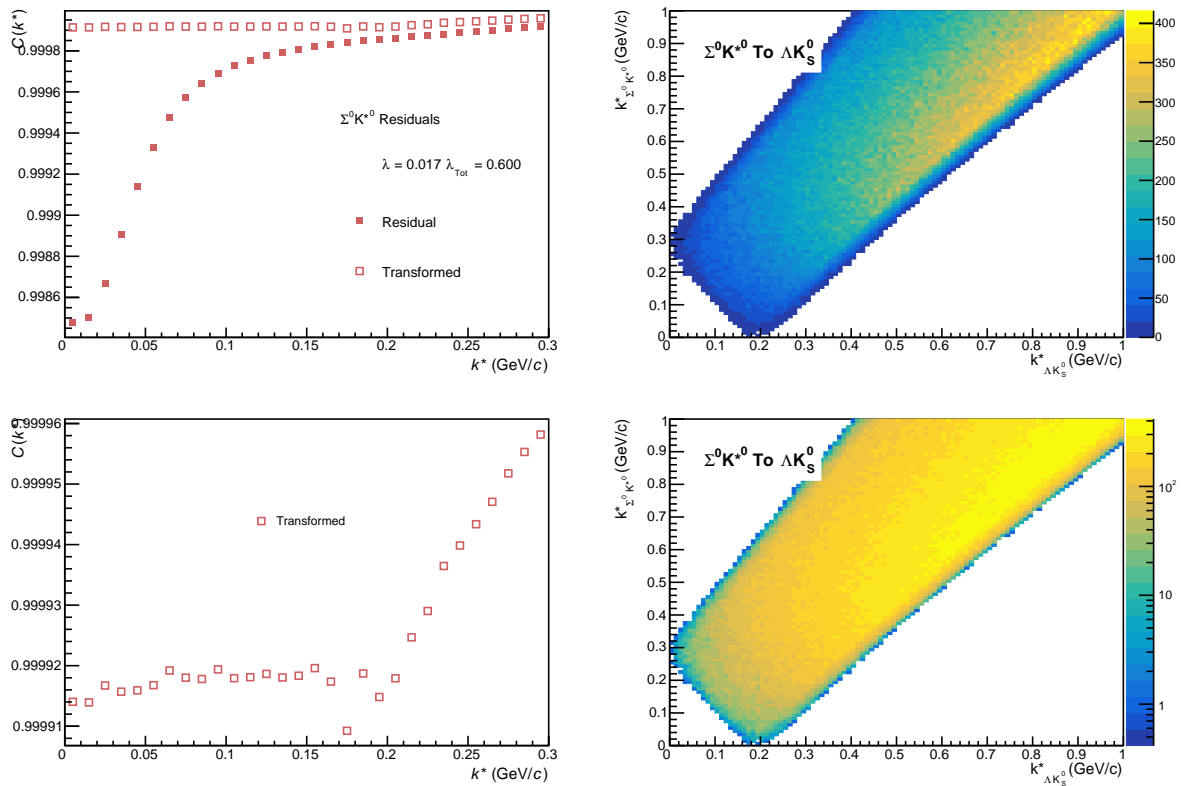
**Fig. 85:** Residuals:  $\Sigma^* - K_s^0 \rightarrow \Lambda K_s^0$  (0-10% Centrality)

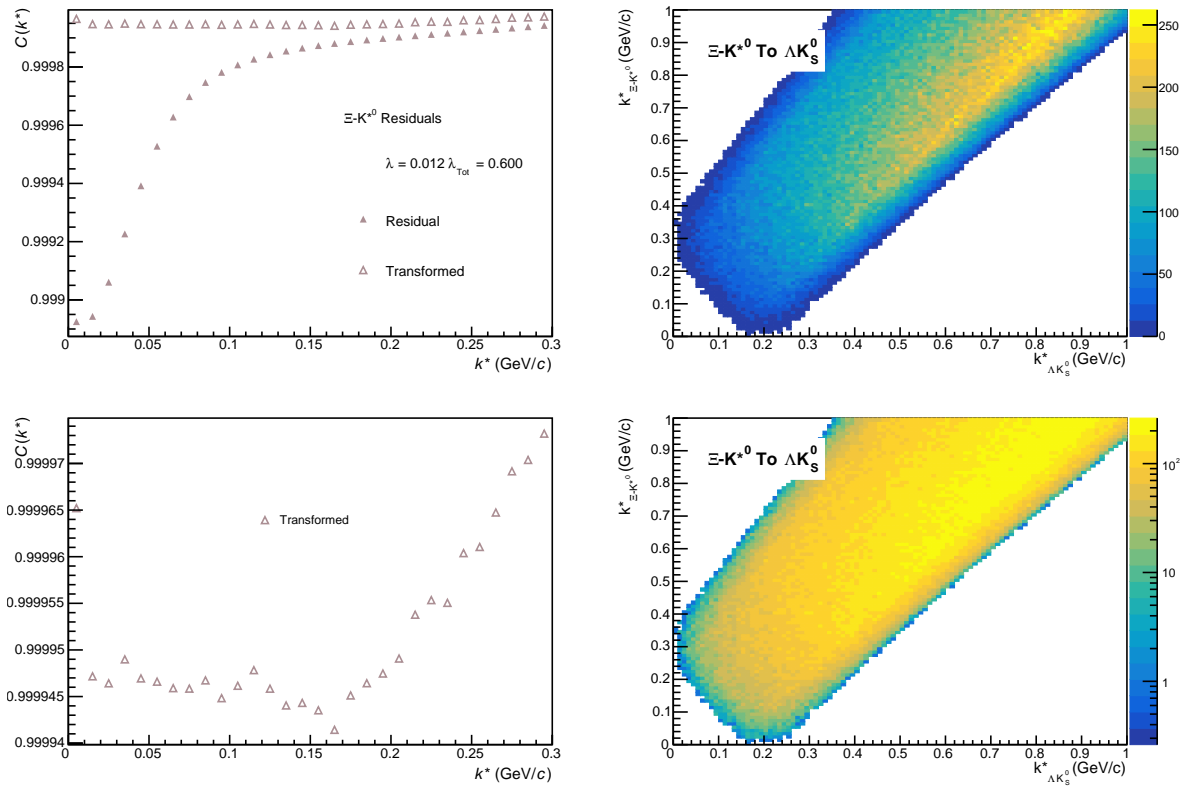


**Fig. 86:** Residuals:  $\Sigma^{*0} K_S^0$  to  $\Lambda K_S^0$  (0-10% Centrality)



**Fig. 87:** Residuals:  $\Delta K^{*0}$  to  $\Lambda K_S^0$  (0-10% Centrality)





**Fig. 90:** Residuals:  $\Xi^- K^{*0}$  to  $\Lambda K_s^0$  (0-10% Centrality)

## References

- [1] R. Lednický and V. L. Lyuboshitz. *Sov. J. Nucl. Phys.*, 35:770, 1982.
- [2] Michael Annan Lisa, Scott Pratt, Ron Soltz, and Urs Wiedemann. Femtoscopy in relativistic heavy ion collisions. *Ann. Rev. Nucl. Part. Sci.*, 55:357–402, 2005.
- [3] S. E. Koonin. Proton Pictures of High-Energy Nuclear Collisions. *Phys. Lett.*, B70:43–47, 1977.
- [4] S. Pratt, T. Csorgo, and J. Zimányi. Detailed predictions for two pion correlations in ultrarelativistic heavy ion collisions. *Phys. Rev.*, C42:2646–2652, 1990.
- [5] Richard Lednický. Finite-size effects on two-particle production in continuous and discrete spectrum. *Phys. Part. Nucl.*, 40:307–352, 2009.
- [6] Adam Kisiel, Hanna Zbroszczyk, and Maciej Szymaski. Extracting baryon-antibaryon strong interaction potentials from  $p\bar{\Lambda}$  femtoscopic correlation functions. *Phys. Rev.*, C89(5):054916, 2014.
- [7] Jai Salzwedel and Thomas Humanic. Lambda femtoscopy in  $\sqrt{s_{NN}} = 2.76$  TeV Pb-Pb collisions at ALICE, Jan 2017. Presented 15 Dec 2016.
- [8] A Kisiel. Non-identical particle correlation analysis in the presence of non-femtoscopic correlations. *Acta Physica Polonica B*, 48:717, 04 2017.
- [9] Yan-Rui Liu and Shi-Lin Zhu. Meson-baryon scattering lengths in HB chi PT. *Phys. Rev.*, D75:034003, 2007.
- [10] Maxim Mai, Peter C. Bruns, Bastian Kubis, and Ulf-G. Meißner. Aspects of meson-baryon scattering in three and two-flavor chiral perturbation theory. *Phys. Rev.*, D80:094006, 2009.
- [11] Jaroslav Adam et al. One-dimensional pion, kaon, and proton femtoscopy in Pb-Pb collisions at  $\sqrt{s_{NN}} = 2.76$  TeV. *Phys. Rev.*, C92(5):054908, 2015.